The role of chirality in synthetic microwave absorbers

Marianne Bingle

Dissertation presented for the Degree of Doctor of Philosophy in Engineering at the University of Stellenbosch

November 1998

Promoters: Prof. J.H. Cloete and Prof. D.B. Davidson

Declaration

I, the undersigned, hereby declare that the work contained in this dissertation is my own original work and that I have not previously in its entirety or in part submitted it at any university for a degree.

Signature:

Date: 10·11·1998

Opsomming

Aansprake gedurende die laat tagtigerjare dat sintetiese chirale materiale as mikrogolfabsorbeerders merkwaardige eienskappe kan besit, het wye belangstelling gewek in chirale mikrogolfabsorbeerders. Artikels het in die wetenskaplike literatuur verskyn en 'n aantal patente is uitgereik.

Bohren *et al.* het in 1992 hierdie aansprake rakende chiraliteit bevraagteken in hul artikel, *"Microwave absorbing chiral composites: is chirality essential or accidental?"* Hulle maak die opmerking dat, alhoewel 'n suspensie van metaalhelikse in 'n nie-chirale omgewing aantreklike eienskappe het vir die ontwerp van mikrogolfabsorbeerders, die chiraliteit toevallig is en nie noodsaaklik nie. 'n Eksperimentele studie deur Cloete *et al.* blyk die bevindings van Bohren *et al.* te ondersteun. Tog was daar 'n behoefte om fundamenteel die rol van chiraliteit in die interaksie tussen 'n elektromagnetiese golf en 'n absorberende medium te ondersoek, en spesifiek in die gebied waar die insluitings resonant is. Dit was die oogmerk van hierdie proefskrif.

Hierdie proefskrif behels 'n teoretiese en eksperimentele studie, by mikrogolffrekwensies, van verwante uniaksiale kristalle van geleidende draadstrukture van resonante lengte, ingelê in 'n diëlektriese materiaal. Eenheidselle van die sintetiese materiaal is ontwerp om in 'n reghoekige of vierkantige golfleier te pas sodat akkurate metings van weerkaats- en transmissiekoëffisiënte uitgevoer kan word.

Die drie-segment draadhakie, in plaas van die heliks, is as basiese element gekies vanweë die eenvoudige geometriese verband tussen die chirale enantiomere en die nie-chirale strukture. Vier uniaksiale kristalle word beskryf en geklassifiseer volgens hul puntgroep-simmetrie: 'n chirale eenheidsel; twee nie-chirale eenheidselle; en 'n raseme eenheidsel.

'n Eindige verskil tydgebied ("FDTD") rekenaarkode is ontwikkel om die chirale en nie-chirale geleidende dundraadstrukture, ingelê in 'n absorberende materiaal, te bestudeer in reghoekige golfleier. Die kode gebruik 'n subsel-dundraadformulering vir geleidende drade, en sluit die effektiewe materiaaleienskappe van die drade in.

Die rekenaarkode is getoets teen eksperimente met fisiese draadkristalle wat in S-band (2 4 GHz) reghoekige golfleier gemeet is. Die FDTD dundraadformulering vir hoogs-geleidende drade voorspel die interaksie van 'n draadkristal met 'n mikrogolf met goeie akkuraatheid ten opsigte van amplitude, fase en absorpsie.

Numeriese eksperimente is vervolgens in vierkantige golfleier uitgevoer om die kristalle te bestudeer vir hulle absorpsie eienskappe. Die volgende waarnemings is gemaak. Die insluiting van draadstrukture in 'n mikrogolfabsorbeerder kan die absorpsie van 'n elektromagnetiese golf verbeter, mits die insluitings goeie geleiers is en van resonante lengte. Dit geld vir beide chirale en nie-chirale strukture. Die eenheidsel van nie-chirale hakies is net so effektief soos die eenheidsel van chirale hakies en die raseme eenheidsel van enantiomorfe hakies in terme van verbeterde absorpsie deur die mikrogolfabsorbeerder.

Chiraliteit is 'n geometriese vereiste vir optiese aktiwiteit. Geen getuienis in hierdie eksperimente dui op chiraliteit as 'n geometriese vereiste vir absorpsie in sintetiese mikrogolfabsorbeerders nie.

Summary

Claims were made during the late 1980's that synthetic chiral materials can yield microwave absorbers with significantly improved electromagnetic and physical properties. Papers appeared in scientific literature and a number of patents were issued. These claims stimulated wide interest in microwave chiral absorbers.

In 1992 Bohren *et al.* challenged the claims about chirality by asking the question, *"Microwave absorbing chiral composites: is chirality essential or accidental?"* They concluded that "although helices have some excellent properties in the design of composite absorbing materials, the resulting chirality is accidental and not essential."

An experimental study by Cloete *et al.* seems to support the findings of Bohren *et al.* However, we are also of the opinion that fundamentally the role of chirality in the interaction between an electromagnetic wave and an absorbing medium is not yet fully understood, especially in the regime where the chiral inclusions are resonant. Hence this theoretical and experimental study of closely related uniaxial crystals of conducting wire structures of resonant length in the microwave regime, embedded in a dielectric host. Unit cells of synthetic material are designed to fit into a rectangular or square waveguide to allow accurate measurements of reflection and transmission coefficients.

The three segment wire hook was chosen as basic element, instead of the helix, for the simple geometrical relation between the chiral enantiomorphs and the non-chiral structures. Four uniaxial crystals are described, and classified according to their point group symmetry: a chiral unit cell, consisting of four hooks of the same handedness; a non-chiral unit cell of four staples; a non-chiral unit cell of four cranks; and a racemic unit cell of enantiomorphous chiral hooks, two of each handedness.

A finite difference time domain code was developed for the full-wave numerical analysis in a rectangular waveguide of the conducting thin wire structures, embedded in an absorbing host. The code uses a subcell thin wire formulation for conducting wires, including the effective material properties of the wires.

In order to validate the FDTD code, wire crystals were manufactured and measured in S-band (2 4 GHz) rectangular waveguide. The FDTD subcell thin wire formulation for highly conducting wires was found to predict the scattering with respect to magnitude, phase and absorption, with good accuracy.

Numerical experiments were performed in a square waveguide on the wire crystals to study their absorption properties. The following observations were made. The inclusion of wire structures in a microwave absorber can improve the absorption interaction of an electromagnetic wave with the host, provided that the inclusions are good conductors and of resonant length. This is observed whether the inclusions are chiral, or non-chiral. The unit cell of non-chiral cranks couples the incident field to the loss mechanisms of the host as effectively as the unit cell of chiral hooks and the racemic unit cell of enantiomorphous hooks.

Chirality is a geometrical requirement for optical activity. However, no evidence in these experiments suggests that chirality is a geometrical requirement for absorption by synthetic microwave materials.

Keywords chiral, chirality, FDTD, finite difference time domain, microwave absorber, point group, racemic, subcell thin wire formulation, rectangular waveguide, wire.

To Johannes Hendrik Cloete
for the farthest mountains are the bluest

Acknowledgement

I regard with gratitude and appreciation the persons who were involved in this work. It was an experience, rich and rewarding, to work under the guidance of Professor John Cloete and Professor David Davidson. The study was proposed by Professor John Cloete, and he suggested the three segment chiral hook and the non-chiral staple and crank. Professor Roger Raab carefully read the paragraphs on symmetry and the classification of the crystals.

This research was funded by the South African Foundation for Research Development (FRD) and industrially by the company AMS Polymers. In particular I mention Mr. Keith Dowson of AMS Polymers. The numerical experiments were performed at the University of Stellenbosch on a Silicon Graphics Origin 200 machine, funded by the FRD.

Jan Greyling and Wessel Croukamp from SED manufactured the samples, and chose guitar steel string for the first samples. Dr. Scott Kuehl manufactured the microwave absorber. Dr. Gronum Smith at EMSS kindly placed their S-band measurement system and network analyser at our disposal, and assisted with the first measurements. David Pansegrouw performed most of the measurements at the University of Stellenbosch, and bolted and unbolted many nuts. Jac Wilsenach sent me a postcard of Rodin's marble hands, *Le Secret*.

Without these hands and heads this work would have proceeded differently, or might not have been.

Contents

List of Tables

Glossary

chiral not superposable on its mirror image, i.e. possessing a definite handedness. [Gk. *kheir* hand]

circular birefringence difference between the refractive indices for left and right circularly polarized electromagnetic waves.

circular dichroism differential absorption of right and left circularly polarized light.

crystal solid enclosed by symmetrically arranged plane faces; solid with regular repetition of a unit cell.

enantiomorph mirror image, form related to another as an object is to its image in a mirror. [Gk. *enantios* opposite + *morphē* form]

FDTD finite difference time domain.

improper rotation *combined* operation of a rotation through $2\pi/n$ degrees followed by an inversion through the centre of the coordinate system.

non-magnetic crystal time-symmetric, i.e. invariant under time-inversion.

optic axis propagation axis for which no linear birefringence occurs.

PML perfectly matched layer, numerical boundary condition in the FDTD formulation.

point group 32 crystallographic point groups or crystal classes; crystals classified according to their rotational symmetry about axes through a point.

racemic composed of equal numbers of dextrorotatory and levorotatory molecules of a compound.

rotatory dispersion dependence on the wavelength of the angle of rotation of the plane of polarization.

symmetry element representation of a symmetry operation; the geometric entity with respect to which the symmetry operation is performed.

symmetry operation the act that carries a crystal into coincidence with itself.

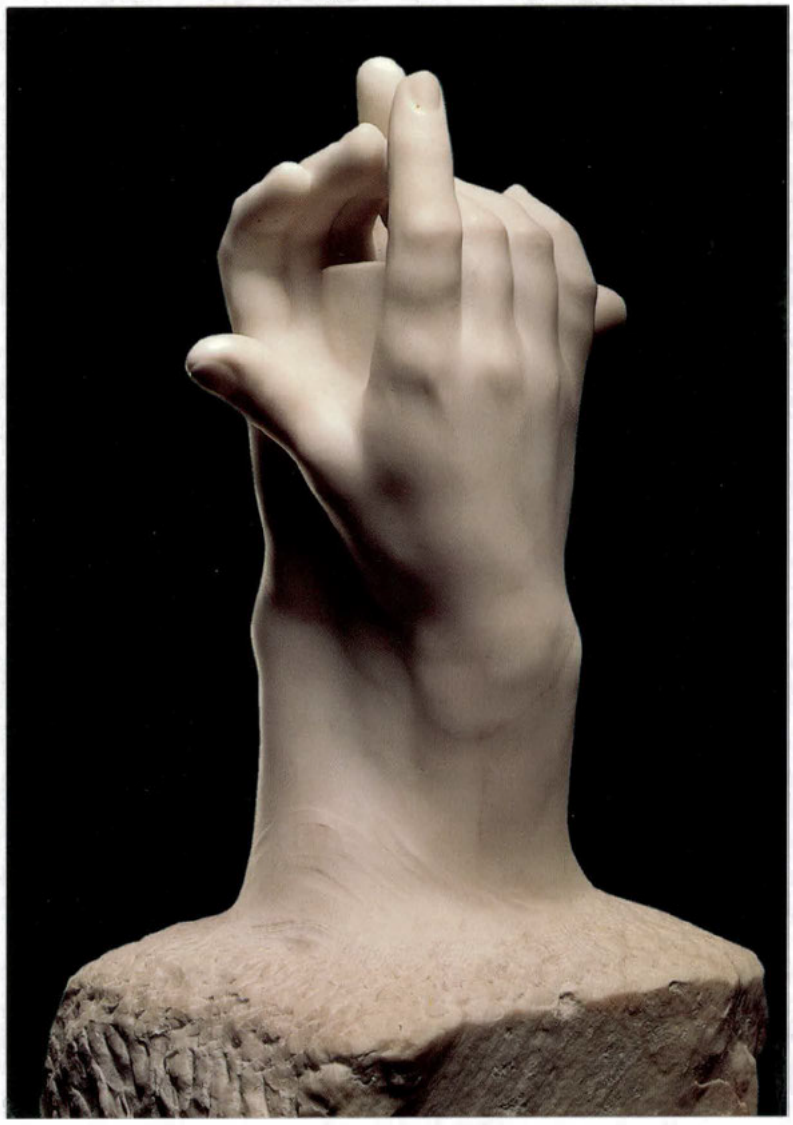

Le Secret [1]

[1] **Auguste Rodin** (1840 1917)
Musée Rodin. Paris. Photograph by E. et P. Hesmerg.

Chapter 1

Introduction

The experiments of Karl Lindman (1920) [1] and Ignacio Tinoco and Mark Freeman (1957) [2] demonstrated optical activity at microwave frequencies. Their experiments with conducting helices have placed chiral phenomena in the spectrum where electromagnetic waves cannot be perceived by the human eye, but the geometrical requirement of chirality is clearly visible. Based on current knowledge, it seems that "optical" activity at radio and microwave frequencies is (still) confined to synthetic materials which contain suitable macroscopic chiral objects [3, 4].

Optical activity (so termed for its discovery in the optical spectrum), includes circular birefringence (the difference between the refractive indices for left and right circularly polarized electromagnetic waves), circular dichroism (the differential absorption of right and left circularly polarized light), and rotatory dispersion (the dependence on the wavelength of the angle of rotation of the plane of polarization) [3, 5]. The most familiar of the chiral phenomena is the rotation of the plane of linearly polarized light by a chiral medium, a manifestation of circular birefringence.

Claims were made during the late 1980's that synthetic chiral materials can yield microwave absorbers with significantly improved electromagnetic and physical properties, e.g. "... the possibility of designing anti-reflection coatings using chiral composites" [6]; "... a novel material which reduces target RCS, through electromagnetic chirality, and makes it invisible to radar" [7]; "By incorporating electromagnetic chirality these screens offer unique advantages, such as increased absorption in thin layers for a relatively wide range of frequencies, over conventional designs" [8]; and a number of patents were issued [9]. These claims stimulated wide interest in microwave chiral absorbers.

In 1992 Bohren *et al.* [10] challenged the claims about chirality by asking the question, *"Microwave absorbing chiral composites: is chirality essential or accidental?"* They remark that no convincing physical arguments have been made as to why "chiral inclusions in a non-chiral matrix should yield a composite markedly more absorbing than a similar medium in which the inclusions are non-chiral." They conclude from a theoretical and experimental study that "while chiral inclusions may be advantageous, any absorber performance that can be obtained from a chiral composite may be obtained from its non-chiral counterpart."

An experimental study of the role of chirality in synthetic microwave absorbers by Cloete *et al.* [11] seems to support the findings of Bohren *et al.* However, we are also of the opinion that fundamentally the role of chirality in the interaction between an electromagnetic wave and an absorbing medium is not yet fully understood, especially in the regime where the chiral inclusions are resonant. Hence this theoretical and experimental study of closely related uniaxial crystals of conducting wire structures of resonant length in the microwave regime, embedded in a dielectric host. Unit cells of synthetic material are designed to fit into a rectangular or square waveguide to allow accurate measurements of reflection and transmission coefficients.

The three segment wire hook was chosen as the basic element, instead of the helix, for the simple geometrical relation between the chiral enantiomorphs[1] and the non-chiral structures.

The chiral hook is transformed into its enantiomorph by bending one of the end segments through 180°; two non-chiral geometries are possible by bending one of the end segments through ±90° (one forms an object which looks like a staple, the other looks like a crank).

The crystals are classified in the nomenclature of classical crystallography, according to their point group symmetry, in Chapter 2. Four uniaxial crystals are described: a chiral unit cell, consisting of four hooks of the same handedness; a non-chiral unit cell of four staples; a non-chiral unit cell of four cranks; and a racemic unit cell of enantiomorphous chiral hooks, two of each handedness. The chiral system is similar to that studied by Theron and Cloete [12, 13] in the study of the circular birefringence of artificial chiral crystals at microwave frequencies, but while they worked in the long wavelength regime, this study is conducted in the resonant regime.

Raab and Cloete [5] have shown that a multipole description to the order of the electric quadrupole and magnetic dipole provides a fundamental and origin independent description for the constitutive parameters of non-magnetic chiral media, in the long wavelength regime, and they stipulate the working criteria for the application of the theory to synthetic chiral crystals. Theron and Cloete [12, 13] have applied their [5] theory to study a uniaxial chiral system of hooks at microwave frequencies, where the hooks are small compared to wavelength.

The approach in this study is entirely different. The hooks are studied around resonance, and because they are electrically large a constitutive parameter description of the crystals is not possible [5]. The approach here is to accurately calculate the scattering coefficients for unit cells of the synthetic material in a rectangular or square waveguide, and from energy balance to determine the absorption by the synthetic material.

A finite difference time domain (FDTD) code was developed for the full-wave numerical analysis in a rectangular waveguide of the chiral and non-chiral conducting thin wire structures, possibly embedded in an absorbing dielectric host. The detail of the formulation is discussed in Chapter 3. Of particular interest is the inclusion of a subcell thin wire formulation to model wires with finite conductivity, for the finite conductivity of practical conductors contributes significantly to the dissipation of an electromagnetic wave in an otherwise lossless environment, especially when the wire is of resonant length.

In order to validate the FDTD code, wire crystals were manufactured and measured in S-band (2 4 GHz) rectangular waveguide. The experiments are discussed in detail in Chapter 4. The experiments were performed for hooks of copper wire and of steel wire, and for unit cells in a host of essentially transparent polystyrene foam and in a microwave absorber.

With the FDTD code well substantiated, a reliable tool is at our disposal for closely studying the behaviour of resonant wire inclusions in a host. The numerical experiments, performed in a square waveguide on the chiral, non-chiral, and racemic crystals, are discussed in Chapter 5, and interpreted within the context of the waveguide environment, and in an attempt to answer Bohren *et al.'s* question,

"Microwave absorbing chiral composites: is chirality essential or accidental?"

[1] mirror images; see Glossary, p. iv.

The following original contributions were made in search of the role of chirality in synthetic microwave absorbers.

The approach towards addressing the claims about chirality in microwave absorbers and towards finding an answer to Bohren's question is original in various aspects: in the choice of the three segment hook as the chiral element, as in the work of Theron and Cloete [12], for the closely related geometry of the enantiomorph and the non-chiral hooks; in the study of a unit cell of resonant (in the microwave regime) chiral and non-chiral hooks; in the full-wave numerical analysis of the resonant wire hooks, embedded in a host, instead of an effective medium constitutive parameter description.

The 422 chiral unit cell of four chiral hooks was studied by Theron and Cloete in the long wavelength regime. The arrangement of the non-chiral staples and cranks, and the enantiomorphous hooks to form uniaxial crystals, all with 4-fold symmetry, is original.

Specific contributions to the FDTD formulation concern the implementation of the three dimensional auxiliary source grid to naturally resolve the dispersive relation between the incident electric and magnetic field for wide band analysis, and the improved subcell formulation for thin wires to account for the finite conductivity of practical wires.

The extensive experimental validation of the FDTD code is valuable. The experiments with copper and steel hooks of resonant length, in a lossless host and in a practical dielectric absorber, are important for the physical validation of the FDTD method and directly lead to the improved formulation for wires with significant resistivity.

The numerical experiments with the wire crystals in square waveguide are original, and their outcome significant in the context of the claims which were made in scientific literature about synthetic chiral absorbers.

Chapter 2

Symmetry

"C'est la dissymétrie, qui crée le phénomène." - Pierre Curie (1908).

2.1 A sense of symmetry

Kheir is the Greek word for *hand* and *chiral* is said of an object not superposable on its mirror image, i.e. possessing a definite handedness. The definition of chirality is a geometrical requirement of handed, or screw-like, symmetry. And this "handed symmetry," or *dissymmetry*, as Louis Pasteur (1848) first described it, gives rise to optical activity. The source of natural optical activity is a *chiral* molecular or crystal structure [3].

The "handed symmetry" is not only a description of the distinctive geometrical feature of the chiral object, but it is also the symmetry of optical activity, for the plane of polarization is rotated, as though following a screw, as a linearly polarized electromagnetic wave passes through the chiral medium. This is a beautiful illustration of how the symmetry of the molecular or crystal structure of the medium is reflected in its macroscopic physical properties.

Although "optical" activity at microwave frequencies has only been observed in *synthetic* materials which contain suitable macroscopic conducting chiral objects [3, 4], it is useful to describe these materials in the language of classical crystallography. For this is a language of geometrical arrangement, of symmetry and symmetry operations, and it provides a systematic, well-developed classification of crystals, and their optical properties.

In the following sections the concepts from crystallography which are required to classify the non-magnetic wire unit cells are presented. A good introduction was found in [14] and in the book *Crystals and Light* by Elizabeth Wood [15]. At a more abstract level, the books by Birss [16] and Barron [3] provided insight into the relationship between symmetry and the physical properties of materials. The explanation of Feynman [17, vol. II-30] on symmetry in crystals and their physical properties introduces the concept almost intuitively.

2.2 The crystallographic point groups

An ideal crystal is constructed by the infinite repetition of identical structural units in space. The 32 classical point group symmetries (crystal classes) constitute the most fundamental classification of *non-magnetic* crystals [16][1]; the seven crystal systems provide seven convenient coordinate systems for reference of the geometry of the crystals.

[1] Non-magnetic crystals are time-symmetric, i.e. their property tensors are invariant under time-inversion, and are either diamagnetic or paramagnetic [16, p. 44]. Magnetic crystals are crystals that exhibit ordered arrays of (spin) magnetic moments and are not time-symmetric [16, pp. vi, 73]. This work is only concerned with non magnetic crystals.

The regular repetition of the unit cell, formed by the constituent elements of the crystal, is its most distinctive feature. In order to fill space solidly, the shape of the unit cell is restricted, and this determines the seven crystal systems of classical crystallography (triclinic, monoclinic, orthorhombic, tetragonal, trigonal, hexagonal, and cubic).

The symmetry operations of a crystal carry the crystal into coincidence with itself. A point group consists of the group of symmetry operations about a point which describes the symmetry of a crystal. Only 32 unique point groups are compatible with the translational symmetry of a crystal lattice, these are the *crystallographic point groups* or crystal classes, and are classified according to their rotational symmetry about axes through a point.

The symmetry operations which leave at least one point in its original position are rotation, reflection in a mirror plane, inversion through a centre, and improper rotation, represented by their respective symmetry elements,[2] rotation axes, mirror planes, a centre of symmetry and rotatory-inversion axes. The repetitive character of crystals confines rotation about an axis to $2\pi/n$ degrees, with $n = 1, 2, 3, 4$ or 6. Inversion through a centre transforms all coordinates (x, y, z) to $(-x, -y, -z)$, and leaves the geometry the same. An improper rotation $(\bar{n})$ is the *combined* operation of a rotation through $2\pi/n$ degrees followed by an inversion through the centre of the coordinate system. These are the only symmetry operations required to form the 32 non-magnetic crystal classes.

Further subdivisions to the non-magnetic crystal classes are obtained when translational symmetry is taken into account, including the combined symmetry elements of screw axes (for rotation-translation operations) and glide planes (for reflection-translation operations). Classical crystallography is concerned particularly with the point group, for the macroscopic properties of non-magnetic crystals depend on the symmetry of their point groups and not on the spatial symmetries obtained by combining a point group symmetry with the translational symmetry of the corresponding infinite lattice [16, p. 32].

Hermann-Mauguin symbols for the 32 point groups

The 32 crystallographic point groups and seven crystal systems are tabulated in Table 2.1, together with the symmetry elements of each point group. Various notations are used to describe the point groups. The notation most commonly adopted by chemists is the Schoenflies notation. Crystallographers prefer the Hermann-Mauguin notation. The international symbols used here are based on the notation devised by Hermann and Mauguin. (Alternative symbols in the international notation are not shown. Refer to [16, pp. 36 38].) The Hermann-Mauguin symbols provide the information necessary to generate the symmetry operations of the point group. The first part of the symbol is the number that gives the order of the principal rotation axis. Following symbols denote the presence of mirror planes or subsidiary rotation axes [18, p. 66]. The Hermann-Mauguin notations for the point groups contain the following symmetry information [15, 18]:

Mirror plane m $(m \equiv \bar{2})$

Rotation axis 2, 3, 4, 6 (2-fold, 3-fold, etc.)

Inversion axis $\bar{1}, \bar{2}, \bar{3}, \bar{4}, \bar{6}$ (1-fold inversion axis $\equiv$ centre of symmetry, 2-fold inversion axis $\equiv$ mirror plane normal to the 2-fold inversion axis, 3-fold inversion axis, etc.). An inversion axis represents the *combined* symmetry operation of a rotation through $2\pi/n$ degrees, followed by an inversion through a centre.

n/m **or** $\frac{n}{m}$ ("n over m") represents an n-fold axis with a mirror plane normal to it.

[2] The symmetry element is the geometric entity with respect to which the symmetry operation is performed.

$nm-$ represents an n-fold axis containing a mirror plane.

$n2-$ represents an n-fold axis with n 2-fold axes perpendicular to it.

$\bar{4}2m$ represents a 4-fold inversion axis containing diagonal mirror planes that bisect the angles between the 2-fold axes.

Not all the symmetry elements of a point group are contained in the Hermann-Mauguin symbol for the point group, as can be seen in Table 2.1. The symbols contain the necessary symmetry elements from which the other elements of the point group can be generated.

Stereographic projection

The stereographic projection provides a visual way to discover what symmetry elements are implied when certain elements are given. The stereographic projection is the projection onto an equatorial plane of the points of intersection of the symmetry axes and the surface of a sphere. The centre of the sphere is at the intersection of the crystallographic axes of symmetry [16, p. 39]. Rotation axes are represented by solid symbols — an oval for a 2-fold axis, a triangle for a 3-fold axis, a square for a 4-fold axis, and a hexagon for a 6-fold axis. A 3-fold inversion axis is represented by a solid triangle with an open circle in the centre, a 4-fold inversion axis is represented by an open square with a solid oval inside it, and a 6-fold inversion axis is represented by an open hexagon with a solid triangle inside it. The principal axis is presented normal to the paper. The crystallographic axes are marked at the rim of the projection by short radial straight lines. Symmetry axes perpendicular to the principal axis are projected as lines through the centre of the diagram and their symmetry order denoted by the appropriate symbols at the ends of the line. Mirror planes are indicated by heavy lines; an outer circle in heavy outline corresponds to a mirror plane normal to the principal axis. Also indicated on a general form of the stereographic projection are positions of equivalent points, that is the positions which can be obtained from any one of these points by successive application of all the symmetry operations of the point group, indicated as dots and circles. Dots represent points above the plane, and circles points below the plane of the paper.

As an example, consider the $4/m$ ("4 over m") point group. In the symbol is contained a 4-fold axis with a mirror plane normal to this axis. This is shown in the left diagram below, with one general point. If the two symmetry operations are applied to this point, the equivalent points are obtained. Successive rotation through 90° generates the three other points above the plane (dots); reflection in the mirror generates the four points below the plane (circles). Inspection of this figure shows that these points are also related by a centre of symmetry, a 4-fold inversion axis, and a 2-fold axis, always inherent in a 4-fold axis.

$4/m$

Table 2.1: The 32 crystallographic point groups and the seven crystal systems.

Crystal System	Restrictions on cell axes and angles	International Point Group Symbol	How many of each kind of symmetry element?									
			m	2	3	4	6	$\bar{1}$	$\bar{2}$	$\bar{3}$	$\bar{4}$	$\bar{6}$
Triclinic	$a \neq b \neq c$	1										
	$\alpha \neq \beta \neq \gamma$	$\bar{1}$						1				
Monoclinic	$a \neq b \neq c$	2		1								
	$\alpha = \beta = 90°$	m	1						1			
	$\neq \gamma$	$2/m$	1	1				1	1			
Orthorhombic	$a \neq b \neq c$	222		3								
	$\alpha = \beta = \gamma$	$mm2$*	2	1					2			
	$= 90°$	mmm*	3	3				1	3			
Tetragonal		4		(1)		1						
(Every point	$a = b \neq c$	$\bar{4}$		(1)							1	
group has	$\alpha = \beta = \gamma$	$4/m$	1	(1)		1		1	1		1	
one	$= 90°$	422		4+(1)		1						
4 or $\bar{4}$ axis.)		$4mm$	4	(1)		1			4			
		$\bar{4}2m$	2	2+(1)					2		1	
		$4/mmm$*	5	4+(1)		1		1	5		1	
Trigonal		3			1							
(Every point	$a = b = c$	$\bar{3}$			(1)			(1)		1		
group has	$\alpha = \beta = \gamma$	32		3	1							
one	$< 120°, \neq 90°$	$3m$	3		1				3			
3-fold axis.)		$\bar{3}m$*	3	3	(1)			(1)	3	1		
Hexagonal		6		(1)	(1)		1					
(Every point	$a = b \neq c$	$\bar{6}$	1		(1)				(1)			1
group has	$\alpha = \beta = 90°$	$6/m$	1	(1)	(1)		1	1	1	1		1
one	$\gamma = 120°$	622		6+(1)	(1)		1					
6 or $\bar{6}$ axis.)		$6mm$	6	(1)	(1)		1		6			
		$\bar{6}m2$	4	3	(1)				4			1
		$6/mmm$*	7	6+(1)	(1)		1	1	7	1		1
Cubic		23		3	4							
(Every point	$a = b = c$	$m3$*	3	3	(4)			(1)	3	4		
group has	$\alpha = \beta = \gamma$	432		6+(3)	4	3						
four	$= 90°$	$\bar{4}3m$	6	(3)	4				6		3	
3-fold axes.)		$m3m$*	9	6+(3)	(4)	3		(1)	9	4	3	

NOTE 1: The abbreviated international point group symbols are shown.
*(Refer to [16] for alternative symbols.)
NOTE 2: Numbers in parentheses refer to axes inherent in other axes present.
NOTE 3: $m \equiv \bar{2}$.
NOTE 4: α = angle bc; β = angle ca; γ = angle ab;
$\neq$ should be read "is not generally equal to."

Source: Wood [15, p. 55], Birss [16, pp. 36 38] and Kittel [19].

2.3 Symmetry and electromagnetic properties

Neumann's principle states that any type of symmetry which is exhibited by the point group of the crystal is possessed by every physical property of the crystal. Expressed in terms of asymmetry rather than symmetry, no asymmetry can appear in an effect which does not already exist in the crystal, in the influence which is exerted upon it, or in the combination of both [16, pp. 45, 46]. The implication is that a physical property may have more symmetry, but not less, than the material to which it belongs.

A crystal is inherently symmetrical, and therefore it appears the same from a limited number of symmetrically equivalent directions, but the number of directions from which it appears different is unlimited. It is to be expected that the properties of crystals will in general depend on the direction in which they are measured, and are therefore anisotropic [16, p. 2].

The optical effects which can occur in transparent matter are refraction, linear birefringence (explained in the electric dipole approximation), circular birefringence (explained in the electric quadrupole-magnetic dipole approximation), and linear Lorentz and Jones birefringence (explained in the electric octopole-magnetic quadrupole approximation) [20]. The effects that may occur in a crystal for a given propagation direction are a consequence of its point group symmetry [20].

Crystals are classified as optically isotropic (corresponding with the cubic system), optically uniaxial (corresponding with the trigonal, tetragonal and hexagonal systems) and optically biaxial (corresponding with the orthorhombic, monoclinic and triclinic systems) according to the form of the electric susceptibility tensors of the crystal systems. The origin of linear birefringence in non-magnetic uniaxial and biaxial crystals can be explained in the electric dipole approximation in terms of the anisotropy of the susceptibility tensor. The optic axis is a propagation axis in the crystal for which no linear birefringence occurs. In uniaxial crystals there is one optic axis, and it coincides with the principal symmetry axis of the crystal (3-fold, 4-fold or 6-fold in the trigonal, tetragonal and hexagonal systems, respectively). The two crystallographic axes normal to this axis are symmetrically equivalent in uniaxial crystals. In biaxial crystals there are, to the order of electric dipole, only two directions for which linear birefringence does not occur. These are therefore the optic axes and the crystals are called biaxial [20].

It was noted before that optical activity (the rotation of plane polarized light through a crystal) has the symmetry of a screw. A screw lacks a centre of symmetry and has no plane of symmetry either parallel or normal to its axis. Crystals with a centre of symmetry cannot rotate the plane of polarized light, because inversion through a centre changes the handedness of an object. Optical activity can also not occur along the optic axis of a crystal with a symmetry plane parallel or normal to the optic axis. Consideration of the symmetry requirements of optical activity restricts the crystal classes in which optical activity may occur to those shown in Table 2.2.

Table 2.2: Crystal classes in which optical activity may occur.

Triclinic	Monoclinic	Orthorhombic	Tetragonal	Trigonal	Hexagonal	Cubic
1	2	$mm2^*$	4	32	6	23
	m	222	$\bar{4}^*$	3	622	432
			422			
			$\bar{4}2m^*$			

* No optical activity along the optic axis. Source: Wood [15, pp. 141 142].

2.4 Classification of the wire crystals

For the study of the role of chirality in synthetic microwave absorbers, the three segment wire hook was chosen as the basic element. The hook, instead of the helix, was chosen for the simple geometrical relation between the chiral enantiomorphs and the non-chiral structures (Figure 2.1).

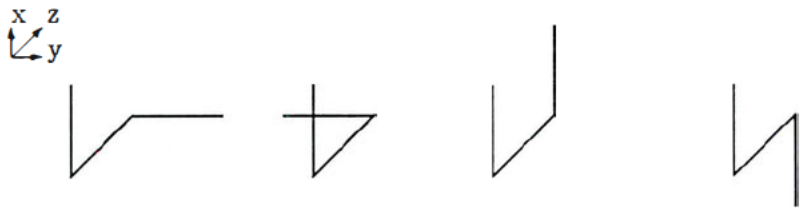

Figure 2.1: Basic wire hook structures. Two chiral hooks of opposite handedness (enantiomorphs), a non-chiral staple and a non-chiral crank.

These basic elements were combined to form uniaxial crystals of 4-fold or $\bar{4}$-fold point group symmetry in the tetragonal crystal system. A chiral unit cell of point group 422 symmetry, a non-chiral unit cell of staples of point group $4/m$ symmetry, a non-chiral unit cell of cranks of point group $\bar{4}$ symmetry and a racemic unit cell of enantiomorphous chiral hooks of point group $\bar{4}$ symmetry are classified. Each unit cell consists of four wire hooks of equal length. A uniaxial crystal in the tetragonal system has one unique 4-fold axis, and two crystallographic axes normal to this axis which are symmetrically equivalent.

Next to each unit cell is shown the stereographic projection of the symmetry elements of the point group, and of equivalent points.

Chiral unit cell of point group 422 symmetry.

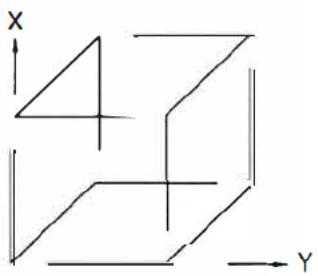

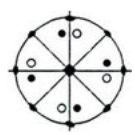

422

Point group 422 has one 4-fold axis and four 2-fold axes.
There are no mirror planes or centre of symmetry.
The unit cell consists of four chiral hooks of one handedness.
The unit cell is chiral, the mirror unit cell consists of four chiral hooks of opposite handedness.

Non-chiral unit cell of point group $4/m$ symmetry.

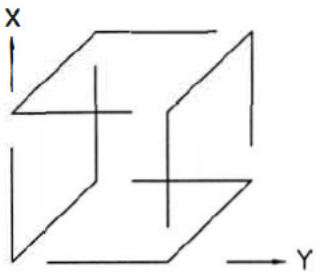

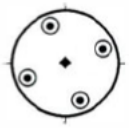

$4/m$

Point group $4/m$ has a 4-fold axis and a mirror plane normal to the 4-fold axis.
The other symmetry elements are a 4-fold inversion axis and a centre of symmetry.
The unit cell consists of four non-chiral staples.
The unit cell is non-chiral.
The symmetry of the point group excludes optical activity as a physical property.

Non-chiral unit cell of point group $\bar{4}$ symmetry.

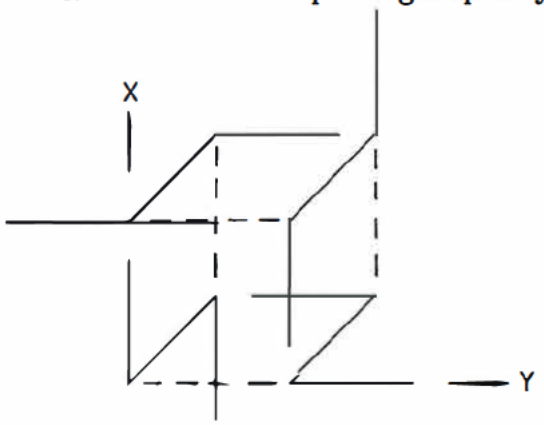

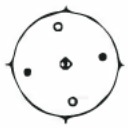

$\bar{4}$

Point group $\bar{4}$ has one 4-fold inversion axis.
There are no mirror planes or centre of symmetry.
The unit cell consists of four non-chiral cranks.
The unit cell is non-chiral.

Racemic unit cell of point group $\bar{4}$ symmetry.

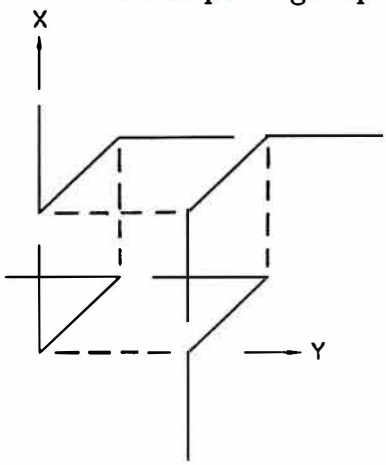

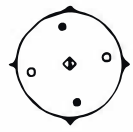

$\bar{4}$

Point group $\bar{4}$ has a 4-fold inversion axis.
There are no mirror planes or centre of symmetry.
The unit cell consists of four chiral hooks, two of each enantiomorph.
The unit cell is non-chiral, although the individual constituent elements are chiral.

Chapter 3

Finite Difference Time Domain Formulation

3.1 Introduction

A finite difference time domain (FDTD) code was developed[1] for the full-wave numerical analysis in a rectangular waveguide of the chiral and non-chiral conducting thin wire hooks embedded in an absorbing dielectric host. The hooks are studied around resonance, and because they are electrically large an effective medium constitutive parameter description of the crystals cannot be used [5]. Therefore, the approach is to perform a full-wave numerical analysis of the resonant wire hooks, embedded in an absorbing dielectric host, in a rectangular or square waveguide. It is a full three dimensional code with a subcell thin wire formulation for highly conducting wires. Other features include the wide band excitation and termination of a rectangular waveguide, propagation in an absorbing dielectric material, and placement of the chiral and non-chiral wire objects at lattice points inside the host.

In the FDTD method [21, 22] space and time is discretized and Maxwell's partial differential equations,

$$\begin{aligned} \nabla \times \mathbf{H} &= \sigma \mathbf{E} + \epsilon_0 \epsilon_r \frac{\partial \mathbf{E}}{\partial t}, \\ \nabla \times \mathbf{E} &= -\mu_0 \frac{\partial \mathbf{H}}{\partial t}, \end{aligned} \tag{3.1}$$

are approximated by central difference equations. As a result of the central differencing, the electric and magnetic field components are interleaved in space and time on staggered grids. (This motivates the use of the Yee-grid, as first proposed by Yee in 1966, and the $\frac{\Delta t}{2}$ offset in time between computing the E- and H-field components.) The spatial mesh is shown in Figure 3.1. The time evolution of the fields is computed by time-stepping through space, subject to the boundary and initial conditions, and at a time step to comply with the Courant stability criterion. A uniform spatial discretization (Δ) is used in all three dimensions.

In these equations, the medium is a hypothetical non-magnetic dielectric with a constant real relative permittivity (ϵ_r) and a constant conductivity (σ).

For the study of propagation in an absorbing dielectric host, consider a medium, linear, uniform, isotropic and non-magnetic and for which the contributions of quadrupoles and higher order multipoles are neglected [23]. Under these conditions the macroscopic Maxwell equations describe the interaction of an electromagnetic field with a dielectric material by the electric

[1] The code is written in FORTRAN 77. All the simulations were performed on a Silicon Graphics Origin 200 machine. It is a two processor R10000 machine with 320 MB RAM.

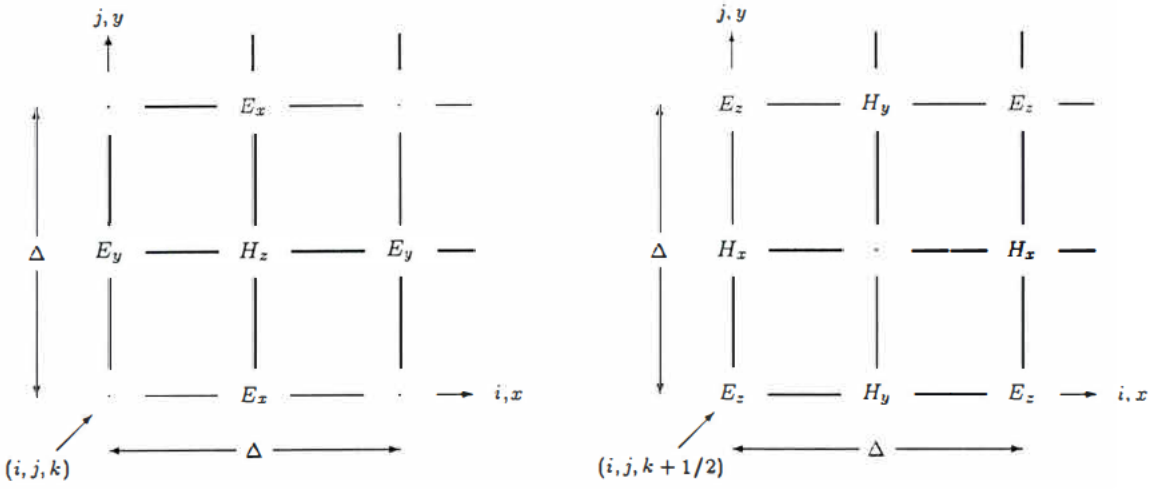

Figure 3.1: Yee-grid showing interleaved field components.

polarization. The permittivity of a material is in general a complex function of frequency and describes the dispersion and absorption characteristics of the material. Different types of polarization occur in dielectric materials according to the molecular composition of the material, and the classical models for the permittivity are based on the polarization mechanisms [24, pp. 18 40]. Electronic and ionic polarization are modelled by second order Lorentz dispersion, orientation polarization is described by the Debye model, and the Drude model describes the interaction of free electrons in the material with an electromagnetic field [25, §7.5]. Physically these models are required to be causal [25, §7.10]. Various techniques are used in the finite difference time domain method to analyse dispersive materials, based on the models for the polarization mechanisms, e.g. [21, 22, 26].

Far below the resonant frequency characterising a polarization mechanism, the contribution of the polarization mechanism to the permittivity of the material is essentially a real constant. In Equation (3.1) the assumption is that the permittivity can be represented by a real constant in the frequency range of interest, and that ohmic loss accounts for absorption in the material. The characterization of a physical microwave absorber is discussed further in Section 3.4.

3.2 Detail of the formulation

The numerical experiment consists of a rectangular waveguide with excellent conductor waveguide walls (i.e. $E_{\tan} = 0$ is enforced numerically).[2] The waveguide is terminated at both ends in an absorbing boundary condition. The code uses the total field-scattered field formulation described in [22, pp. 111 135]. A transverse plane divides the numerical space into a total field region and a scattered field region. At this plane the incident electromagnetic field of the TE_{10} mode is launched into the total field region of the waveguide (Figure 3.2). The connecting conditions between the scattered field and total field regions require knowledge of the incident E- and H-fields at this plane.

[2] In the computational literature *perfect electric conductor* (PEC) is commonly used where the condition $E_{\tan}$ 0 is applied.

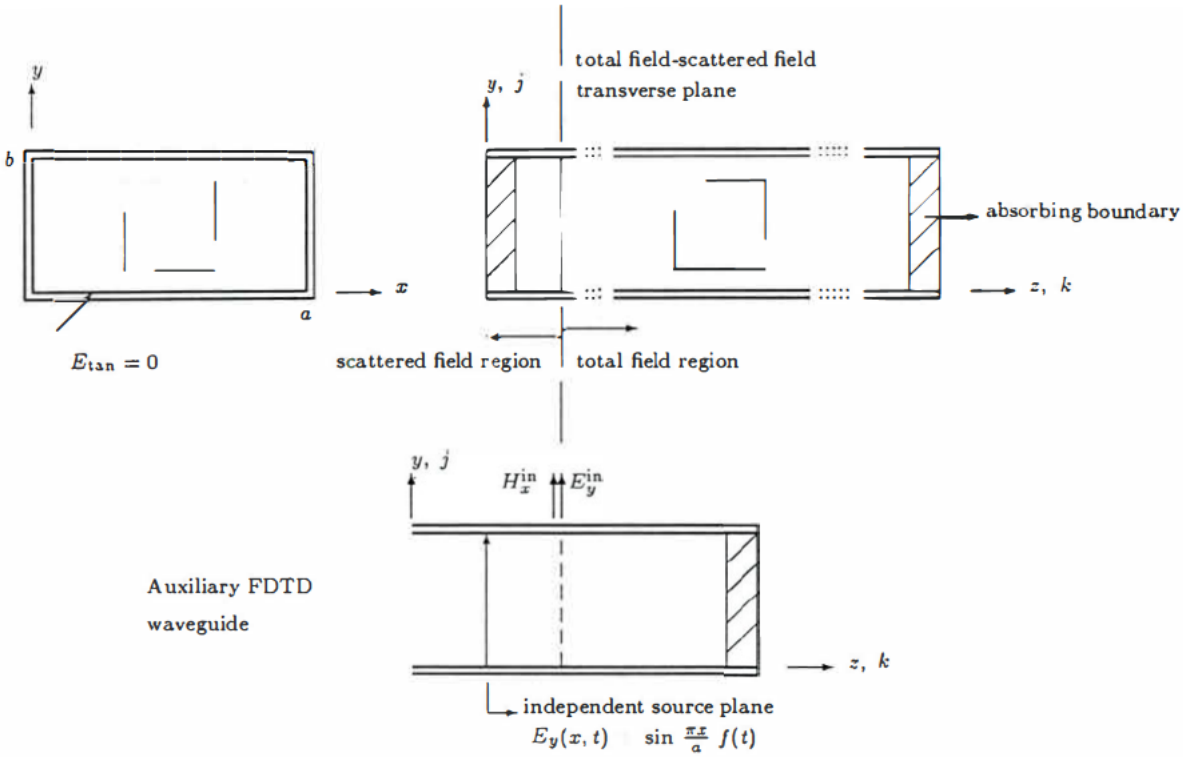

Figure 3.2: Rectangular waveguide geometry and FDTD configuration.

3.3 Rectangular waveguide

3.3.1 Excitation

Propagation in waveguide is dispersive, as expressed in the frequency domain relation between the transverse electric and magnetic field components of the TE_{10} mode,

$$\begin{aligned} E_y(x,f) &= -Z_{TE}(f)H_x(x,f) = E_0(f)\sin\frac{\pi x}{a}, \\ Z_{TE}(f) &= \frac{\eta_0}{\sqrt{1-(\frac{f_c}{f})^2}}, \end{aligned} \tag{3.2}$$

where $\eta_0 = \sqrt{\mu_0/\epsilon_0}$, a is the dimension of the waveguide in the x-direction and $f_c = \frac{c}{2a}$ is the cutoff frequency of the TE_{10} mode in a rectangular waveguide. The group velocity measured along the waveguide is

$$v_g = c\sqrt{1-\left(\frac{f_c}{f}\right)^2}, \tag{3.3}$$

where c is the velocity of light in vacuum [27, pp. 423-428]. For a waveguide filled with air, $\epsilon_r \approx 1.00059$ at standard atmospheric pressure and temperature [28, p. 221],[3] and the properties of vacuum are realistic.

Both the E- and H-field components of the incident electromagnetic field are required (in time) across the total field-scattered field transverse plane. In the time domain the electric and

[3]Standard atmospheric pressure and temperature are 1.01×10^5 Pa and 0° C.

magnetic fields in the waveguide are related by convolution, and in the FDTD discretization scheme the E- and H-field components are offset in time and space. Instead of determining the one from the other through convolution, the incident E- and H-fields are computed in an auxiliary FDTD waveguide, *in parallel with* the main code (Figure 3.2).

In the auxiliary FDTD waveguide an independent distributed source is applied at a transverse plane in the waveguide by specifying the tangential E-field components (independently) at this plane [22, §6.4].[4] For the TE_{10} mode, $E_y(x,t) = \sin \frac{\pi x}{a} f(t)$ at this plane. This launches a numerical electromagnetic wave which propagates in the auxiliary waveguide, in both directions. The auxiliary grid has the actual waveguide cross-section dimensions and is terminated in a perfectly matched layer absorbing boundary. In the auxiliary grid the FDTD boundary value problem naturally resolves the dispersive relationship between the electric and magnetic field due to the waveguide dispersion, and with the required time and spatial offset in the FDTD discretization. The calculated E- and H-field components at a transverse plane in the auxiliary grid are read at each time step into the main code as the incident field required at the total field-scattered field plane (Figure 3.2).

The approach described in [22] for the calculation of the incident field to implement the connecting condition at the total field-scattered field boundary is based on a table look-up procedure. A one dimensional auxiliary source grid generates a look-up table with the space-time variation in unbounded space of the incident fields. From the look-up table data, and with the appropriate delay distance, the incident fields at all grid positions on the total field-scattered field boundary are determined through linear interpolation [22, pp. 121 135]. Due to the dispersive nature of the waveguide, a three dimensional auxiliary grid is required here to determine the space-time variation of the incident fields over a bandwidth of frequencies. The incident E- and H- field components are updated and read at each time step into the main code. A look-up table is not used. (For monochromatic excitation, of course, the incident electric and magnetic fields are related by a constant factor, and convolution in the time domain is not required. The code was not used to run monochromatic problems, since the interest was to study behaviour in a broader frequency band.)

At the independent source transverse plane the tangential E-field components are independently specified (and not updated with the FDTD equations), regardless of any other fields propagating in the FDTD solution space. Any reflections from the absorbing boundary terminating the waveguide will be retroreflected from the independent source. It is therefore important that the absorbing boundary condition should provide very good absorption to suppress unphysical reflections from the independent source in the grid. Note that the independent source divides the auxiliary grid into two independent regions. The fields in either region cannot propagate past the source plane.

The time dependence of the excitation is a modulated, windowed, sinusoidal carrier-function,

$$f(t) = \begin{cases} \left(1 - \left(\frac{t-t_0}{q}\right)^2\right)^4 \sin 2\pi f_0(t-t_0), & \text{if } |(t-t_0)/q| < 1, \\ 0, & \text{otherwise,} \end{cases}$$

with a selected bandwidth around the carrier frequency f_0, above the cutoff frequency in the waveguide. The spectrum of $f(t)$ is determined with the discrete Fourier transform.

3.3.2 Absorbing boundary condition

Propagation in waveguide can both be multimodal and dispersive, and the absorbing boundary condition (ABC) used to terminate the waveguide must be able to absorb energy having widely

[4] Taflove uses the term *hard source* [22, p. 109].

varying transverse distributions and group velocities [22, p. 195]. Berenger's perfectly matched layer (PML) [29, 30] has been reported as a robust dispersive ABC for propagating electromagnetic fields in FDTD simulation of waveguide systems [22]. The PML has been implemented to terminate the waveguide in the z-directions of both the FDTD grid and the auxiliary source grid.

3.3.3 Calibration of the FDTD waveguide experiment

FDTD simulations in a rectangular waveguide were run to determine the quality of the excitation and the absorbing boundary condition. For this purpose the waveguide end-termination of the auxiliary FDTD grid was selected far away (1.8 m) from the independent source plane to prevent possible reflections from the termination from entering the FDTD grid. A waveguide of dimensions, 78 mm $\times$ 42 mm was considered. A spatial discretization of $\Delta = 3$ mm was chosen and a time step $\Delta t = 5.78$ ps to comply with the Courant stability criterion for the FDTD time-stepping. The frequency spectrum of the excitation is shown in Figure 3.4. (The parameters for the modulated, windowed, sinusoidal function are $f_0 = 2.8$ GHz; $q = 1.44$ ns; $t_0 = q = 1.44$ ns.)

The field is sampled at the centre of a transverse plane of the waveguide at the absorbing boundary. The experiment was performed with a PML and a second order Mur boundary condition. The absorbing boundaries at both ends of the waveguide were 63 mm from the total field-scattered field plane. The fields were calculated for 1040 time steps. The reflection coefficient from the termination is determined by dividing the spectrum of the reflected electric field by the spectrum of the incident electric field. The incident field at the sampling point is determined from an FDTD run for a long (1.8 m) empty waveguide structure. The reflected field at the boundary is determined by subtracting the incident field from the total field. The time domain data is transformed with the discrete Fourier transform to the frequency domain. The normalised group velocity is determined by dividing the spectrum of the magnetic field at the boundary, multiplied by η_0, by the spectrum of the electric field at the boundary.

In Figure 3.3 the reflection coefficient for the PML ABC is compared to the second order Mur boundary condition. The performance of the PML is better than -60 dB between the first and second cutoff frequencies of the rectangular waveguide. In Figure 3.4 the computed normalised group velocity is compared to the analytical expression. The error introduced by reflections from the second order Mur boundary is evident while the small reflections from the PML do not influence the computation of the propagating fields notably.

The PML boundary condition is sufficient for termination of both the FDTD grid and the auxiliary source grid. The performance of the PML greatly enhances the sensitivity of the code to determine low level scattering from objects inside the waveguide. With no scattering objects in the auxiliary source grid, it can be terminated a few cells from the independent source plane. This greatly reduces the memory requirements introduced by the auxiliary FDTD waveguide grid.

3.4 Characterization of a microwave absorber

Microwave absorbers frequently measured at the University of Stellenbosch consist of graphite coated spherical balls of polystyrene foam. These can be characterised as non-magnetic, with a relative permittivity (in general dispersive and complex) and a conductivity (constant up to infrared frequencies). The material parameters can be determined from the measured scattering parameters either through a direct inversion technique [31, 32] or a model-based parameter estimation technique [33, 34].

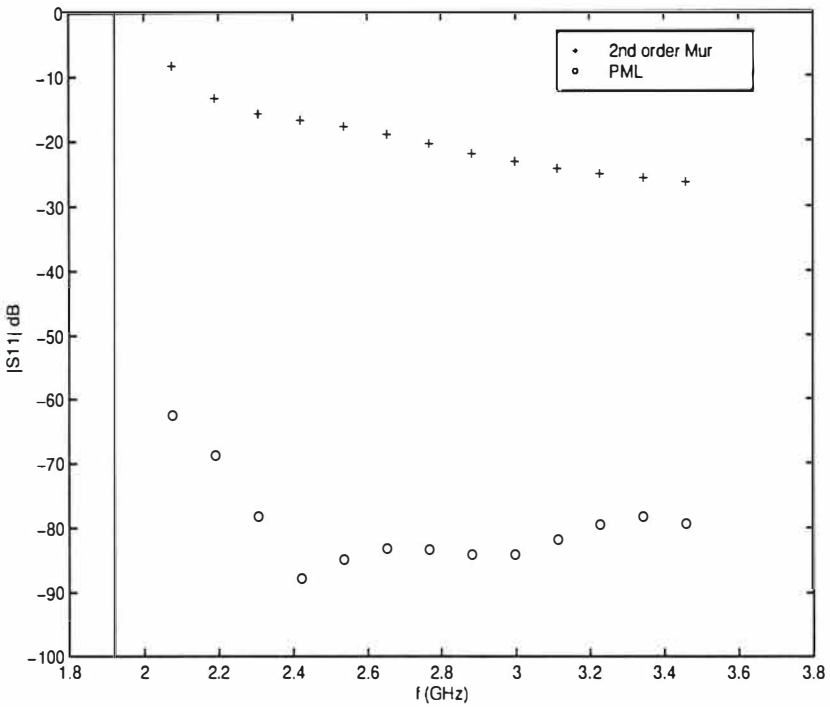

Figure 3.3: Reflection coefficients for a second order Mur and a PML boundary in a rectangular waveguide. (8 cell PML with quadratic loss profile and R(0)=10 ^{7}.)

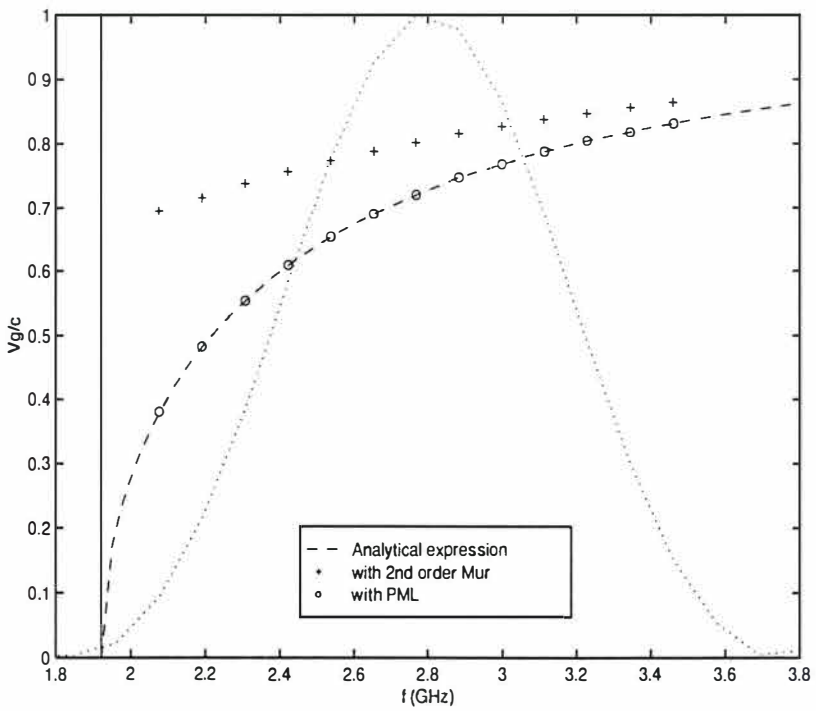

Figure 3.4: Normalised group velocity in a rectangular waveguide, determined from the calculated FDTD electric and magnetic fields at the absorbing boundary. The spectrum of the incident field is also shown. The waveguide dimensions are 78 mm × 42 mm, with $f_{c(\mathrm{TE}_{10})}$=1.9 GHz and discretization Δ = 3 mm.

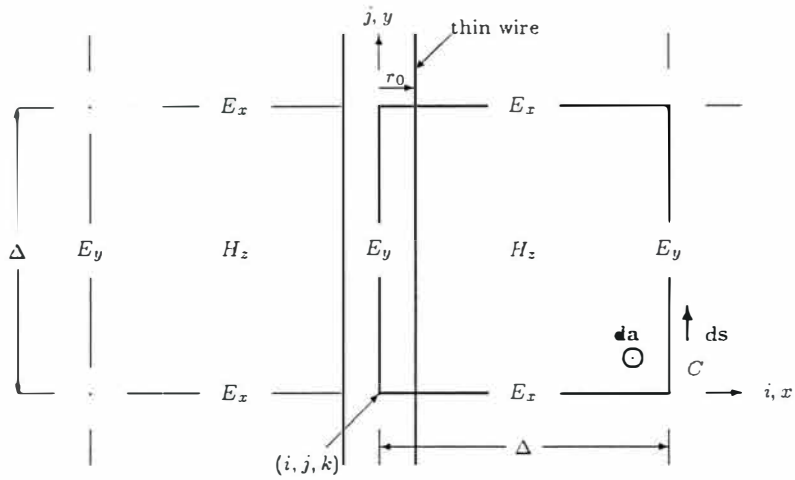

Figure 3.5: Contour and surface of integration for discretization of Faraday's contour integral in a cell containing a thin wire.

The direct inversion technique is accurate except for weakly absorbing samples at frequencies where the sample thickness is multiples of half a wavelength. The direct inversion technique does not distinguish between dielectric loss (bound charges) and ohmic loss (free electrons or ions) in the material. It determines a complex number for the permittivity at each frequency of measurement, and the loss due to the conductivity of the material is included in Im (ϵ_r).

In the model-based parameter estimation technique a frequency dependent model for the permittivity, with constant coefficients, is chosen based on a microscopic theory of matter which is consistent with linearity and causality constraints [25, 35]. For a material with conductivity, a term is added to Im (ϵ_r) to account for ohmic losses in the material $(\epsilon_r^* = \epsilon_r(\omega) - j\frac{\sigma}{\omega\epsilon_0})$.[5] The constitutive parameters are obtained by estimating the constant coefficients in the model. The corresponding scattering parameters are fitted to the measured scattering parameters by minimizing the sum of the squares of the differences between the predicted and measured scattering parameters [34].

It was found, by comparing the material parameters determined from the measured scattering parameters with the two different techniques, that the microwave absorber of graphite coated spherical balls of polystyrene foam can be characterised by a constant real permittivity and a constant conductivity across S-band.

The FDTD equations, derived from Equation (3.1), therefore are sufficient to describe propagation through an absorbing dielectric host of this kind. Comparison of the calculated S-parameters to the analytic solution for a slab of thickness d indicated that the absorber length in the FDTD experiment appears $2 \times \frac{\Delta}{2}$ longer than the thickness specified in cells. This is not strange in the staggered scheme of the FDTD discretization. For FDTD experiments in an absorbing host, the absorber thickness is therefore specified Δ shorter than the physical length.

3.5 Subcell thin wire formulation

A subcell thin wire formulation is used to incorporate wires of thinner than FDTD grid size

[5] Note that the frequency dependent model for $\epsilon_r(\omega)$ must be consistent with causality constraints. A time convention $e^{j\omega t}$ is assumed.

dimensions (e.g. in [21, §10.3] and [22, §10.5]). For this, Faraday's contour integral,

$$\oint_C \mathbf{E} \cdot \mathrm{d}\mathbf{s} = -\frac{\mathrm{d}}{\mathrm{d}t} \iint_S \mu_0 \mathbf{H} \cdot \mathrm{d}\mathbf{a}, \tag{3.4}$$

is discretized in the cells containing a thin wire.[6] The contour and surface of integration are shown in Figure 3.5.

The contour integration of the electric field along the cell sides is performed analytically to update the circumferential magnetic field through the cell surface. In performing this integral, the radial electric field and the circumferential magnetic field components are assumed to have a $1/r$ field dependency. For an excellent conductor, the tangential electric field component in the wire is assumed to be zero (e.g. Taflove [22, p. 288]). For the actual wires with significant resistivity considered in this work, $E_{\tan} \neq 0$ in the wire and needs to be determined.

The update equations for a thin wire bend of 90 degrees are derived with the same field assumptions [37].

3.5.1 The radial field dependency

The $1/r$ approximation for the radial electric field and the circumferential magnetic field components is a quasistatic approximation for the *scattered* radial electric field of an infinitely long line charge and the *scattered* circumferential magnetic field of an infinitely long line current.

The FDTD formulation described here updates total fields. According to [22] it can be assumed that the $1/r$ dependency of the scattered field dominates the incident field and therefore can be applied to the total fields [22, p. 290].

The $1/r$ field dependency is applied to all cells containing a thin wire, regardless of the cell's relative position along the length of the wire. The effect of this for wires of finite length (especially for wires of the order of a wavelength or half a wavelength) might be significant, since for a wire of resonant length, charge will concentrate at the endpoints of the wire. The formulation is evaluated for resonant wire structures, both in a lossless host, and in a dielectric absorber, against experiments in rectangular waveguide.

3.5.2 The finite conductivity of the wire

The finite conductivity of practical conductors contributes significantly in the interaction of an electromagnetic wave with a wire, especially when the wire is of resonant length. Therefore the subcell thin wire formulation was refined to model wires with finite conductivity, i.e. where $E_{\tan} \neq 0$ in the wire.

A frequency domain approximation relates the tangential electric field at the wire surface to the total current in the wire (of radius r_0) through an internal impedance,

$$E_{\tan}(r_0, \omega) = Z_i(r_0, \omega) I(\omega). \tag{3.5}$$

The high frequency approximation for the internal impedance of a round conductor [27, p. 184] is

$$(Z_i)_{\mathrm{hf}} \approx \frac{1}{2\pi r_0} \sqrt{\frac{j\omega\mu_0}{\sigma}}, \tag{3.6}$$

assuming the metal is non-magnetic at microwave frequencies, and the conductivity of the wire (σ) is frequency independent. Except for a multiplicative constant, this expression is identical to the expression for the surface impedance of a good conductor infinite half space which is used

[6] A different approach has recently been described in [36].

by Beggs *et al.* [38] as a surface impedance boundary condition. The approach to update the tangential electric field in the wire is essentially the same as described in [38], with the main difference that for the thin wire formulation the current and the time derivative of the current are required in the wire. For the sake of the subtle differences, the approach is outlined here.

A few remarks on the notation in this work are appropriate. The electromagnetic fields are interchangeably expressed in the time domain, the frequency domain and the s-domain. The same symbol is used in the different domains — the domain is indicated by the parameter, t or ω or s. $E_y(t)$ is a real function in the time domain while $E_y(\omega)$ and $E_y(s)$ are complex functions in the frequency and s-domains respectively. This also applies to the current in the wire. The spatial coordinates are omitted.

The internal impedance of Equation (3.6) is proportional to the square root of the frequency, and also related to the permeability (here assuming μ_0) and conductivity of the wire. By mathematically manipulating Equations (3.5) and (3.6) and through analytic continuation ($j\omega \rightarrow s$),

$$E_{\tan}(r_0, s) = Z_i'(r_0, s) s I(s), \tag{3.7}$$

$$Z_i'(r_0, s) = \frac{1}{2\pi r_0}\sqrt{\frac{\mu_0}{\sigma}}\frac{1}{\sqrt{s}}. \tag{3.8}$$

$Z_i'(r_0, s)$ is defined in order to facilitate the transformation to the time domain. Using the Laplace transform pair $\mathcal{L}^{-1}\left(\frac{1}{\sqrt{s}}\right) = \frac{1}{\sqrt{\pi t}}$ $(t > 0)$ [39, p. 299], the inverse Laplace transform of Equation (3.7) relates the tangential electric field at the wire surface in the time domain by convolution to the time derivative of the current in the wire,

$$E_{\tan}(r_0, t) = z_i'(r_0, t) * \frac{\partial I}{\partial t}, \tag{3.9}$$

$$z_i'(r_0, t) = \frac{1}{2\pi r_0}\sqrt{\frac{\mu_0}{\pi\sigma}}\frac{1}{\sqrt{t}}, \quad t > 0. \tag{3.10}$$

The convolution of Equation (3.9) is defined by the convolution integral,

$$E_{\tan}(r_0, t) \quad \frac{1}{2\pi r_0}\sqrt{\frac{\mu_0}{\pi\sigma}}\int_0^t \frac{1}{\sqrt{t-\tau}}\frac{\partial I(\tau)}{\partial \tau}\partial\tau. \tag{3.11}$$

The convolution integral is discretized in time ($t = n\Delta t$) by writing it as the sum of integrals over time intervals of Δt. The time derivative of the current is written as a backward difference equation. The update equation for the tangential electric field component in the wire is then a convolution sum, requiring knowledge of all previous current values,

$$E_{\tan}^n(r_0) = \frac{1}{2\pi r_0}\sqrt{\frac{\mu_0}{\pi\sigma\Delta t}}\sum_{m=0}^{n-1} Z_0(n-m-1)(I^{m+\frac{1}{2}} - I^{m-\frac{1}{2}}), \tag{3.12}$$

$$Z_0(m) \equiv \int_m^{m+1}\frac{\mathrm{d}\alpha}{\sqrt{\alpha}} = 2(\sqrt{m+1} - \sqrt{m}). \tag{3.13}$$

$Z_0(m)$ is the discrete impulse response [38], obtained with the assumption that the fields are piecewise constant in time. By expanding $Z_0(m)$ in an exponential series,

$$Z_0(m) \approx \sum_{p=1}^{N} a_p e^{\alpha_p m} \tag{3.14}$$

the convolution sum can be performed recursively. The coefficients for a ten term exponential series adequately approximating the function $Z_0(m)$, determined with Prony's method, are tabulated in [21, p. 174].

The update equation for the tangential electric field becomes,

$$E^n_{\tan}(r_0) = \frac{1}{2\pi r_0}\sqrt{\frac{\mu_0}{\pi\sigma\Delta t}}\sum_{p=1}^{10}\Psi^n_p, \tag{3.15}$$

$$\Psi^n_p = a_p\sum_{m=0}^{n-1} e^{(n-m-1)\alpha_p}(I^{m+\frac{1}{2}} - I^{m-\frac{1}{2}}) \tag{3.16}$$

$$= e^{\alpha_p}\Psi^{n-1}_p + a_p(I^{n-\frac{1}{2}} - I^{n-\frac{3}{2}}), \tag{3.17}$$

$$\Psi^1_p = 0. \tag{3.18}$$

Ψ^n_p is determined recursively from the current in the wire at the two previous time steps. The current is determined from the discretized Ampère's contour integral of the circumferential H-field, neglecting the displacement current in the immediate neighbourhood of the wire (i.e. within half a cell). For clarity, the spatial indexing is omitted in the above development. A spatial point (i, j, k) is associated with every $E^n_{\tan}$ and in the Yee-grid it is assumed that $E^n_{\tan}(r_0)$ can be replaced by $E^n_{\tan}(i, j, k)$ in the centre of the wire. The current $I^{n+\frac{1}{2}}(i, j, k)$ is in the same direction as the tangential electric field, and both are parallel to the wire axis.

3.5.3 Memory requirements

The memory requirements can roughly be estimated for an FDTD waveguide problem of $NX \times NY \times NZ$ spatial cells, including a subcell thin wire formulation. The memory in bytes is roughly (for single precision),

$$4 \times (NX \times NY \times NZ) \times [\text{ID} + \text{E} + \text{H} + \underbrace{\text{IDWire} + \text{HW} + \text{EW} + \text{IW} + N * \text{WConv}}_{\text{thin wire formulation}}].$$

NX, NY and NZ (number of cells in x-, y- and z-directions); ID (identifier for each cell for the material specification); IDWire (identifier for each cell for a thin wire); E (three electric field components in each cell); H (three magnetic field components in each cell); HW (three additional magnetic field components in each cell, required by the thin wire formulation); EW (three additional electric field components in each cell, required by the thin wire formulation); IW (three current components in each cell, required by the thin wire formulation); WConv (three recursive convolution components in each cell, required by the thin wire formulation); $N = 10$ (ten term exponential series approximation of the discrete impulse response of the wire). EW, IW and $N \times$WConv are required by the improved subcell thin wire formulation for wires of finite conductivity.

$$\text{Memory (in bytes)} \approx 4 \times (NX \times NY \times NZ) \times [1 + 3 + 3 + \underbrace{1 + 3 + 3 + 3 + 30}_{\text{thin wire formulation}}].$$

From this estimation the additional memory requirement of the subcell thin wire formulation is evident. Here the code allows for thin wire structures in each cell of the waveguide problem. The memory requirements can be largely reduced by restricting the cells in which thin wires may be present (say to a length of NZW cells, which will reduce the memory requirements of the thin wire formulation by a factor NZW/NZ). It will also reduce the run time. This was not implemented in the code for the simulations presented in this work. The numbers quoted later for the FDTD code run times and memory usage are therefore not particularly efficient.

3.5.4 Validation of the subcell thin wire formulation

The extensive experimental validation of the FDTD code is presented in Chapter 4. In order to determine the ability of the FDTD code to accurately model resonant wire hook structures in a rectangular waveguide, possibly embedded in a dielectric absorber, the code was tested against measurements in a rectangular waveguide. The experiments with steel hooks of resonant length in a lossless host directly lead to the improved formulation for thin wires to account for the resistivity of practical wires.

During the various stages of the code development, simple experiments were performed to check for obvious errors in the implementation of the subcell thin wire formulation. For example, the thin wire formulation was first implemented for excellent conductors ($E_{\tan} = 0$) and checked for consistency in the calculations for the three different wire orientations and for the 12 possible rectangular bend orientations, in unbounded space. Qualitatively, the FDTD predictions were also compared to a moment method analysis (NEC4) for the current induced on a wire in unbounded space when illuminated with a plane wave. In the rectangular waveguide the subcell thin wire formulation for an excellent conductor was compared to the solution by a variational method [40, pp. 257 263] for a single string (solid inductive post) spanned across the waveguide. These experiments and results are not discussed since the validation presented in Chapter 4 is considered to demonstrate sufficiently and thoroughly the ability of the FDTD code to perform accurate numerical experiments of resonant wire hook structures in a rectangular waveguide, possibly embedded in a dielectric absorber.

Chapter 4

Validation of the code

4.1 Introduction

In order to validate the FDTD code for the numerical analysis of subcell conducting thin wire structures of resonant length, potentially embedded in an absorbing dielectric host, wire crystals were manufactured and measured in S-band rectangular waveguide. The experiments were performed for hooks of copper wire and of steel wire, and for unit cells in a host of polystyrene foam and in a microwave absorber.

4.2 S-band waveguide measurement configuration

Measurements were performed with the HP8510C vector network analyser measurement system [41]. The measurement system consists of a synthesized sweeper, an S-parameter test set, and the microwave receiver and network analyzer.[1] The system can be used to make S-parameter measurements over the frequency range of 45 MHz to 20 GHz. The S-parameter test set uses two directional couplers to separate the RF signal provided by the source into an incident signal, sent to the device under test, and a reference signal against which the reflected and transmitted signals are compared. It also routes the transmitted and reflected signals to the receiver.

A schematic diagram of the S-band waveguide measurement set-up is shown in Figure 4.1. The experimental set-up consists of two S-band rectangular waveguide directional couplers,[2] and a waveguide sample holder (of length, 19.75 mm). The sample holder is positioned between the two waveguide directional couplers. Two waveguide loads[3] terminate the two unused ports of the directional couplers. The waveguide is fed through a waveguide-to-coaxial adapter[4] at the direct port of the one directional coupler. On the transmit side, the coupler is terminated in a waveguide load at the direct port, and the transmitted signal is measured at the 10 dB directional port. (Note that the HP8541B S-parameter test set has internal directional couplers. The S-band directional coupler on the left in Figure 4.1 is simply used as a waveguide section. The S-band directional coupler on the right is used in a set-up to obtain an improved load for the S_{11} measurement.)

An S_{11} one port calibration is performed with three calibration standards: a waveguide load, a short (aluminium plate) and a 52 mm offset short. For the transmission measurement a through calibration is performed, with the sample holder in position. Calibration is with

[1] HP8341B synthesized sweeper, 10 MHz – 20 GHz; HP8541B S-parameter test set, 45 MHz – 20 GHz; HP8530A microwave receiver.

[2] Flann microwave instruments directional coupler; type 10132 10; directivity 40 dB; coupling value 10 dB.

[3] Maury microwave model S301A WR284 fixed waveguide termination with flange; VSWR (maximum) 1.025.

[4] Maury right angle launch adapter, model S213D2 WR284; VSWR (maximum) 1.25.

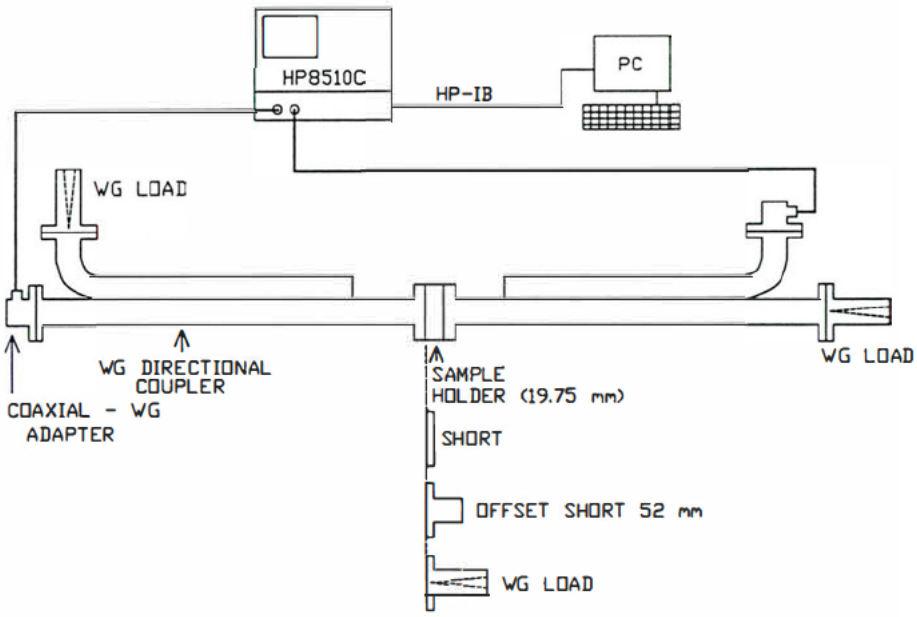

Figure 4.1: Schematic diagram of the S-band waveguide measurement set-up.

respect to the front of the sample holder. The calibration kit and error correction procedure for the S-band waveguide experimental system were adapted by Dr. Gronum Smith at the University of Stellenbosch from the 11 17 GHz quasi-Gaussian beam free space measurement system [31]. The calibration standards are at least as good or better than the standards used with the free space measurement system, and the measurement uncertainty guaranteed by Hewlett-Packard for the HP8510C vector network analyser measurement system is smaller at S-band frequencies than between 11 and 17 GHz. The measurement uncertainty for the free space measurement system are an amplitude uncertainty of approximately 0.1 dB and a phase uncertainty of approximately 4° for both the reflection coefficient and the transmission coefficient [31, p. 85], and are conservative estimates for the S-band waveguide measurement set-up.

The measurements were performed on the measurement system at the University of Stellenbosch. Measurements were also performed on a duplicate measurement system at the company, EMSS in Stellenbosch. Measurements were repeated with different calibrations and on different samples of the same geometry.

The internal dimensions of S-band waveguide are 2.84" × 1.34" (≈ 72.0 mm × 34.0 mm), with the recommended frequency range for the TE_{10} mode, 2.6 3.95 GHz.

4.3 FDTD waveguide configuration

For the numerical experiments, the frequency spectrum of the incident field was between 2.3 and 3.6 GHz, therefore only the TE_{10} mode can propagate. (The parameters for the modulated, windowed, sinusoidal function are $f_0 = 3.0$ GHz; $q = 1.67$ ns; $t_0 = q$.)

The reflected and transmitted electric fields were sampled at the centre of a transverse plane of the waveguide at a distance of about 200 mm from the front and back of the unit cell. The next higher order mode is the TE_{20} mode. It is evanescent in this frequency spectrum, and at the sampling distance is sufficiently attenuated by a factor of $e^{-\alpha_{20}z} = 0.00016$ at 3.6 GHz.

The time domain data are transformed with the discrete Fourier transform to the frequency domain. The reflection coefficient is determined by dividing the spectrum of the reflected electric

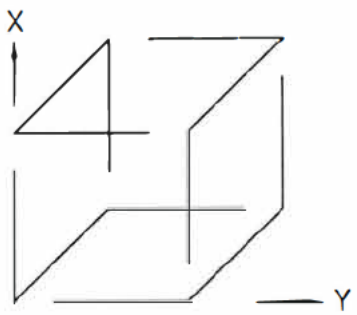

Figure 4.2: Chiral unit cell of point group 422 symmetry.

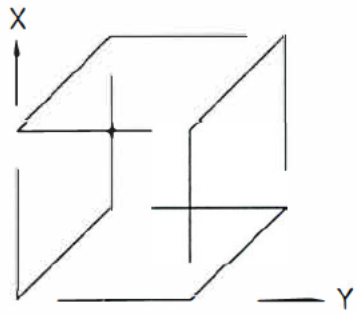

Figure 4.3: Non-chiral unit cell of point group $4/m$ symmetry.

field by the spectrum of the incident electric field,

$$S_{11} = \frac{\mathcal{F}\{E_y(i_c, j_c, k_r, t)\}}{\mathcal{F}\{E_y^{in}(i_c, j_c, k_r^{in}, t)\}}, \tag{4.1}$$

where (i_c, j_c, k_r) is the sampling point for the reflected field, and k_r^{in} refers the phase of S_{11} to the sample front. The transmission coefficient is determined by dividing the spectrum of the transmitted electric field by the spectrum of the incident electric field,

$$S_{21} = \frac{\mathcal{F}\{E_y(i_c, j_c, k_t, t)\}}{\mathcal{F}\{E_y^{in}(i_c, j_c, k_t, t)\}}, \tag{4.2}$$

where (i_c, j_c, k_t) is the sampling point for the transmitted field. The incident field is sampled at the required positions in a simulation run for an empty waveguide.

4.4 Three wire crystals

For the experimental study in a rectangular waveguide, three closely related systems of resonant wire hooks are considered. The chiral unit cell of point group 422 symmetry (Figure 4.2); the non-chiral unit cell of point group $4/m$ symmetry (Figure 4.3); and a racemic unit cell of point group 2 symmetry, consisting of four thin wire hooks of alternating handedness (Figure 4.4). The chiral and non-chiral unit cells were classified in Chapter 2, and are optically uniaxial. A resonant racemic unit cell in the tetragonal crystal system, shown in Chapter 2, does not fit into the rectangular waveguide, therefore the point group 2 unit cell was chosen for the experiments in the rectangular waveguide. The descriptive term *racemic* is used in the sense that an equal number of left and right handed hooks are present. Point group 2 falls in the monoclinic crystal system and the crystal is optically biaxial (Appendix B).

The three segments of each hook are of equal length and the total length (L) is the same for all the hooks. A single unit cell is designed to fit into S-band rectangular waveguide, with the centre legs in the direction of the waveguide axis. The unit cell is centered in the rectangular waveguide. The hooks are studied around resonance, with each hook half a wavelength long in the host material. Experiments were performed on the three anisotropic unit cells in S-band rectangular waveguide to validate the FDTD code.

The experiments were performed for hooks of copper wire and of steel wire, and for the unit cells in a host of polystyrene foam and in a microwave absorber. The steel wire is of acoustic guitar steel string. Detail of the steel, and its microwave properties are not known. A DC measurement of the conductivity of the steel string yielded $\sigma_{\text{steel}} = 4.7 \times 10^6$ S/m. Depending

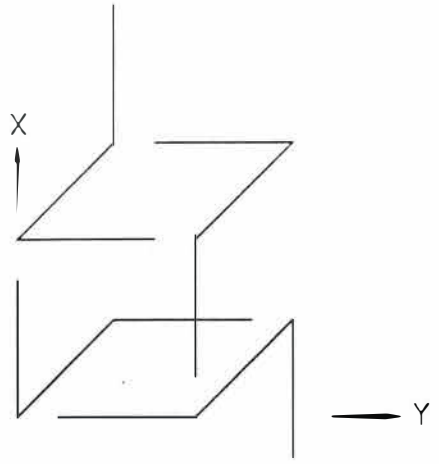

Figure 4.4: Racemic unit cell of point group 2 symmetry.

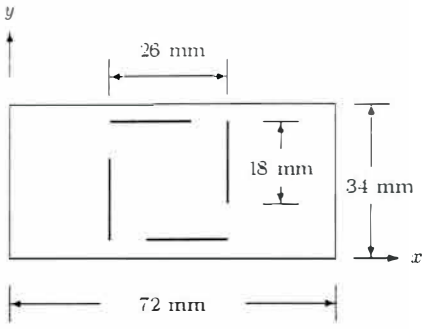

Figure 4.5: Diagram of the unit cell's position in the rectangular waveguide

on the carbon and silicon contents, referenced values for the conductivity of steel are in the range 0.1 1.0 $\times$ 10^7 S/m (e.g. [42, 28, 43]). The wire diameter is 300 μm for both the copper and the steel wires.

With the TE_{01} mode cutoff, the measured and predicted scattering parameters for the racemic unit cell are, within measurement accuracy and manufacturing tolerance, identical to that of the chiral unit cell. The results for the racemic unit cell are therefore not shown in this chapter, nor included in the detail discussion. However, the discussion and conclusions are confirmed by the additional experiments performed with the racemic unit cell. For completeness, the measured and predicted scattering parameters for the racemic unit cell are presented in Appendix B.

4.5 The wire crystals in polystyrene foam

4.5.1 Geometry

Design for a half wavelength resonance frequency of 2.8 GHz in air determines $L = 54$ mm $= 3 \times$ 18 mm. The distance between the centre legs was chosen to be 26 mm. A diagram of a unit cell in the rectangular waveguide is shown in Figure 4.5. The hooks were positioned in a polystyrene foam slab of dimensions 72 mm $\times$ 34 mm $\times$ 18 mm. The properties of the polystyrene foam were measured in S-band rectangular waveguide. The inverted medium parameters for the polystyrene foam were determined as $\epsilon_r \approx 1.02$, with $\tan\delta < 0.001$; $\mu_r = 1$. The wire of the appropriate length for each hook was threaded through the host at the required position, and then bent to form the three segment hook. The hooks were secured in position with a few stitches sewn through the host.

4.5.2 Measured effect of wire conductivity

A comparison between the measured amplitudes of the scattering parameters of the copper and steel unit cells are presented in Figure 4.6 for the chiral unit cell and in Figure 4.7 for the non-chiral cell. Two steel chiral unit cells of the same geometry were constructed differently. The one construction method was described above. In a different construction the hooks were positioned on the edges of a rectangular prism of the appropriate dimensions, and secured with cellotape. The measured results for both are shown. Measurements were performed on the

waveguide and network analyser measurement system at the University of Stellenbosch, and also on a duplicate system of the same configuration at EMSS. These results are shown for the non-chiral steel unit cell.

The frequency at minimum transmission is interpreted as the resonant frequency of the unit cell. The measured resonant frequency for the copper chiral unit cell is 2.83 GHz, and for the two steel chiral unit cells 2.75 GHz and 2.81 GHz, deviating by a maximum of 1.8 % from the "designed" $f_0 = 2.8$ GHz, where f_0 is the resonant frequency in air for a single wire of length $L = \lambda/2$. The measured resonant frequency for the non-chiral unit cell is 2.75 GHz for the copper cell and 2.72 GHz for the steel cell, deviating by a maximum of 2.9 % from f_0. (Expressed as a wire length variation, a 1 mm change in wire length would result in a 1.8 % shift in resonant frequency, but the resonant frequency of the unit cell will probably not be solely determined by the length of a single hook.)

Discontinuities occurred in the measured data of the copper unit cells. This is probably an attribute of manufacture, since the copper wire is soft, and it was difficult to keep the wire legs straight and without irregularities.

The important difference in the behaviour of the copper and steel unit cells occurs around resonance. Where the copper unit cells show almost complete reflection (0.19 dB in the chiral unit cell and 0.35 dB in the non-chiral unit cell), the level of reflection for the steel cells is reduced to 2.1 and 2.8 dB in the two chiral unit cells and to 3.9 dB in the non-chiral unit cell. Away from resonance, the measurement does not distinguish significantly between the copper and steel unit cells.

4.5.3 The numerical experiments

The measured scattering parameters for the copper unit cells are compared to the FDTD predictions, using a wire conductivity of $\sigma_{\text{wire}} = 5.7 \times 10^7$ S/m (the conductivity of copper) and spatial discretization of $\Delta = 1$ mm, and $\Delta t = 1.926$ ps. The scattering parameters are shown for the copper chiral unit cell (Figure 4.8 and 4.9) and for the copper non-chiral unit cell (Figure 4.10 and 4.11).

The FDTD prediction for copper wire agrees well with the measured scattering parameters. For the chiral unit cell a resonant frequency of 2.86 GHz is predicted compared to the measured 2.83 GHz, and for the non-chiral unit cell, 2.79 GHz is predicted, compared to the measured 2.75 GHz, all within 2.1 % from the "designed" 2.8 GHz.

Although the effect is small for the copper wire, a small percentage of power is dissipated around resonance by the copper unit cells, due to the high yet finite conductivity of copper. A comparison of the level of maximum reflection coefficient gives an indication of the ability of the FDTD thin wire formulation for highly conducting wires to predict this effect, since when $E_{\tan} = 0$, total reflection is predicted. For the chiral unit cell the maximum level of reflection measured, is 0.19 dB ($|S_{11}| = 0.978$) and predicted, 0.23 dB ($|S_{11}| = 0.974$). For the non-chiral unit cell, 0.35 dB ($|S_{11}| = 0.961$) is measured and 0.27 dB ($|S_{11}| = 0.969$) predicted.

In the steel unit cells, a substantial amount of power is dissipated around resonance. Steel has a lower conductivity than copper and furthermore, the relative permeability of steel at microwave frequencies may be significantly different from unity, and frequency dependent [44, p. 42]. Using an average $|\mu_r|$ across the frequency band, the effect of the relative permeability could be interpreted as an effective conductivity $\sigma_{\text{eff}} = \sigma/|\mu_r|$ in the surface impedance model of a conductor,

$$(Z_i)_{\text{hf}} \approx \frac{1}{2\pi r_0}\sqrt{\frac{j\omega\mu_0}{\sigma_{\text{eff}}}}. \tag{4.3}$$

No successful attempt could be made to independently measure the effective conductivity

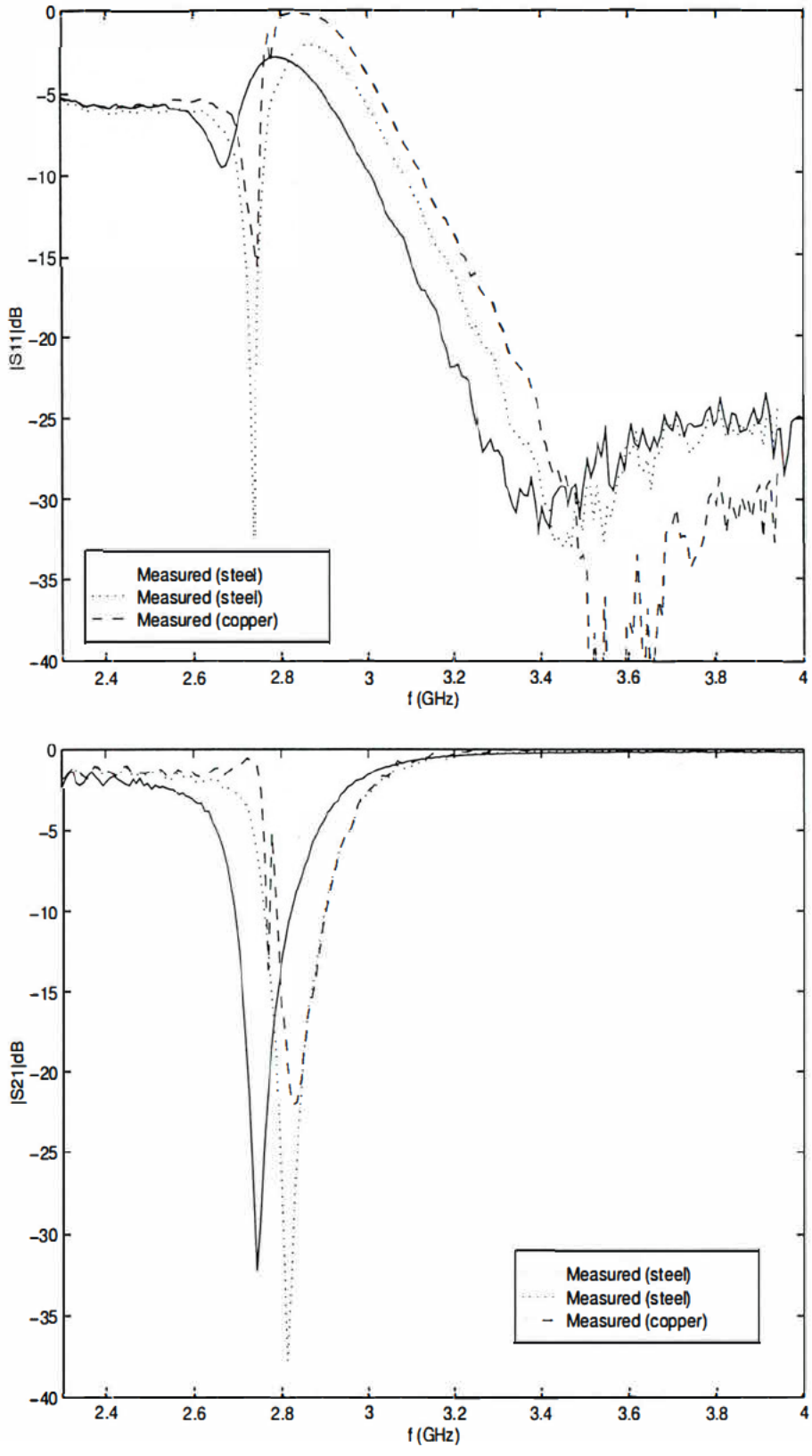

Figure 4.6: Point group 422 chiral unit cell. Copper and steel wire, in a polystyrene foam host. Measured magnitude of S_{11} and S_{21}. Two steel samples of the same design were manufactured, with the difference in the construction (··· hooks threaded through the host; — hooks positioned around a rectangular prism).

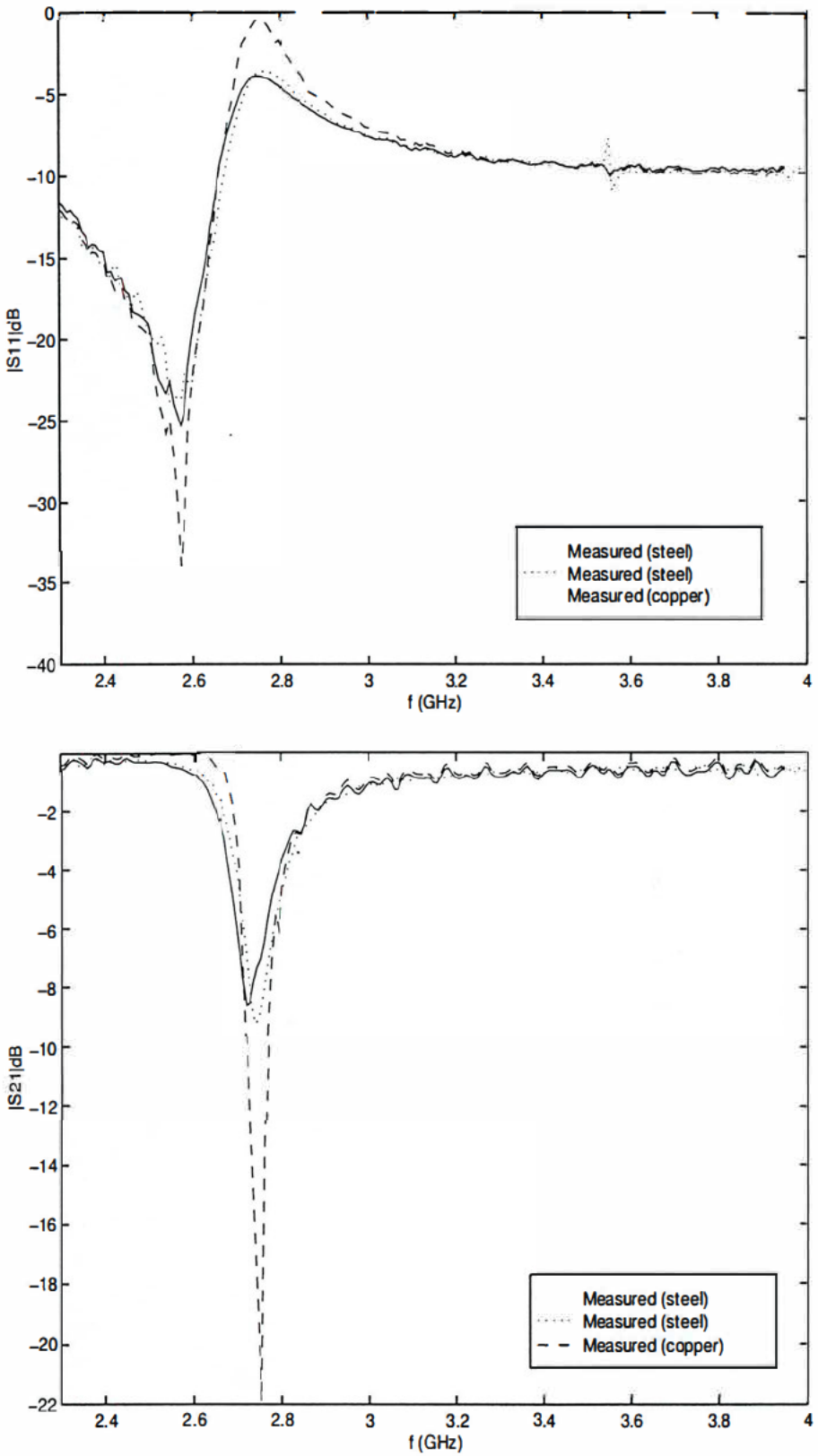

Figure 4.7: Point group $4/m$ chiral unit cell. Copper and steel wire, in a polystyrene foam host. Measured magnitude of S_{11} and S_{21}. The steel sample was measured on two measurement systems.

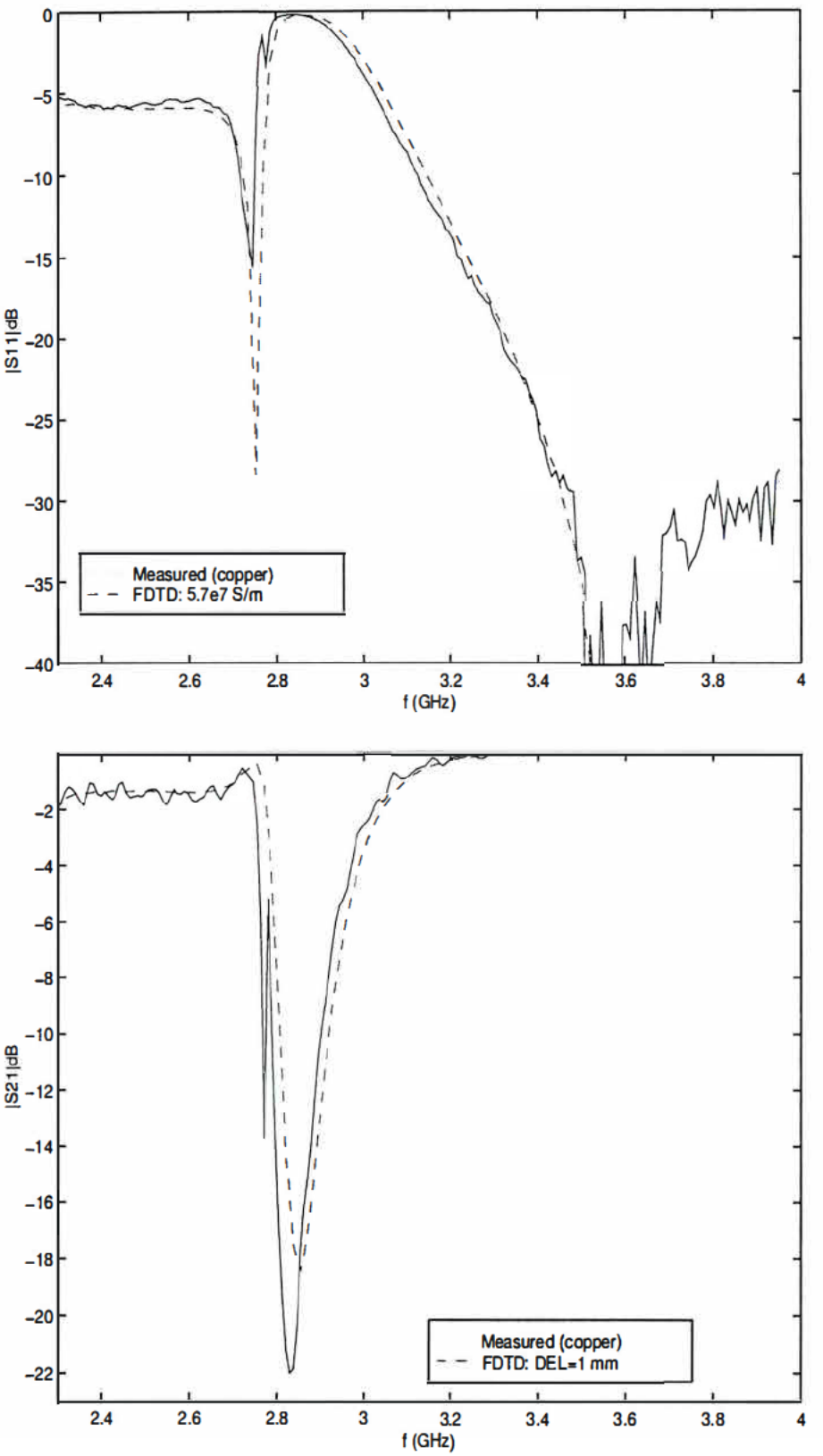

Figure 4.8: Point group 422 chiral unit cell, copper wire in a polystyrene foam host. Measured magnitude of S_{11} and S_{21} compared to the FDTD experiment, with $\sigma_{\text{wire}} = 5.7 \times 10^7$ S/m and $\Delta = 1$ mm.

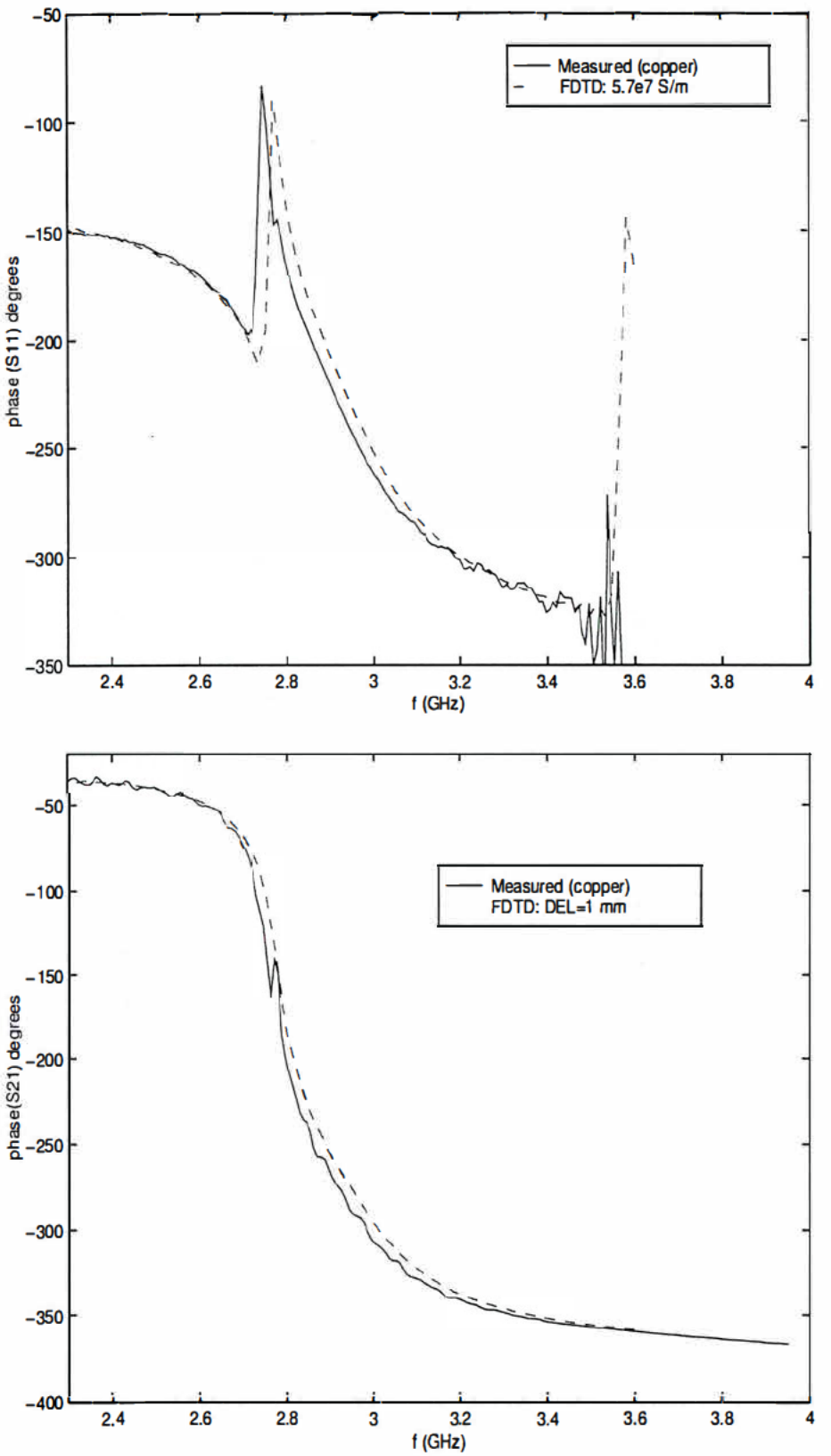

Figure 4.9: Point group 422 chiral unit cell, copper wire in a polystyrene foam host. Measured phase of S_{11} and S_{21} compared to the FDTD experiment, with σ_{wire} 5.7×10^7 S/m and $\Delta = 1$ mm.

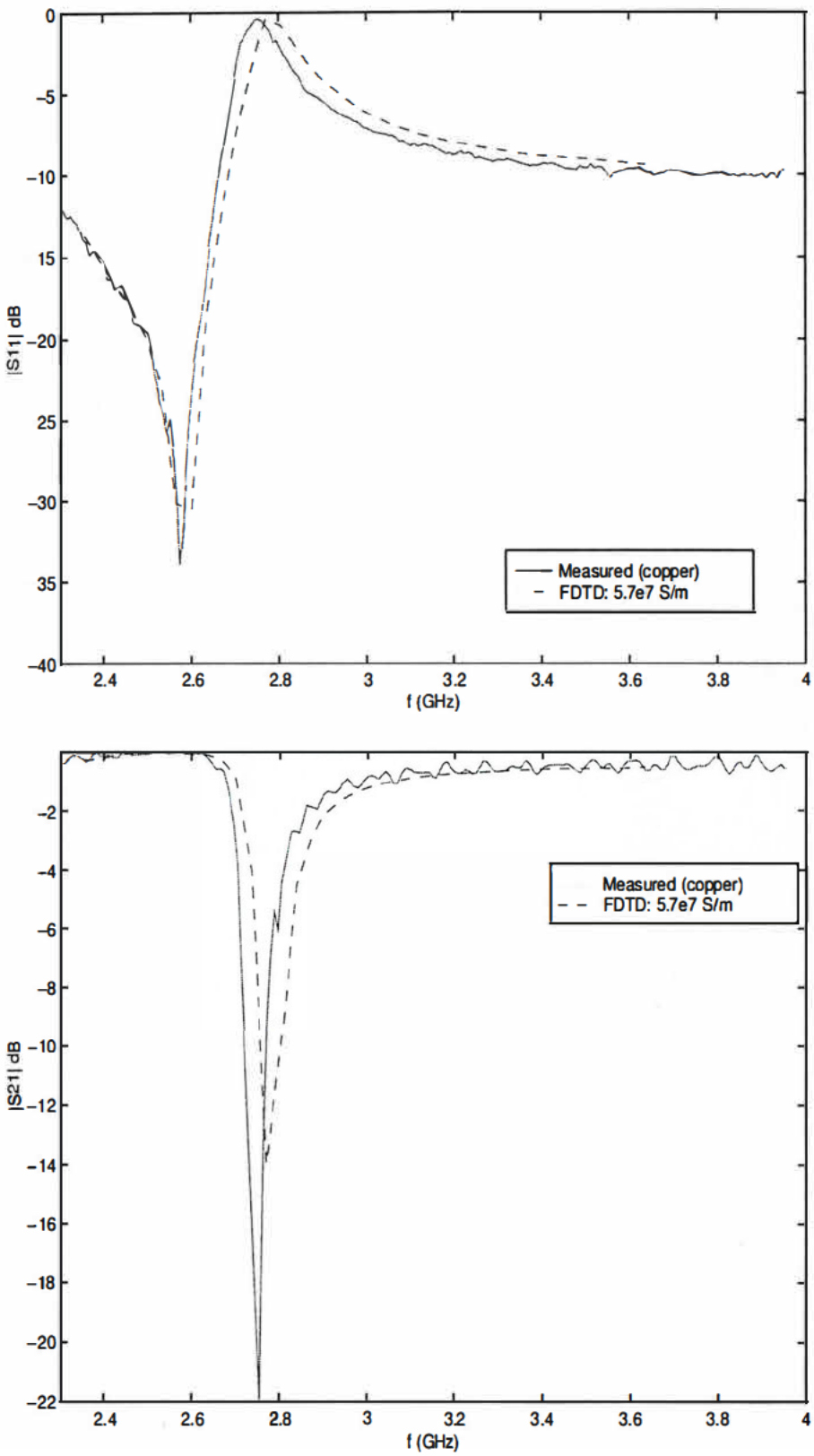

Figure 4.10: Point group $4/m$ non-chiral unit cell, copper wire in a polystyrene foam host. Measured magnitude of S_{11} and S_{21} compared to the FDTD experiment, with $\sigma_{\text{wire}} = 5.7 \times 10^7$ S/m (the conductivity of copper) and $\Delta = 1$ mm.

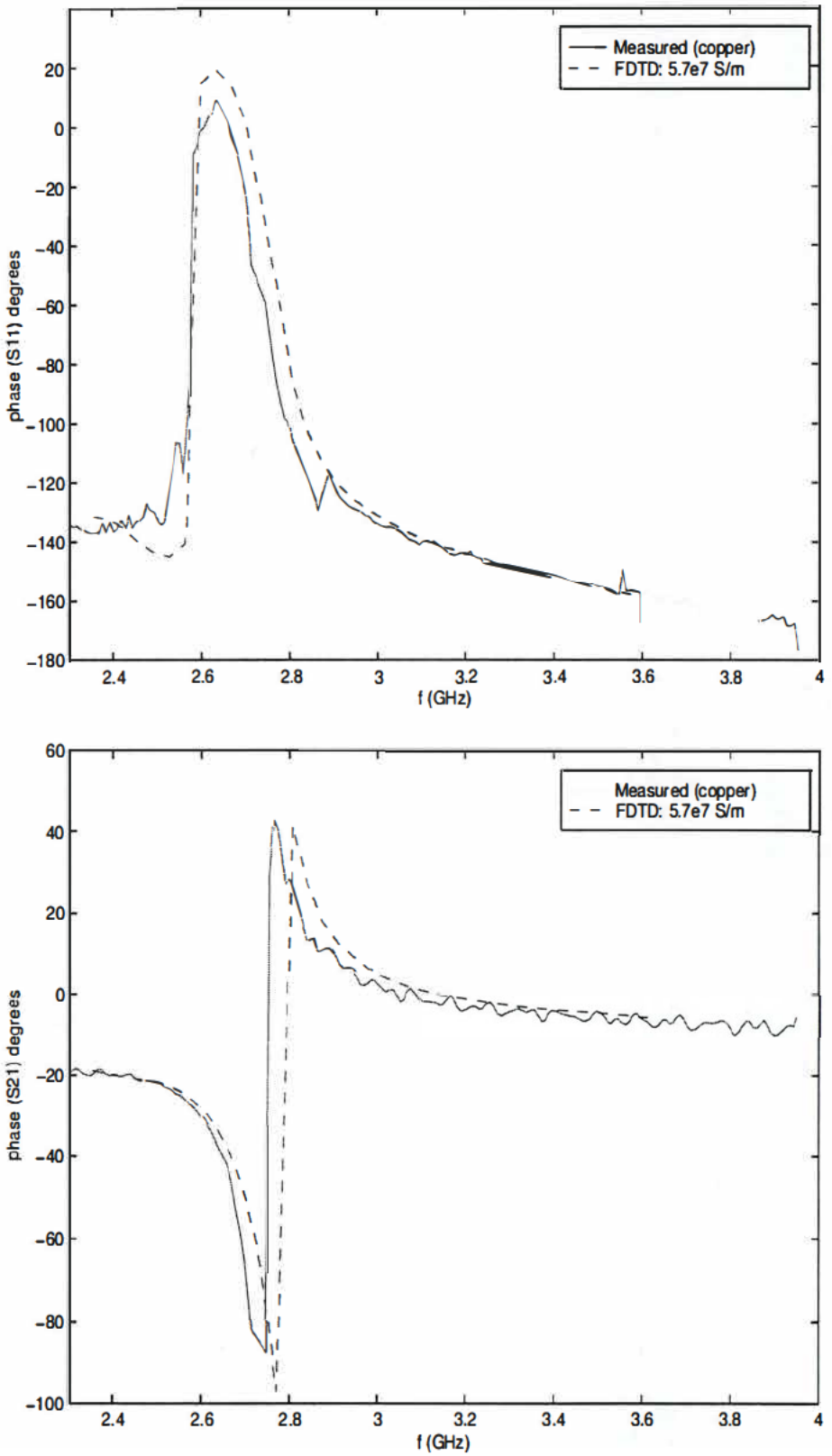

Figure 4.11: Point group $4/m$ non-chiral unit cell, copper wire in a polystyrene foam host. Measured phase of S_{11} and S_{21} compared to the FDTD experiment, with $\sigma_{\text{wire}} = 5.7 \times 10^7$ S/m (the conductivity of copper) and $\Delta = 1$ mm.

of the steel string at microwave frequencies. Two experiments in the rectangular waveguide were performed, and the scattering parameters were compared to the FDTD predictions and a moment method solution. A brief description of the experiments follows.

In the one experiment a conducting wire (both copper and steel) was spanned in the center of the rectangular waveguide. It was expected to observe the effect of the wire resistivity in the reflection coefficient. The moment method solution[5] predicted at 3 GHz a difference of 0.25 dB in the reflection coefficient between a wire with $\sigma = 10^7$ S/m and a wire with $\sigma = 10^5$ S/m, and the FDTD code predicted a difference of 0.28 dB. The moment method solution and FDTD solution (for $\Delta = 1$ mm) differ in the absolute value of the reflection coefficient by approximately 3 % for corresponding values of wire conductivity. The construction of the samples was not delicate enough to experimentally differentiate between the copper and steel wires.

In the other experiment a uniform grating of wires was spanned across the waveguide (one grating of 17 wires, 4 mm apart, and another grating of 35 wires, 2 mm apart). The wire grating acts as a surface impedance, and the more resistive the wires of the grating, the more transparent the grating becomes for an incident electromagnetic wave. In this experiment too, the measurement did not differentiate between a copper and a steel grating, although the measurement set-up is sensitive enough to detect the expected difference in the transmission coefficient. It is believed that the construction of the grating obscured the effect of the wire resistivity in some way. The measurement of the microwave properties of wires is an important practical problem, but is not pursued further.

The numerical experiment was repeated for a few values of effective conductivity ($10^7, 10^6, 10^5$ and 2×10^5 S/m). A conductivity of 2×10^5 S/m resulted in a fairly good agreement between measured and predicted scattering parameters for the chiral, racemic and non-chiral steel unit cells. The effective conductivity is smaller than the expected conductivity of steel, due probably to the relative permeability of steel at microwave frequencies.

The scattering parameters are shown for the steel chiral unit cell (Figure 4.12 and 4.13) and for the steel non-chiral unit cell (Figure 4.14 and 4.15).

The predicted and measured resonant frequencies are within 3 % from the "designed" 2.8 GHz. For the chiral unit cell, 2.81 and 2.74 GHz was measured and 2.82 GHz predicted; for the non-chiral unit cell, 2.72 GHz was measured and 2.75 GHz predicted.

The maximum reflection coefficient is significantly reduced by the steel wire. The predicted maximum reflection coefficient for the chiral unit cell, with $\sigma_{\text{eff}} = 2 \times 10^5$ S/m, is −2.36 dB ($|S_{11}| = 0.762$), compared to the measured values of −2.82 dB ($|S_{11}| = 0.723$) and 2.13 dB ($|S_{11}| = 0.783$). For the non-chiral unit cell 3.36 dB ($|S_{11}| = 0.679$) is predicted, compared to the measured −3.92 dB ($|S_{11}| = 0.637$).

It is illuminating to observe the percentage power absorbed by a unit cell of steel and copper wire in the rectangular waveguide. From the principle of energy balance, the percentage power absorbed by the sample is,

$$P_{\text{absorbed}} = \left[1 - \left(|S_{11}|^2 + |S_{21}|^2\right)\right] \times 100\,\%,$$

with only the TE_{10} mode propagating in the rectangular waveguide. The measured and predicted absorption are compared for the chiral unit cell in Figure 4.16 and for the non-chiral unit cell in Figure 4.17. The discontinuities in the measured scattering parameters of the copper chiral unit cell occurred around resonance, and are observed as a high absorption peak in Figure 4.16. A substantial amount of power is absorbed around resonance by the steel unit cells, and measurement and prediction with the fitted effective conductivity for steel are in good agreement with respect to maximum absorption and bandwidth.

[5] By Dr. Petrie Meyer.

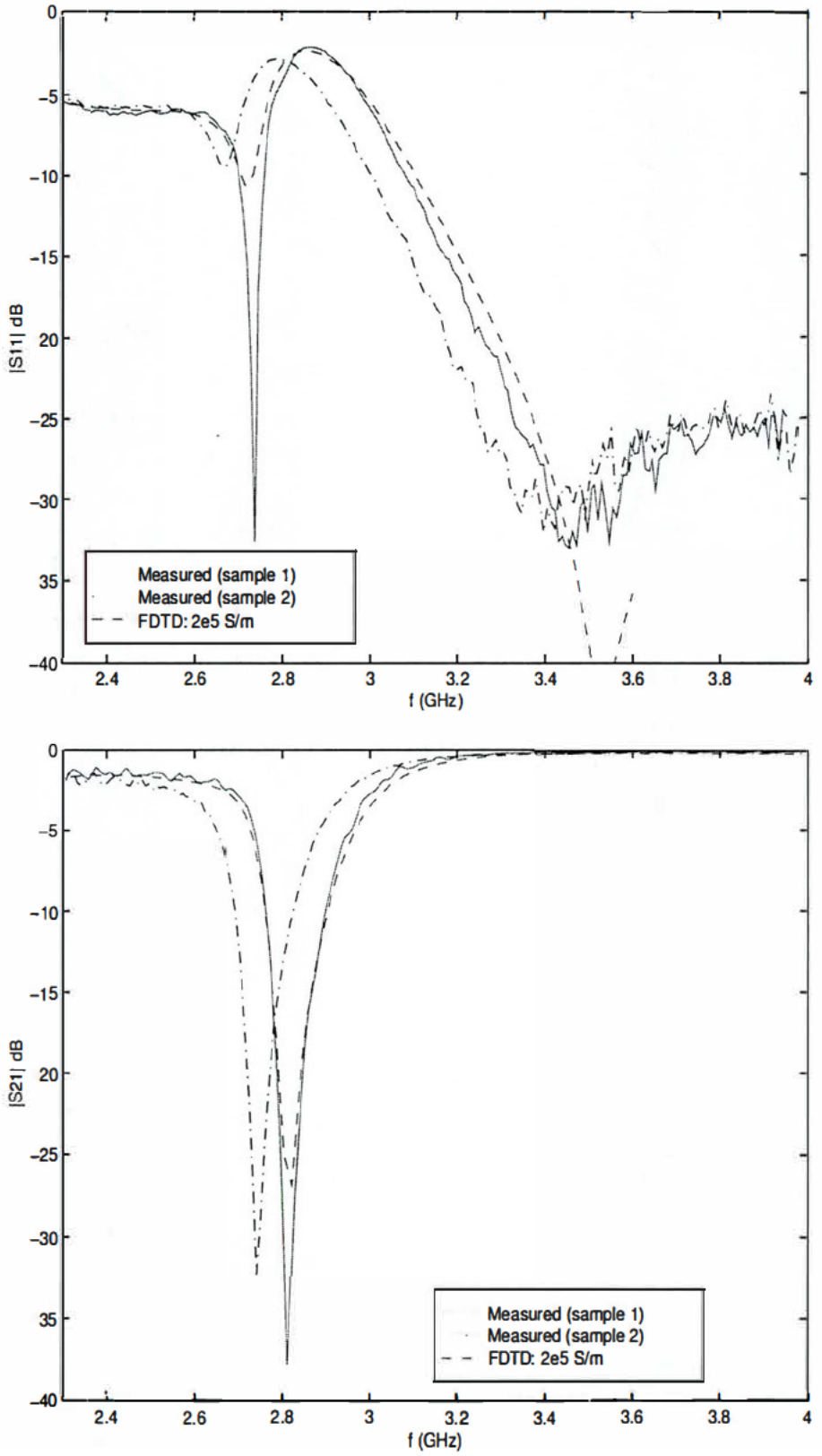

Figure 4.12: Point group 422 chiral unit cell, steel wire in a polystyrene foam host. Measured magnitude of S_{11} and S_{21} compared to the FDTD experiment, with $\sigma_{\mathbf{wire}} = 2 \times 10^5$ S/m and $\Delta = 1$ mm. Two steel samples of the same design were constructed.

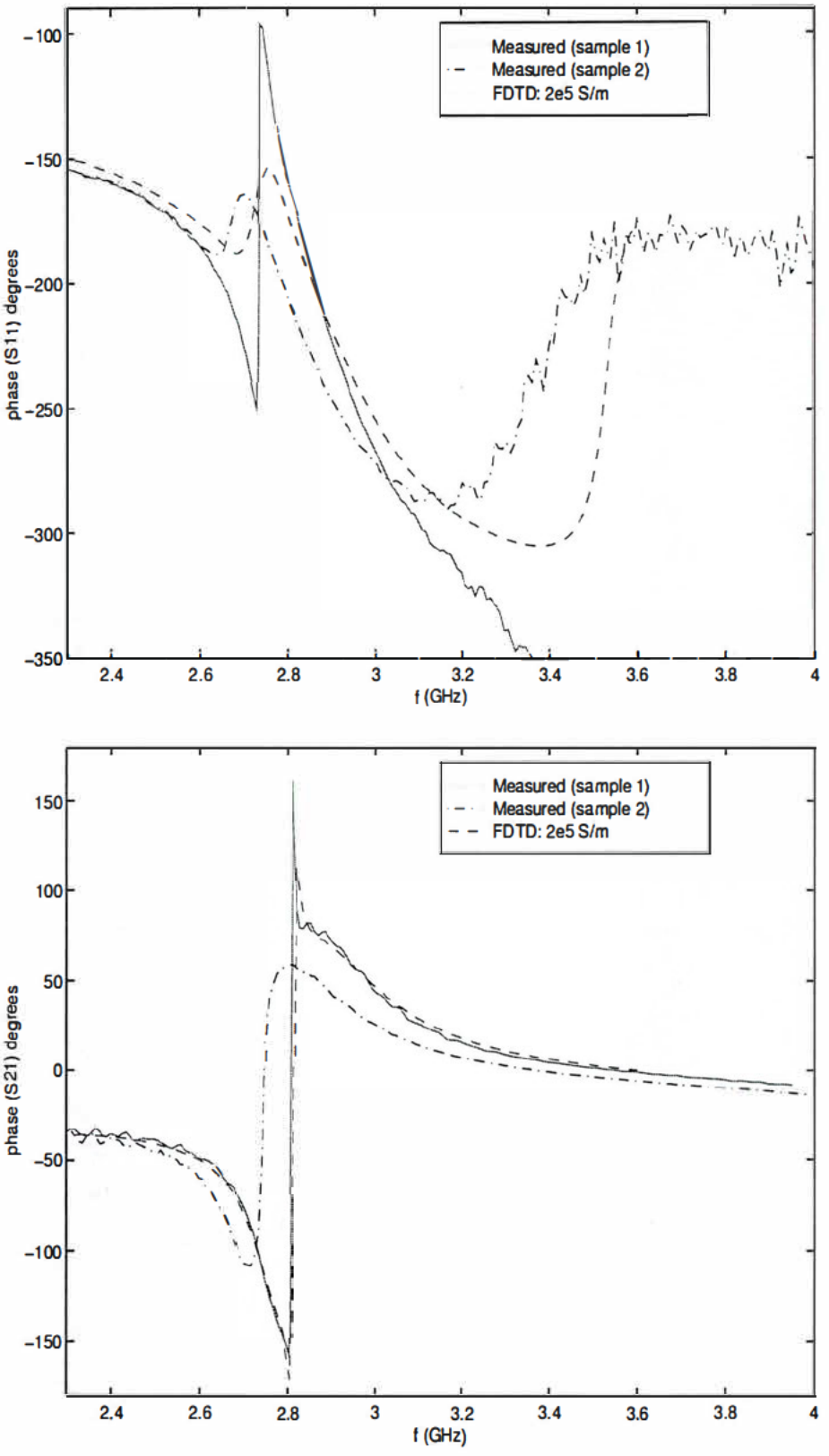

Figure 4.13: Point group 422 chiral unit cell, steel wire in a polystyrene foam host. Measured phase of S_{11} and S_{21} compared to the FDTD experiment, with $\sigma_{\text{wire}} = 2 \times 10^5$ S/m and $\Delta = 1$ mm. Two steel samples of the same design were constructed.

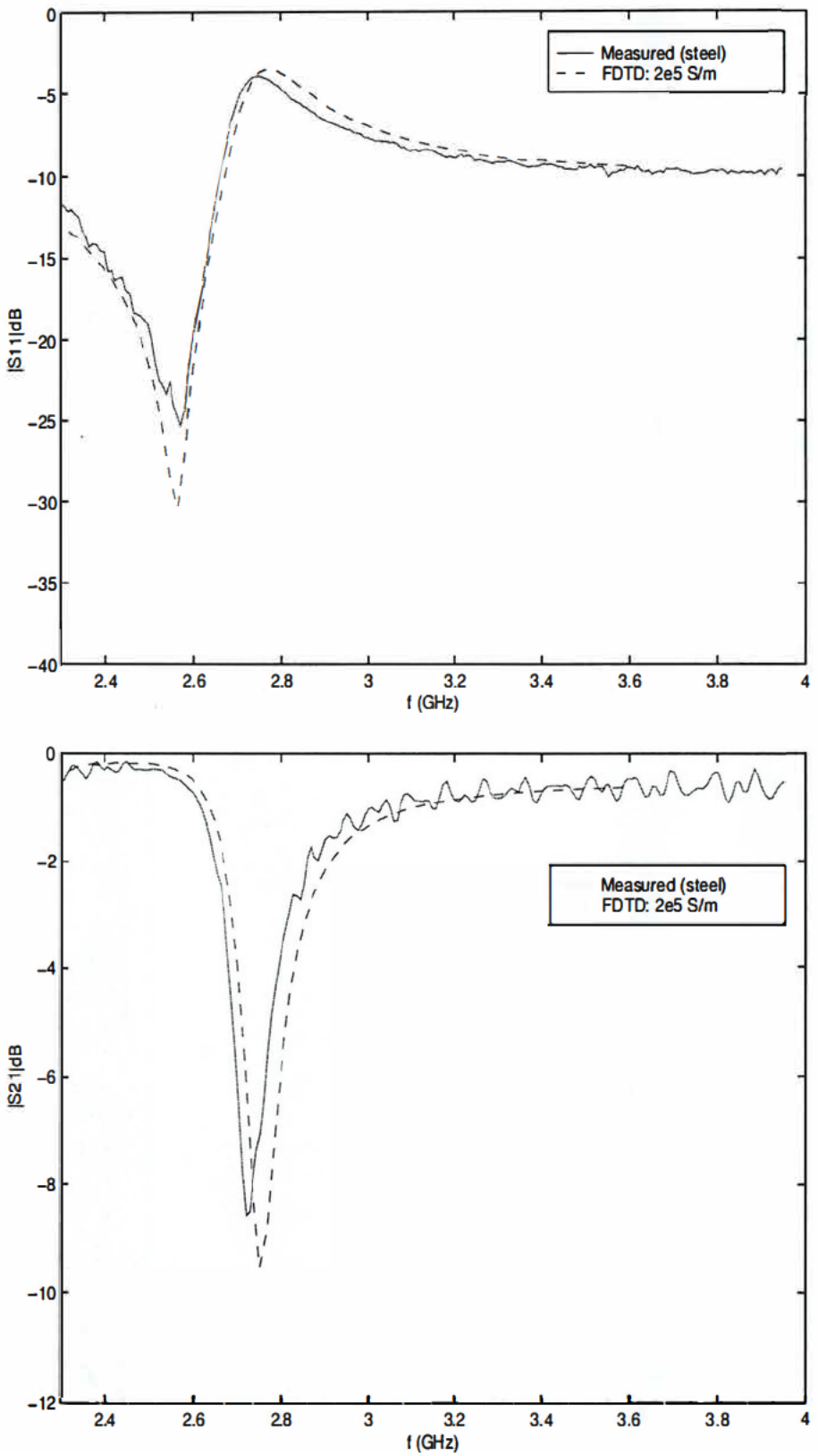

Figure 4.14: Point group $4/m$ non-chiral unit cell, steel wire in a polystyrene foam host. Measured magnitude of S_{11} and S_{21} compared to the FDTD experiment, with $\sigma_{\text{wire}} = 2 \times 10^5$ S/m and $\Delta = 1$ mm.

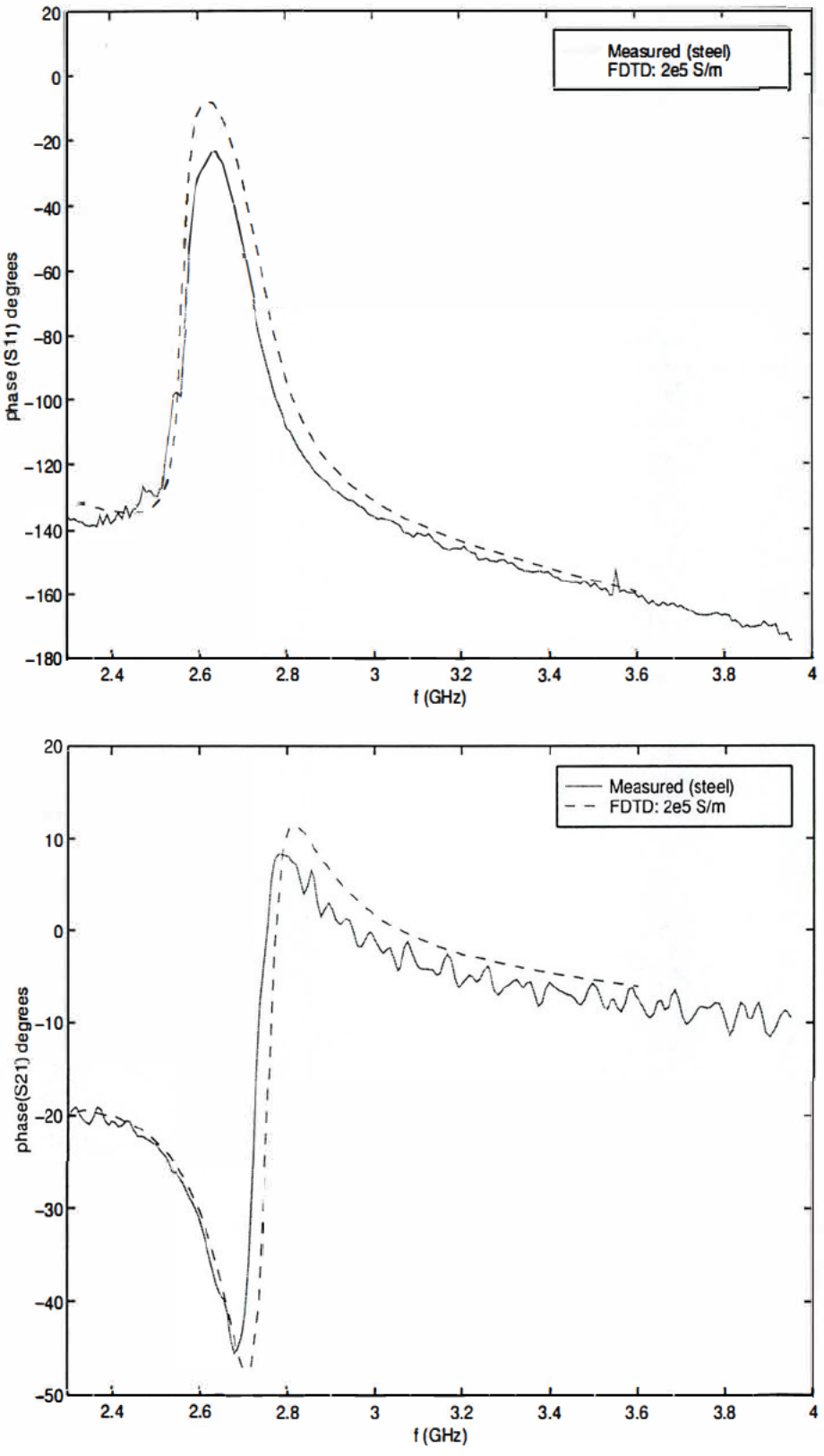

Figure 4.15: Point group $4/m$ non-chiral unit cell, steel wire in a polystyrene foam host. Measured phase of S_{11} and S_{21} compared to the FDTD experiment, with $\sigma_{\text{wire}} = 2 \times 10^5$ S/m and $\Delta = 1$ mm.

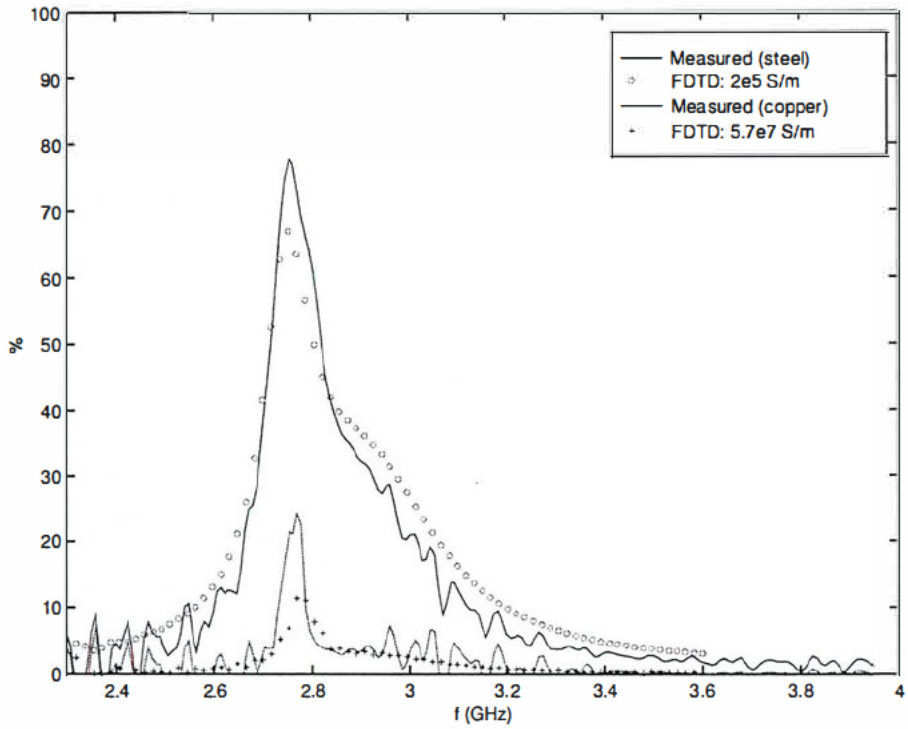

Figure 4.16: Point group 422 chiral unit cell. Percentage power absorbed by a copper and a steel unit cell of four chiral hooks in polystyrene foam, in the rectangular waveguide.

Note that in the standard FDTD formulation in which metallic conductors are modelled by $E_{\tan} = 0$, no power is dissipated by the unit cells in a lossless host.

Away from resonance, both measurement and FDTD prediction do not distinguish significantly between the copper and steel unit cells, e.g. for the non-chiral unit cell, at 3.6 GHz, $|S_{11}| = 0.331$ (9.6 dB) for both the copper and steel unit cells, and the FDTD prediction lies at 0.347 (9.2 dB) for the copper unit cell and 0.339 (9.4 dB) for the steel unit cell, i.e. within 2 % of the measured value.

Some remarks regarding the accuracy of the FDTD predictions and the spatial discretization are appropriate. The FDTD experiments discussed above were all conducted for a spatial discretization of $\Delta = 1$ mm, i.e. $\Delta \approx \lambda/76$ at the upper frequency limit of the TE_{10} mode. To investigate the sensitivity of the numerical results to the discretization, the numerical experiments were also performed with a discretization of $\Delta = 2$ mm. The results for the magnitude of the reflection coefficient are shown for the copper unit cells in Figure 4.18. The discretization affects the predicted scattering parameters around resonance, as well as away from resonance and the improved accuracy with the finer discretization is evident.

4.6 The wire crystals in an absorbing host

4.6.1 Characterization of the microwave absorber

The microwave absorbing host consists of graphite coated spherical balls of polystyrene foam and is characterised by a constant real permittivity and a constant conductivity across S-band. A slab of the material was cut to fit tightly into the rectangular waveguide. The thickness was measured as $d \approx 13.85$ mm. From the measured scattering parameters, the material parameters

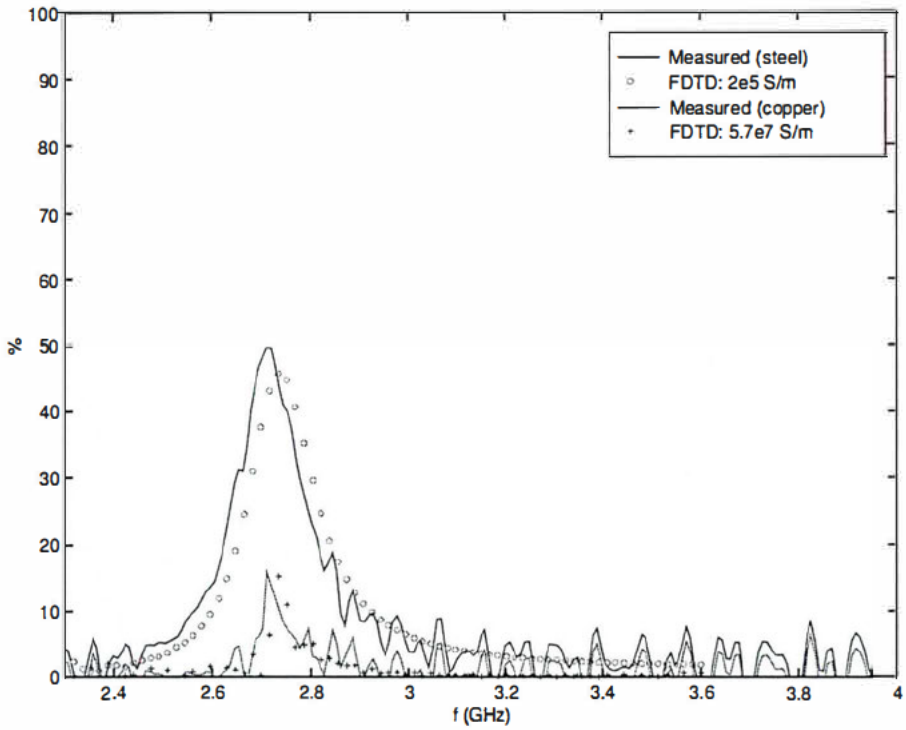

Figure 4.17: Point group $4/m$ non-chiral unit cell. Percentage power absorbed by a copper and a steel unit cell of four non-chiral hooks in polystyrene foam, in the rectangular waveguide.

were estimated with the model-based parameter estimation technique (and confirmed by the direct inversion technique) as $\epsilon_r \approx 1.67$, $\sigma \approx 0.04$ S/m, and $\mu_r \approx 1.0 - j0.0$. Uncertainties in the material thickness, surface roughness of the sample and a possible small offset in the position of the sample, add an error margin of about 10 % on the estimated material parameters.

4.6.2 Geometry

A resonance frequency of approximately 2.8 GHz in the microwave absorber determines $L = 42$ mm $= 3 \times 14$ mm, using the estimated material parameters, $\epsilon_r = 1.67$ and $\sigma = 0.04$ S/m. In the unit cell the resonance frequency will be determined by a combination of effects, such as the wire length and the absorber thickness and the element spacing. The unit cells were made of both steel and copper wire. The distance between the centre legs was kept at 26 mm. The hooks were positioned in the microwave absorber slab of dimensions 72 mm $\times$ 34 mm $\times$ 14 mm. (The absorber thickness is the same as the length of the centre leg of a hook.)

4.6.3 The experiments

All of the numerical experiments in the absorber were performed for a spatial discretization of 1 mm ($\Delta \approx \lambda/58$ at the upper frequency limit of the TE_{10} mode). All the numerical results are presented for the "designed" geometry, using the estimated material parameters ($\epsilon_r = 1.67$, $\sigma = 0.04$ S/m) and an effective absorber thickness of 14 mm. For the copper wire, $\sigma_{\text{wire}} = 5.7 \times 10^7$ S/m was used, and for the steel wire an effective conductivity of $\sigma_{\text{wire}} = 2 \times 10^5$ S/m was used, as determined in the experiments with steel in polystyrene foam.

Uncertainties in the manufactured absorber samples exist in the homogeneous composition of the absorber mixture and the position of the front and back legs of the hooks in the absorber-

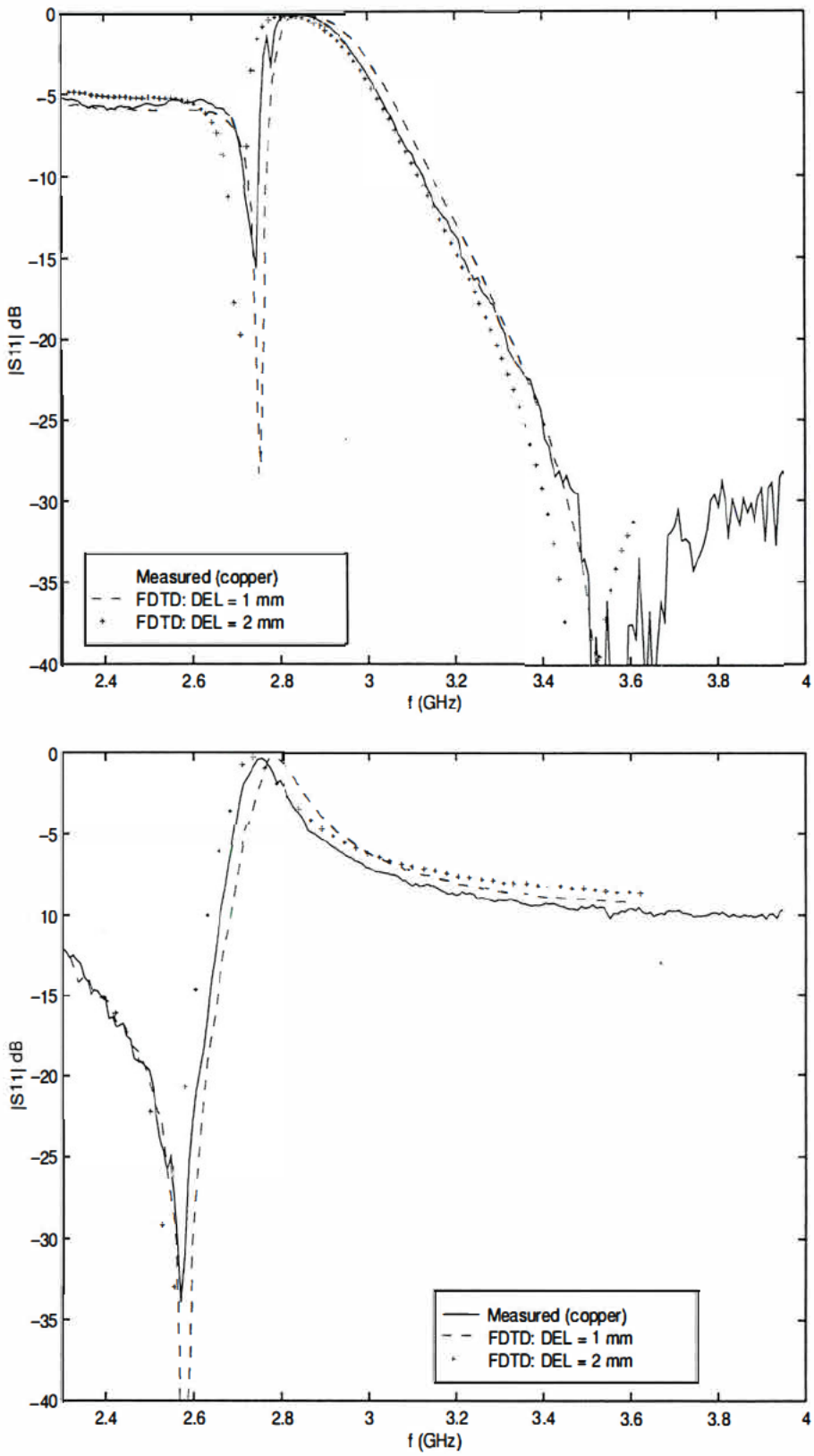

Figure 4.18: Effect of discretization on the accuracy of the numerical predictions. $|S_{11}|$ compared for $\Delta = 1$ mm and $\Delta = 2$ mm to the measured reflection coefficient of the chiral copper unit cell (top graph) and the non-chiral copper unit cell (bottom graph), in a polystyrene foam host.

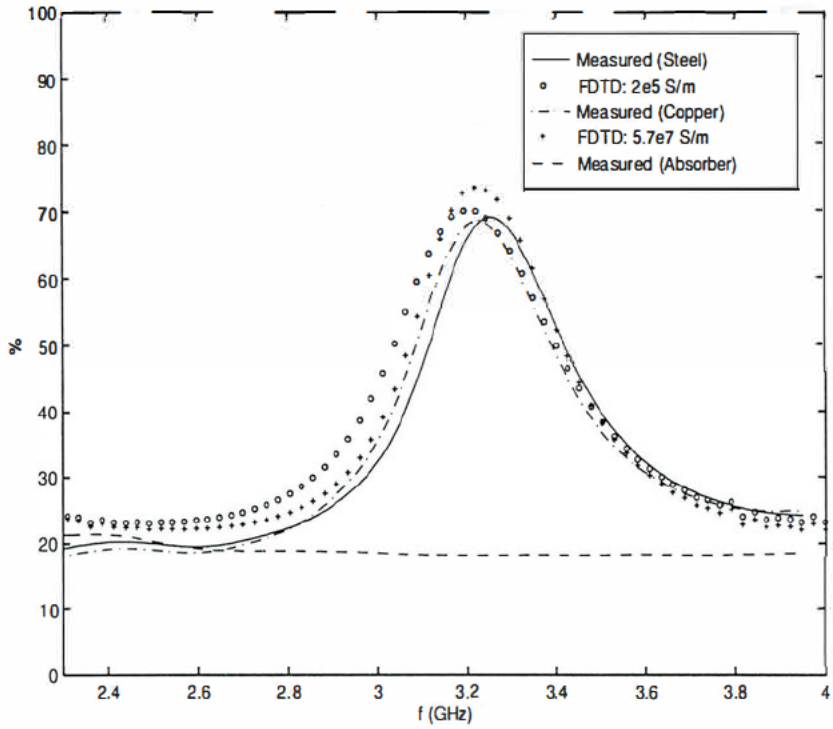

Figure 4.19: Point group 422 chiral unit cell in an absorber. Comparison of the percentage power absorbed by a copper and a steel unit cell, measured and predicted.

air interface. The numerical simulations indicated great sensitivity of the scattering parameters to the absorber thickness and the position of the unit cell in the absorber. A detail comparison of the scattering parameters would therefore not be meaningful. More clearly and informative is a comparison of the power absorbed by the different unit cells. The measured and predicted scattering parameters are compared graphically in Appendix A for all the experiments.

Unlike the experiments with the wire crystals in a lossless host, the distinction between the copper and steel unit cells in the absorbing host is not very prominent. Comparing the measured percentage power absorbed by the copper and steel chiral unit cells in the absorber (Figure 4.19), both cells absorb a maximum of 69% of the power, with a half power bandwidth of 17 %. It seems that the properties of the wire are masked by the absorber surrounding the wire in the absorption of the power. This is confirmed by the measurements on the non-chiral unit cells (Figure 4.20), with an absorption peak of 56 % and 57 % with a half power bandwidth of 17 % for the copper and steel unit cells. In the numerical comparison between the copper and steel unit cells, a higher absorption peak and narrower bandwidth is predicted for the copper cells (2 to 4 % difference compared to the steel cells).

The differences between the predicted and measured absorption by the unit cells in absorber are of the order 1 % to 5 %, with respect to maximum absorption, frequency of maximum absorption, bandwidth, and absorption away from resonance. In the light of the uncertainties in the actual absorber properties, manufacture tolerances, and approximations in the numerical formulation, e.g. the simple absorber material model of a complex mixture, the uncertainty of the position of the unit cell in the effective numerical absorber length, and approximations in the thin wire formulation for updating the current in the wire, the differences are acceptable.

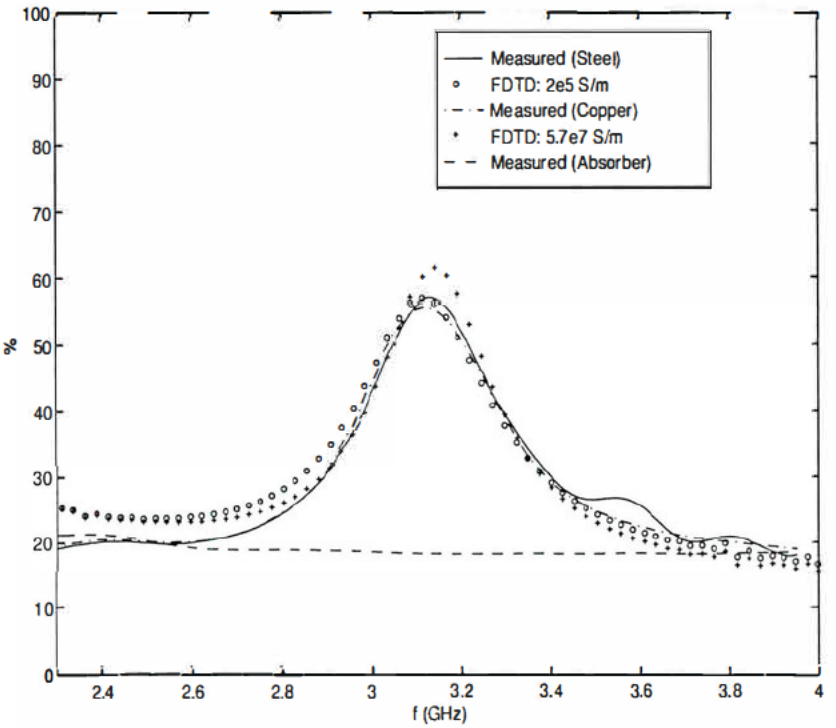

Figure 4.20: Point group $4/m$ non-chiral unit cell in absorber. Comparison of the percentage power absorbed by a copper and a steel unit cell, measured and predicted. (The use and removal of glue in the steel sample caused some damage to the sample, noted in the curve above 3.4 GHz.)

4.7 Conclusions

The experiments with resonant copper and steel wire hooks in polystyrene foam indicated that the finite conductivity of wires, especially around resonance, significantly affects the scattering parameters and absorption by a unit cell of four hooks in the rectangular waveguide. A high frequency surface impedance model for round conductors has been incorporated into the FDTD subcell thin wire formulation, and good agreement was obtained between measurement and FDTD prediction for copper wire. A good fit could be obtained for the steel unit cells, suggesting an effective conductivity of the order 2.0×10^5 S/m for the guitar steel string. There is a maximum difference of approximately 3 % between the measured and predicted resonant frequencies. This could be due to a similar error in the measured physical length of the hooks (as indicated by the measurement of the two chiral samples of the same geometry), or an end effect resulting in a different effective wire length from the physical length or due to approximations of the thin wire formulation (indicated by the effect of the spatial discretization), or a combination of these effects. It is not particularly important for this study.

The experiments in an absorbing host indicated that the absorber properties overshadow the properties of the wire in the absorption of the power by a unit cell of four hooks. The differences of the order 1 % to 5 % between the predicted and measured absorption by the unit cells are acceptable in the light of the uncertainties mentioned in the previous section. The significant conclusion is that the inclusion of resonant wire structures in a microwave absorber enhances absorption, and that the properties of the wire are not of much importance, except that it should be a good conductor, and this is drawn both from the measured and the predicted

results.

In a typical experiment and for a spatial discretization of $\Delta = 1$ mm, the size of the waveguide was $73 \times 35 \times 500$ cells, requiring 258 Megabytes of memory at single precision, and the run time for 15000 time steps was 5 hours 45 minutes on a Silicon Graphics Origin 200 machine. It is a two-processor R10000 machine with 320 MB RAM. Refer to Section 3.5.3 for the remark on more efficient memory usage. (By restricting the length in the waveguide in which thin wires may be present to 50 mm, the memory usage can be reduced by more than a factor of 4.) The formulation was also checked for stability. It remained stable in a simulation of 20000 time steps.

With these experiments of varied geometry, wire properties and host properties for resonant wire unit cells in a rectangular waveguide, the FDTD subcell thin wire formulation for highly conducting wires predicts the scattering with respect to magnitude, phase and absorption remarkably well.

Chapter 5

Wire crystals and their absorption

5.1 Wire crystals in a square waveguide

With the FDTD code well substantiated, it can be used to closely study the behaviour of resonant wire inclusions in a host. The experiments are performed to obtain an understanding of the absorption mechanisms in crystals of chiral and non-chiral wire structures. Four closely related uniaxial crystals in the tetragonal crystal system were classified in Chapter 2.

1. A chiral unit cell of point group 422 symmetry.
2. A non-chiral unit cell of staples of point group $4/m$ symmetry.
3. A non-chiral unit cell of cranks of point group $\bar{4}$ symmetry.
4. A racemic unit cell of enantiomorphous chiral hooks of point group $\bar{4}$ symmetry.

The crystals all have a 4-fold or $\bar{4}$-fold principal symmetry axis. In order to maintain the 4-fold symmetry in the waveguide, a unit cell is centered in a square waveguide, with the 4-fold axis of the crystal coincident with the (4-fold) waveguide axis (Figure 5.1). Synthetic chiral microwave absorbers consist usually of a conventional microwave absorber which contains suitable macroscopic conducting chiral objects. The absorption of an electromagnetic wave is studied in square waveguide for the unit cells of *resonant* copper hooks, embedded in a microwave absorbing host. The experiments in rectangular waveguide of steel wire hooks in polystyrene foam showed that the ohmic loss in resonant wire hooks of finite conductivity in an otherwise essentially lossless environment is significant. Therefore unit cells of *resonant* steel hooks in air are also studied for their absorption.

The geometrical arrangement of the hooks in a unit cell influences how the unit cell behaves in its interaction with an electromagnetic wave. Without changing the symmetry, there are still many parameters defining the unit cell's geometry which are not determined, e.g. the total length of a hook, the spacing between hooks, the wire diameter, and the spacing between unit cells. Infinitely many arrangements are possible. These parameters concern the detail behaviour of the wire crystals, and what may be optimum for one (from an absorption point of view), may not be optimum for another, although the crystals are geometrically closely related.

Two more experiments in a square waveguide are performed on the 422 chiral unit cell of chiral hooks and the $4/m$ non-chiral unit cell of staples to touch on the detail influence of the arrangement of the hooks. The one experiment is a study of the interaction between the unit cells as a function of their spacing, and their repetition, by arranging four unit cells in the square waveguide (Figure 5.2). The other experiment is a parametric study of the absorption by a unit cell of steel wire as a function of the spacing between the hooks in the unit cell (Figure 5.3).

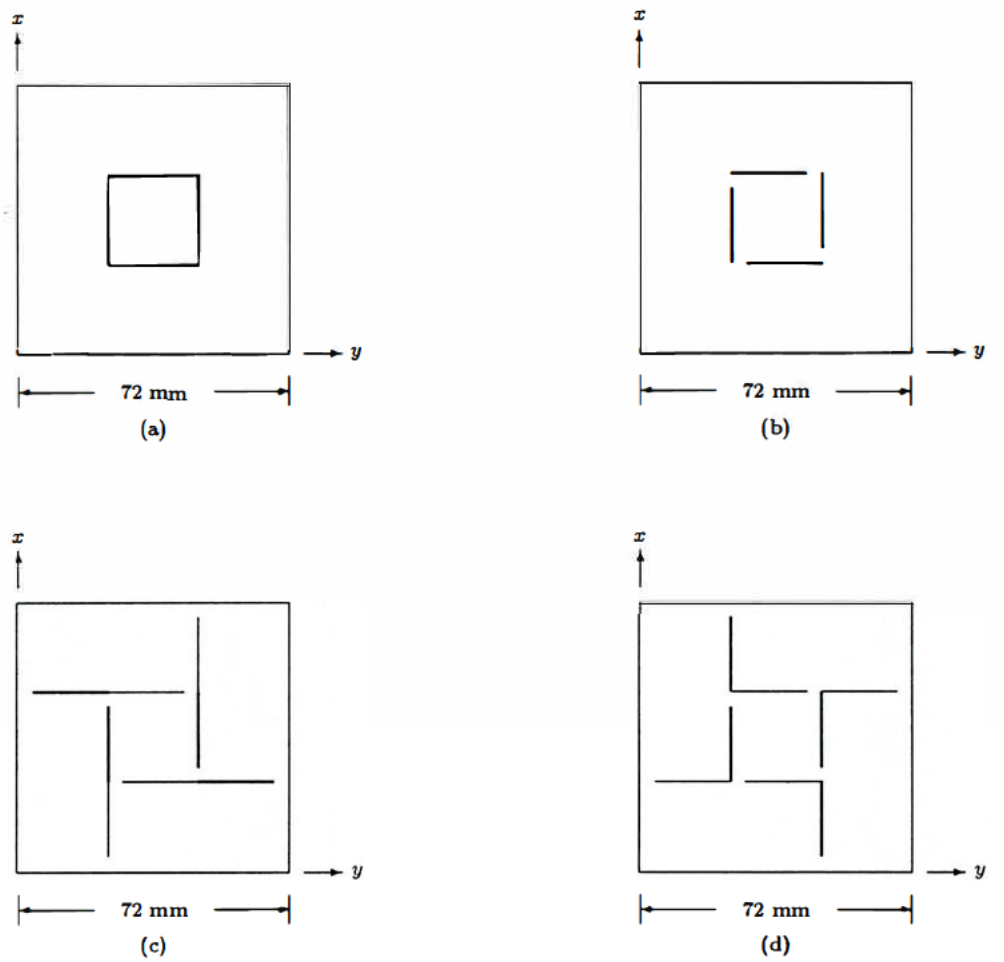

Figure 5.1: Diagrams of the wire unit cells in a square waveguide. Thick lines represent the front legs and thin lines represent the back legs. (a) 422 Chiral unit cell. (b) $4/m$ Non-chiral unit cell of staples. (c) $\bar{4}$ Non-chiral unit cell of cranks. (d) $\bar{4}$ Racemic unit cell of enantiomorphous hooks.

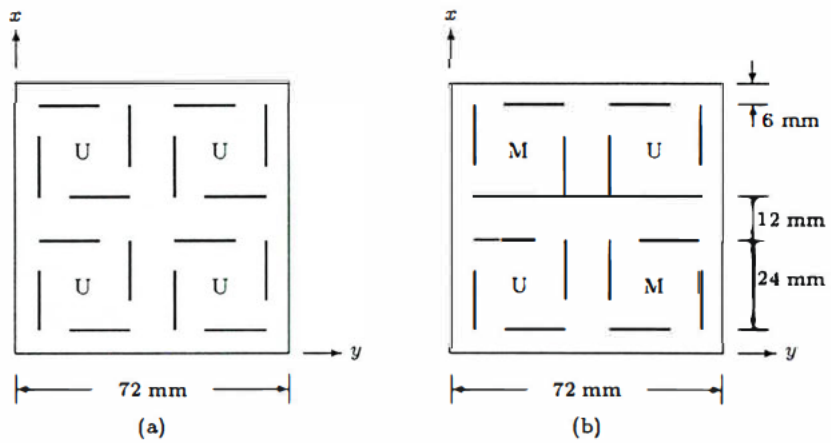

Figure 5.2: Front view diagram of four unit cells arranged in the square waveguide. The unit cell (either the 422 chiral unit cell or the $4/m$ non-chiral unit cell) is marked by a "U" and the mirror image of the unit cell by an "M". (a) Four identical unit cells. (b) Four unit cells, related by two orthogonal mirror planes.

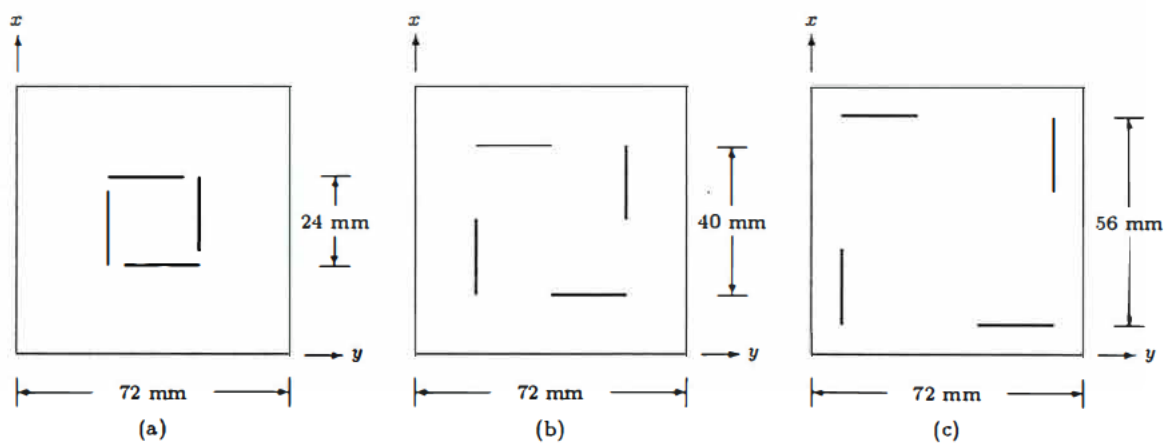

Figure 5.3: Front view diagram for the 422 and $4/m$ unit cells in a square waveguide, with spacings of (a) 26 mm, (b) 40 mm and (c) 56 mm between the centre legs in each unit cell. The length of each hook remains unaltered.

5.2 Through the waveguide looking-glass

With apology to Lewis Carroll.

5.2.1 The waveguide perspective

The wire crystals are viewed in a square waveguide. The perspective is therefore of a crystal surrounded by conducting boundaries, and illuminated by a non-uniform plane wave. The amplitude distribution of the electric field in the TE_{10} mode in a transverse plane in the waveguide is uniform in the direction of the E-field, and sinusoidal in the direction orthogonal to the E-field polarization. The wire crystal in the waveguide may selectively excite some other modes, e.g. a chiral crystal is expected to excite the TE_{01} mode. Other modes may propagate if they are excited, and if the waveguide dimension is sufficiently large. Otherwise, at frequencies below cutoff, the modes are evanescent, and do not transport energy.

5.2.2 Another perspective: the infinitely imaged crystal at oblique incidence

A well-known alternative view of propagation in rectangular waveguide is to consider the TE_{10} mode as two uniform plane waves obliquely incident from two angles, θ and $-\theta$, defined relative to the waveguide axis, with the direction of propagation in planes parallel to the broadwall of the rectangular waveguide, e.g. [27, pp. 426 428]. The E-field is polarized normal to the plane of incidence [27, p. 398]. The angle of incidence is given by the relation $\sin\theta = \frac{\lambda}{\lambda_c}$, where λ_c is the cutoff wavelength for the incident mode, and λ is the free space wavelength. The two plane waves form a regular pattern of null planes by their interference, where $E_{\tan} = 0$. Perfectly conducting walls at these planes will not disturb the fields.

The crystal in the waveguide can be visualized as an infinite array of imaged unit cells (Figure 5.4), illuminated at oblique incidence. The perfectly conducting waveguide walls represent mirror planes for the unit cell, adding to the symmetry of the crystal.

A plane wave incident on a wire crystal will be reflected, refracted and diffracted. In general, a periodic array or grating of wires reradiates or diffracts a plane wave incident upon it into various directions [27, pp. 305-306], described as the diffraction orders of the grating. The possible directions for the transmitted wave (θ_2) are those for which the phase constants along the grating match on the two sides. For a simple grating of evenly spaced elements, separated by a distance d, and illuminated at an angle θ, this requires $kd \sin\theta = kd \sin\theta_2 \pm 2m\pi$, (m=0, 1, 2, ...), where k is the free space wave number. The principal order is $m = 0$ when $\theta_2 = \theta$. Other diffraction orders or grating lobes may exist, provided that $|\sin\theta_1 \pm m\lambda/d| \leq 1$.

If the elements of the array are sufficiently closely spaced in terms of wavelength, no grating lobes are formed, and the angle for each reflected wave is equal and opposite to the incident wave angle, and the angle for each transmitted wave is equal to the angle of the incident wave. By virtue of symmetry, the reflection coefficients and the transmission coefficients are identical for the two incident plane waves, and the null planes formed by the reflected and transmitted waves coincide with the null-planes of the incident waves. Perfectly conducting walls at these planes will not disturb the fields anywhere, because they are also at symmetry planes of the array elements. By superposition, the reflection and transmission coefficients of the combined waves are identical to that of the individual waves. If the spacing between the array elements is large enough in terms of wavelength, grating lobes may be excited. Grating lobes correspond to higher order modes in the waveguide.

These principles are exploited in the waveguide simulator, developed at Wheeler Laboratories, to determine the performance of large planar phased-array antennas [45].

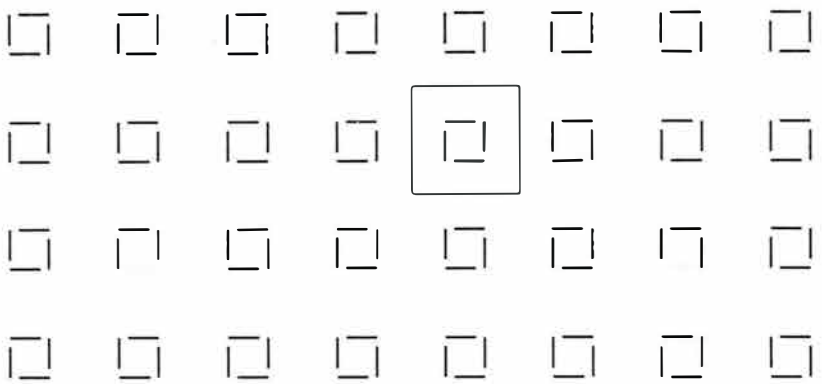

Figure 5.4: Diagram of an infinitely imaged wire crystal (front view). One "unit cell" in the waveguide simulator is indicated.

The crystals have been classified in Chapter 2 according to the point group symmetry of a unit cell of four hooks. This is the symmetry of a crystal formed by the translation of the unit cell along the crystallographic axes. From the perspective of the waveguide simulator, the crystal is formed by an interleaved translation of the "unit cell" and the imaged "unit cell". The imaged crystal therefore has the additional symmetry of two orthogonal mirror planes, and the point group symmetry is different from the crystal formed by the translation of the unit cell alone. The imaged crystals are still of the tetragonal crystal system, and therefore optically uniaxial.

5.3 FDTD waveguide configuration

The lowest cutoff frequencies for a 72 mm × 72 mm square waveguide are shown below.

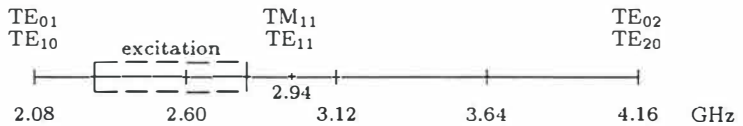

The crystals are illuminated with the TE_{10} mode. The incident field has a frequency spectrum between 2.3 and 2.8 GHz, therefore only the TE_{10} and TE_{01} modes can propagate. The reflected and transmitted electric fields are sampled for the y (TE_{10} mode) and x (TE_{01} mode) components at the centre of a transverse plane in the waveguide, at a distance of 400 mm from the front and back of the unit cell. The next higher order modes are the TE_{11} and TM_{11} modes. They are evanescent in this frequency spectrum, and at the sampling distance are sufficiently attenuated by a factor of $e^{-\alpha_{11} z} = 0.0005$ at 2.8 GHz. A spatial discretization of $\Delta = 2$ mm is used, and a time step $\Delta t = 3.85$ ps to comply with the Courant stability criterion for the FDTD time stepping. (At 2.8 GHz $\Delta \approx \lambda/53$ in air and $\Delta \approx \lambda/41$ in the absorbing host.)

Viewed as an infinitely imaged crystal, illuminated at oblique incidence, θ varies from 65° to 48° for frequencies varying from 2.3 to 2.8 GHz in the 72 mm waveguide.

5.4 The experiments

5.4.1 The four uniaxial crystals in a square waveguide

The absorption by the four uniaxial crystals of resonant hooks is considered in a square waveguide. Unit cells of copper wire embedded in a microwave absorbing host and unit cells of steel wire in air are studied. Diagrams of the wire unit cells centered in a square waveguide are shown in Figure 5.1.

Copper unit cells embedded in a microwave absorber

Each hook has a total length of $L = 3 \times 16$ 48 mm ($f_0 \approx 2.4$ GHz), and the centre legs of the hooks are separated by 24 mm in a unit cell. A unit cell is embedded in a microwave absorber with an effective thickness of 18 mm, and material parameters $\epsilon_r = 1.67$ and $\sigma = 0.04$ S/m. The wire conductivity is $\sigma_{\text{wire}} = 5.7 \times 10^7$ S/m and the wire radius is 0.15 mm. The magnitudes of the scattering parameters are shown in Appendix C, Figures C.1 C.4.

Steel unit cells in air

Each hook has a total length of $L = 3 \times 20$ 60 mm ($f_0 \approx 2.5$ GHz), and the centre legs of the hooks are separated by 24 mm in a unit cell. The wires have the effective conductivity of the guitar steel string, $\sigma_{\text{wire}} = 2 \times 10^5$ S/m and a radius of 0.15 mm. The magnitudes of the scattering parameters are shown in Appendix C, Figures C.5 C.8.

5.4.2 Four unit cells in a square waveguide

The absorption is considered for a system of four unit cells in the square waveguide, arranged to maintain four fold symmetry. In the one arrangement four identical unit cells are studied, in the other arrangement the four unit cells are related by two orthogonal mirror planes. A front view diagram is shown in Figure 5.2. The experiment is performed with the 422 unit cell and the $4/m$ unit cell, both of copper wire embedded in a microwave absorber and of steel wire in air.

Copper unit cells embedded in a microwave absorber

Each hook has a total length of $L = 3 \times 16 = 48$ mm, and the centre legs are separated by 24 mm. A unit cell is embedded in a microwave absorber with an effective thickness of 18 mm, and material parameters $\epsilon_r = 1.67$ and $\sigma = 0.04$ S/m. The wire conductivity is $\sigma_{\text{wire}} = 5.7 \times 10^7$ S/m and the wire radius is 0.15 mm. The magnitudes of the scattering parameters are shown in Appendix C, Figures C.9–C.12.

Steel unit cells in air

Each hook has a total length of $L = 3 \times 20$ 60 mm, and the centre legs are separated by 24 mm. The wire conductivity is $\sigma_{\text{wire}} = 2 \times 10^5$ S/m and the wire radius is 0.15 mm. The magnitudes of the scattering parameters are shown in Appendix C, Figures C.13–C.16.

5.4.3 Wider spacing between the hooks

A parametric study of the absorption by the 422 chiral unit cell and the $4/m$ non-chiral unit cell of steel hooks, as a function of the spacing between the hooks in a unit cell, was performed in the square waveguide. The unit cells were analysed for a spacing of 24 mm, 40 mm, and 56

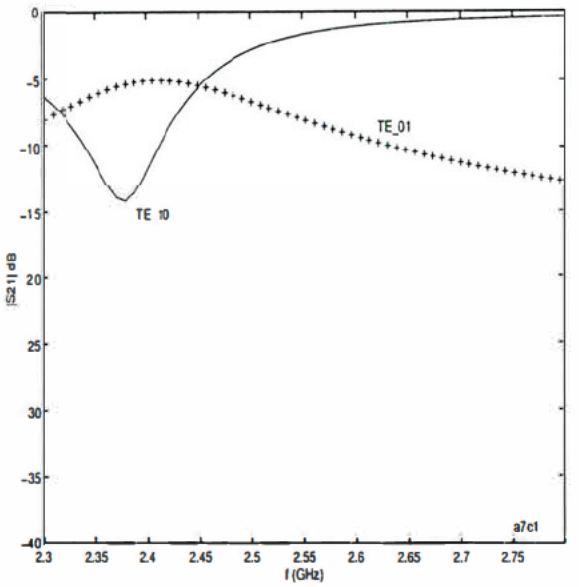

Figure 5.5: Transmission coefficient for the 422 chiral steel unit cell in air. The crystal is illuminated with the TE_{10} mode.

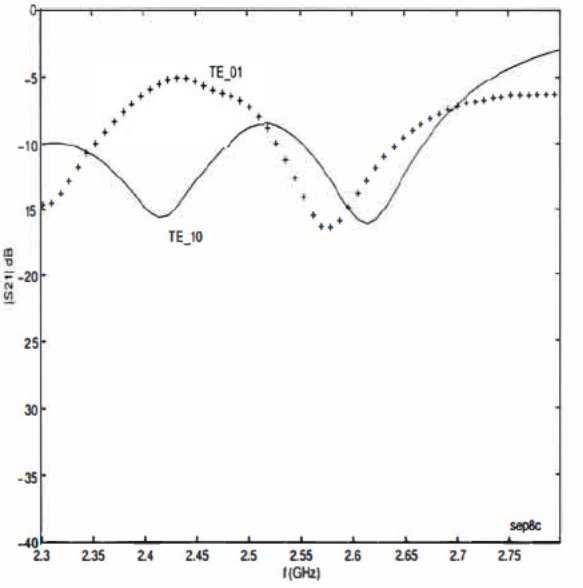

Figure 5.6: Transmission coefficient for the system of four 422 chiral steel unit cells in air.

mm between the centre legs of the hooks. The hooks remain unaltered. A front view diagram is shown in Figure 5.3.

5.5 Interpretation of the experiments

5.5.1 The chiral activity of the wire crystals

Chiral activity includes circular birefringence, circular dichroism, and rotatory dispersion. The most familiar of the chiral phenomena is the rotation of the plane of linearly polarized light by a chiral medium, a manifestation of circular birefringence. In the square waveguide, rotation of the plane of polarization of the TE_{10} mode is observed in the TE_{01} mode with the frequency of the electromagnetic wave below cutoff for higher order modes.

The wire crystals have been classified according to the point group symmetry of a unit cell of four hooks. This is the symmetry of the infinite crystal formed by translation of the unit cell. The symmetry of point group $4/m$ excludes chiral activity as a physical property. This is the symmetry of the unit cell of staples. The symmetry of point group $\bar{4}$ does not exclude chiral activity, except along the optic axis. The symmetry of point group 422 does not exclude chiral activity.

The TE_{01} mode was excited only in the transmitted wave (with a transmission coefficient stronger than 30 dB) in the experiments with the 422 chiral unit cell. In the experiment with the arrangement of four chiral unit cells in the square waveguide, it was excited only with the four unit cells of the same handedness. The magnitude of the transmission coefficient (for the TE_{10} and TE_{01} mode) is shown for the single 422 chiral unit cell of four steel hooks in the square waveguide in Figure 5.5 and for the system of four 422 chiral unit cells of steel hooks of the same handedness in Figure 5.6.

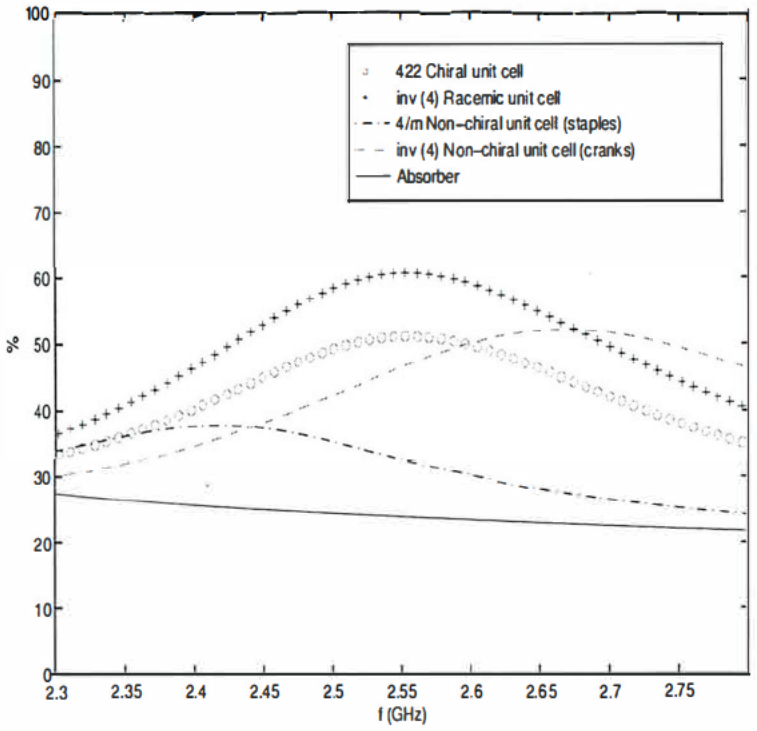

Figure 5.7: Absorption by the four uniaxial copper wire crystals embedded in a microwave absorber. A 422 chiral unit cell, a $4/m$ non-chiral unit cell of staples, $\bar{4}$ non-chiral unit cell of cranks, and a $\bar{4}$ racemic unit cell of enantiomorphous hooks.

5.5.2 Copper crystals embedded in a microwave absorber

Synthetic chiral microwave absorbers consist usually of a conventional microwave absorber which contain suitable macroscopic chiral objects. The inclusion of conducting wire structures in a microwave absorber serves to couple the incident field to the local ohmic and dielectric loss mechanisms of the host [11]. The four uniaxial crystals are compared for their absorption in Figure 5.7. The percentage power absorbed by a sample is,

$$P_{\text{absorbed}} = \left[1 - \left(|S_{11}|_y^2 + |S_{11}|_x^2 + |S_{21}|_y^2 + |S_{21}|_x^2\right)\right] \times 100\,\%,$$

with only the TE_{10} and TE_{01} modes propagating in the square waveguide. The microwave absorber (18 mm thick), without any wire inclusions, absorbs on average across the band about 25 % of the power. The absorption is enhanced by the inclusion of resonant wire structures in the microwave absorber. This is observed whether the inclusions are chiral, or non-chiral. There are differences regarding bandwidth and maximum absorption. This is to be expected for the orientation of the structures with respect to the incident field and with respect to each other will influence the induced currents in the hooks due to coupling. In the chiral and racemic unit cells of four hooks, currents are induced by the incident field in all the hooks. In the two non-chiral unit cells of staples and cranks, currents are directly induced by the incident field in two of the hooks, but in the other two hooks currents are induced by coupling. Even so, the unit cell of non-chiral cranks couples the incident field to the loss mechanisms of the host as effectively as the chiral and racemic unit cells.

The absorption by a system of four unit cells in the square waveguide is shown in Figure 5.8 for the chiral hooks and in Figure 5.9 for the staples. A system of four unit cells in the square

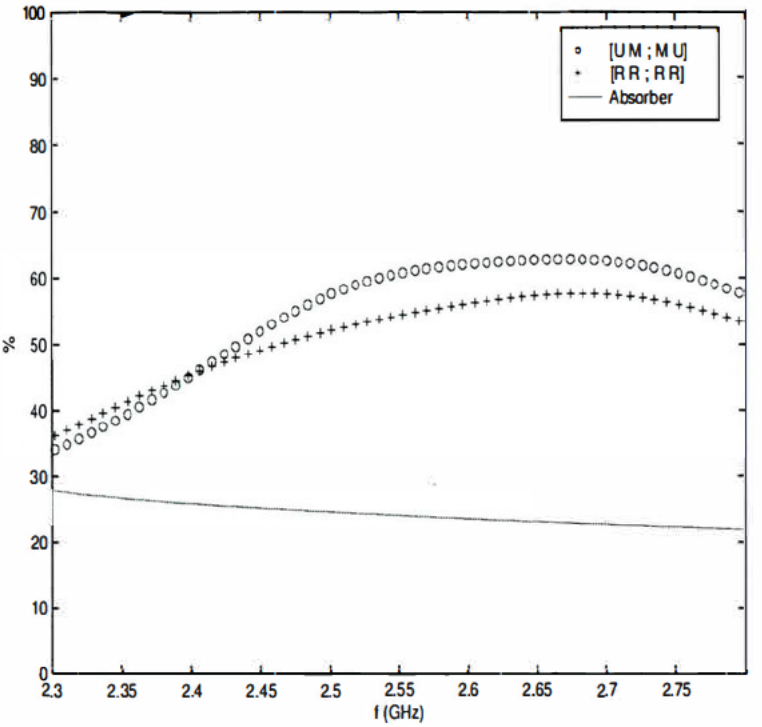

Figure 5.8: Absorption by the system of four copper wire chiral unit cells in the 72 mm square waveguide embedded in the microwave absorber. (+) Four 422 chiral unit cells of the same handedness. (o) Four 422 chiral unit cells, related by two orthogonal mirror planes.

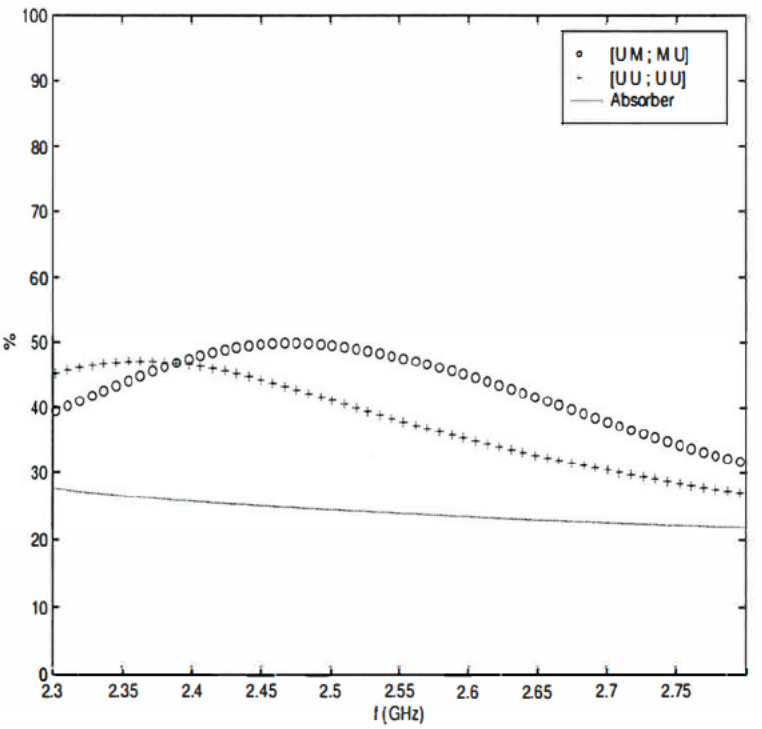

Figure 5.9: Absorption by the system of four copper wire non-chiral unit cells of staples in the 72 mm square waveguide embedded in the microwave absorber. (+) Four identical $4/m$ non-chiral unit cells. (o) Four $4/m$ non-chiral unit cells, related by two orthogonal mirror planes.

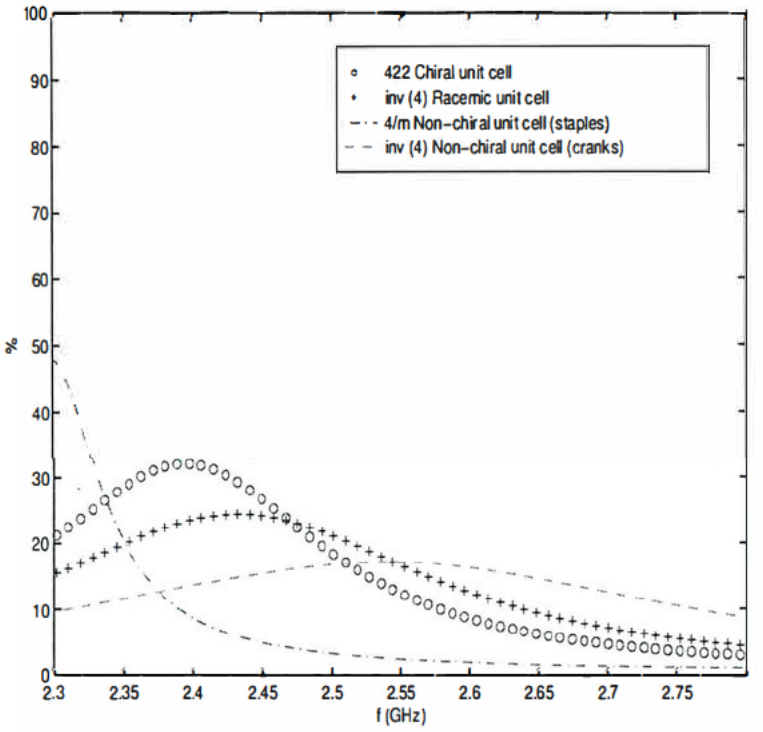

Figure 5.10: Absorption by the four uniaxial crystals of steel wire in air. A 422 chiral unit cell, a $4/m$ non-chiral unit cell of staples, a $\bar{4}$ non-chiral unit cell of cranks, and a $\bar{4}$ racemic unit cell of enantiomorphous hooks.

waveguide shows increased absorption and bandwidth compared to a single unit cell. The arrangement of four identical unit cells and of four mirrored unit cells differ with a few percent regarding the degree of absorption and bandwidth, for both the chiral hook and the non-chiral staple systems.

From these experiments and observations, what are the conclusions? The inclusion of wire structures in a microwave absorber can increase the absorption interaction of the field with the material, provided that the inclusions are good conductors and of resonant length. Geometry is certainly important, and in various ways. The comparison in Figure 5.7 between the two non-chiral unit cells, one of staples, the other of cranks, clearly shows that the geometry of the inclusion plays a significant role. Both unit cells are non-chiral, both have two hooks with legs oriented parallel to the polarization of the electric field, and two hooks orthogonal to the incident electric field polarization, yet their interaction with the field is substantially different. The experiment with four unit cells in the square waveguide indicates that the interaction between the unit cells is important and dependent on spacing and geometrical repetition.

5.5.3 Steel crystals in air

The absorption by resonant steel wire hooks in polystyrene foam was significant in the experiments in rectangular waveguide. The absorption is due to ohmic loss in the wires. The four uniaxial crystals of steel wire are compared for their absorption in Figure 5.10. Their performance regarding absorption is greatly varied. On the one hand the non-chiral unit cell of staples absorbs a maximum of approximately 47 % of the power, with a half power bandwidth of the order 3 %, on the other hand the non-chiral unit cell of cranks shows a broadband response,

with a half power bandwidth of 20 % and an absorption maximum of 17 %. In between lies the performance of the chiral and racemic unit cells.

The absorption by a system of four unit cells in the square waveguide is shown in Figure 5.11 for the chiral hooks and in Figure 5.12 for the staples.

The closer spacing of the unit cells in these experiments has a dramatic effect on the absorption. The closely spaced unit cells of resonant steel hooks in air are rather efficient in absorption. Two absorption peaks appear in the frequency band of the experiment and the absorption is significant over a broader band. This is reminiscent of the effect observed in a coupled pendulum system of two identical pendulums connected by a spring [17, vol. I, §48-7 and §49-4], and in a synchronously tuned coupled resonator filter [46, pp. 296–305].

Finally, the results of the parametric study of the absorption as a function of the spacing between the hooks in a unit cell, are presented in Figure 5.13 for the 422 chiral unit cell and in Figure 5.14 for the $4/m$ non-chiral unit cell. The unit cells were analysed for a spacing of 24 mm, 40 mm, and 56 mm between the centre legs of the hooks. The response is completely different for the two systems of hooks and staples. For the unit cell of chiral hooks, increased spacing between the hooks in the unit cell results in increased absorption and narrower bandwidth, with not much variation in the frequency of maximum absorption. For the unit cell of staples, increased spacing between the hooks in the unit cell results in decreased absorption with little change in bandwidth. Why these opposite tendencies in the response occur is not clearly understood. By increasing the spacing between the hooks, the hooks are moved into a region of weaker illumination in the square waveguide, but the conditions are the same for the chiral hooks in the 422 arrangement and the non-chiral staples in the $4/m$ arrangement. It has been noted before that in the unit cell of staples, two of the elements are orthogonal to the incident field polarization. By moving the elements further apart, the interaction of these two elements with the directly excited elements is weakened and the induced currents are orders of magnitude smaller in these two elements. In the chiral unit cell, currents are directly induced by the incident field in all four hooks. From the viewpoint of the infinitely imaged crystal illuminated at oblique incidence, with θ varying between 65° and 48° in the frequency range 2.3 to 2.8 GHz, changing the spacing between the elements within the unit cell of four hooks, simultaneously changes the spacing between the unit cell and its image. Although the wire crystals are of simple geometry, no simple picture emerges of the interaction of an electromagnetic wave with finitely conducting resonant wire structures in a lossless environment, and its dissipation due to ohmic loss in the wires.

5.6 Conclusion

The FDTD code provided a reliable tool for closely studying the behaviour of resonant wire inclusions in a host. The numerical experiments performed in square waveguide on the chiral, non-chiral, and racemic crystals were described and discussed in the context of the waveguide environment. The observations and conclusions from this work are discussed in the next chapter.

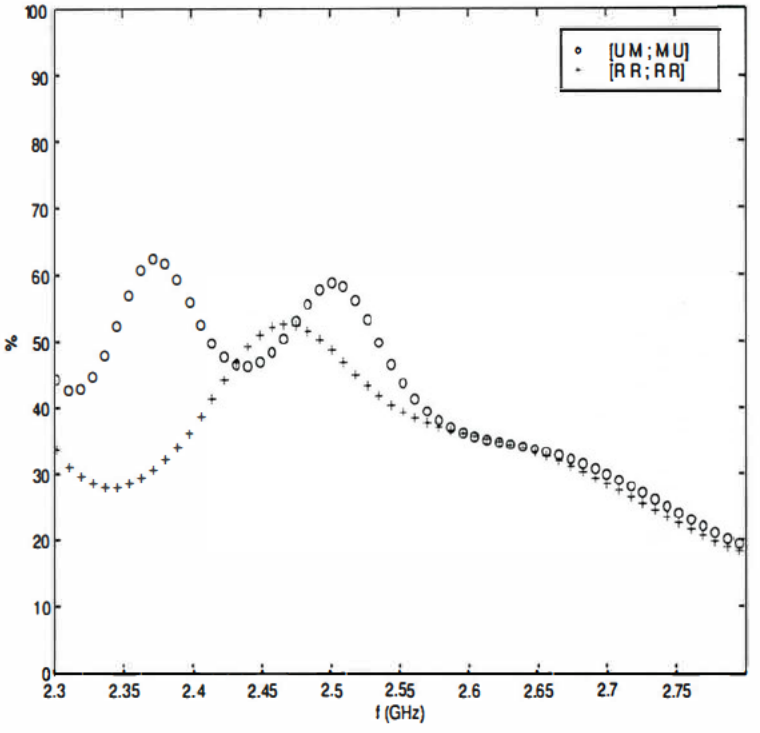

Figure 5.11: Absorption by the system of four chiral unit cells of steel hooks in air in the 72 mm square waveguide. (+) Four 422 chiral unit cells of the same handedness. (o) Four 422 chiral unit cells, related by two orthogonal mirror planes.

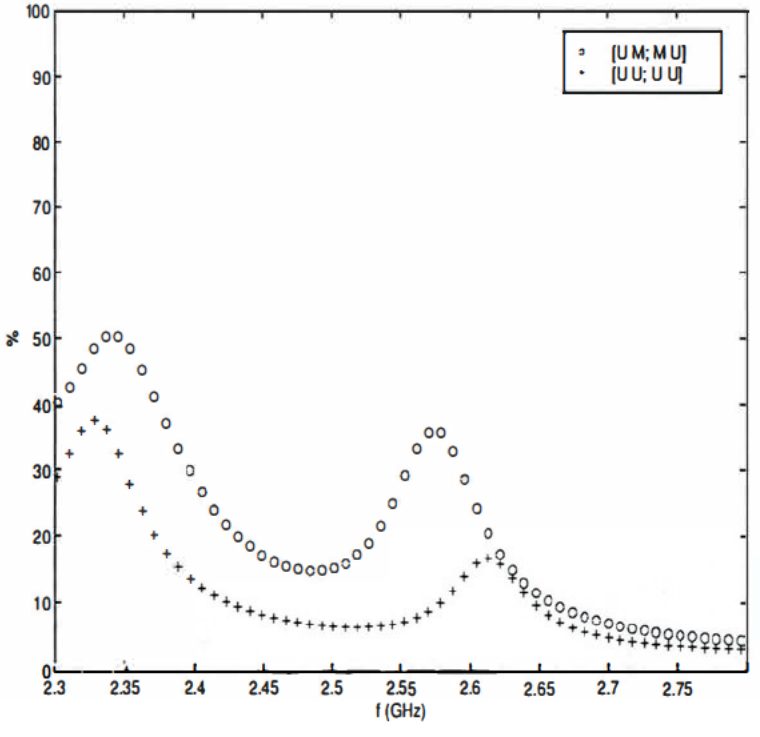

Figure 5.12: Absorption by the system of four non-chiral unit cells of steel staples in air in the 72 mm square waveguide. (+) Four $4/m$ non-chiral unit cells. (o) Four $4/m$ non-chiral unit cells, related by two orthogonal mirror planes.

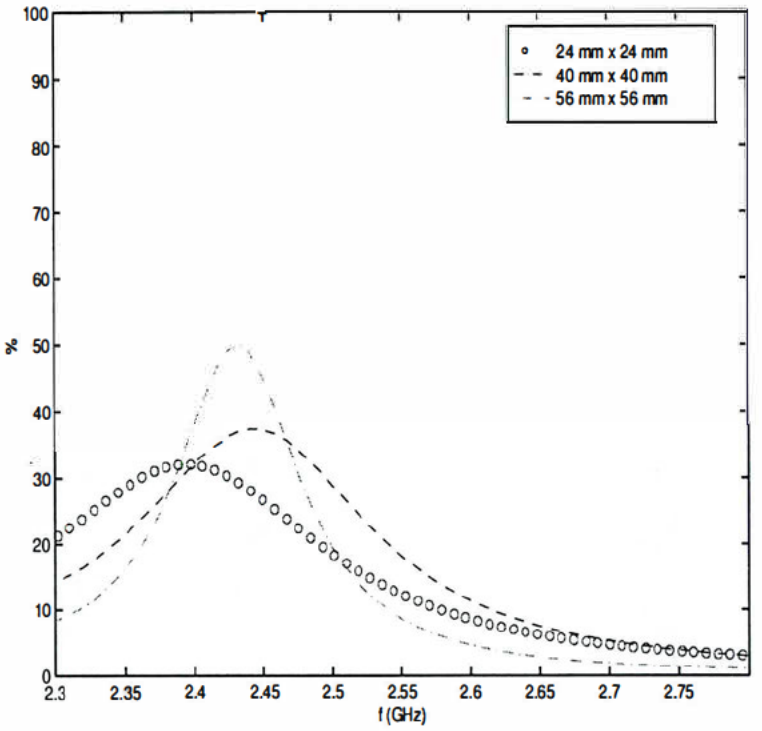

Figure 5.13: Absorption by 422 chiral unit cells of steel wire in air. Spacings of 24 mm (o), 40 mm (−−) and 56 mm (−·) between the centre legs in each unit cell.

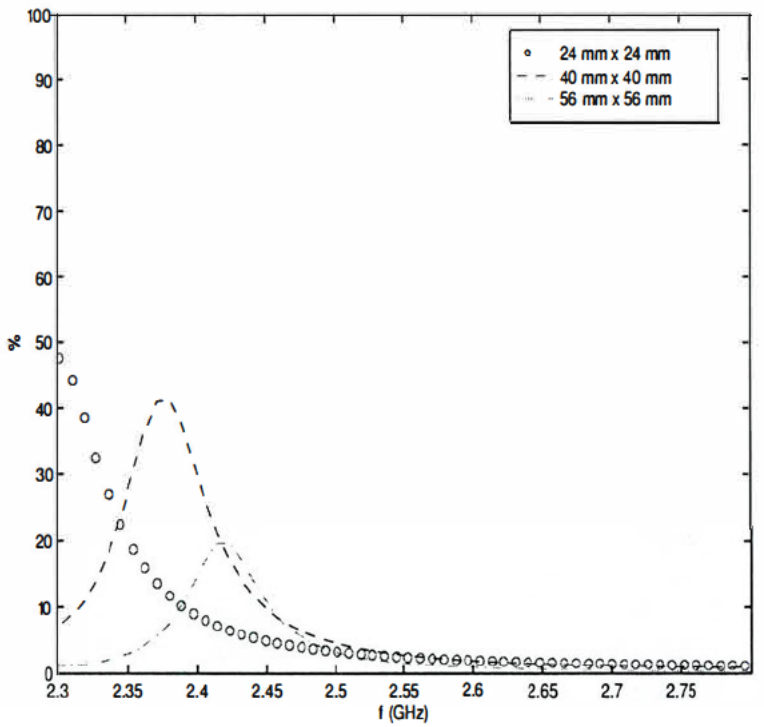

Figure 5.14: Absorption by $4/m$ non-chiral unit cells of steel wire in air. Spacings of 24 mm (o), 40 mm (−) and 56 mm (−·) between the centre legs in each unit cell.

Chapter 6

Conclusions

A theoretical and experimental study was conducted in search of a physical understanding of the role of chirality in synthetic microwave absorbers. The approach was to closely study the interaction of an electromagnetic wave with a microwave absorbing host containing resonant wire inclusions. The wire inclusions and their arrangement in the host are closely related in geometry.

The unit cells of synthetic material were designed to fit into a rectangular or square waveguide to allow accurate measurements of reflection and transmission coefficients. The three segment hook was chosen as the basic element, and chiral and non-chiral geometries of the hook were arranged to form uniaxial wire crystals. Four uniaxial crystals were described and classified according to their point group symmetry in order to provide a well-defined basis for the comparative study: a chiral unit cell, consisting of four hooks of the same handedness; a non-chiral unit cell of four staples; a non-chiral unit cell of four cranks; and a racemic unit cell of enantiomorphous chiral hooks, two of each handedness.

A finite difference time domain code was developed for the full-wave numerical analysis in rectangular or square waveguide of the chiral and non-chiral conducting thin wire structures, embedded in an absorbing host. The code uses a subcell thin wire formulation for conducting wires, including the effective material properties of the wires. The code was validated by comparing numerical and measured experiments in a rectangular waveguide. The FDTD subcell thin wire formulation for highly conducting wires was found to predict the scattering with respect to magnitude, phase and absorption, with good accuracy. The FDTD code could therefore be used to closely study the behaviour of resonant wire inclusions in a host.

Chiral phenomena at microwave frequencies are observed in synthetic composites which contain macroscopic conducting chiral inclusions. The experiments were therefore aimed at studying the absorption mechanisms in such materials. More specifically, copper wire hooks, embedded in a microwave absorber which could be characterised by the two constant parameters ϵ_r and σ in the frequency range of interest, were studied. The material parameters of the microwave absorber were determined from measured scattering parameters through a model-based parameter estimation technique. It was found experimentally that the properties of the wire are not of much importance in the performance of the microwave absorber, except that the wire should be a good conductor. The numerical experiments in a microwave absorber were therefore only performed for copper wire hooks.

The absorption by resonant steel wire hooks in essentially transparent polystyrene foam was found experimentally to be significant. This lead to the incorporation of a high frequency surface impedance model for round conductors. Good agreement was obtained with this formulation between measurement and the FDTD prediction for copper wire. It was surprising to find that the relative permeability of steel at microwave frequencies may be significantly different from

unity, and frequency dependent. The DC conductivity of the guitar steel string was measured to be 4.7×10^6 S/m. A good fit of the FDTD predictions to the measured scattering parameters suggests an effective conductivity of the order 2×10^5 S/m for the guitar steel string, or on average $|\mu_r| \approx 23$ across the frequency band, which is quite possible according to measurements by Sanderson [44, p. 42]. The uniaxial crystals of resonant steel hooks in air were consequently also studied for their absorption.

The wire crystals were viewed in a *square* waveguide and illuminated with the TE_{10} mode, a plane wave of non-uniform amplitude distribution. In order to maintain the 4-fold symmetry in the waveguide experiment, the crystals were centered in the square waveguide. The crystals were studied in a frequency band where only the TE_{10} and TE_{01} modes can propagate. In the experiments, the reflected and transmitted waves were measured for both modes. The TE_{01} mode was only excited in the transmitted wave in the experiments with the 422 chiral unit cell. An alternative perspective to the experiments in waveguide is to view the unit cell in the waveguide as an infinite array of imaged unit cells, illuminated at oblique incidence. Higher order modes in the waveguide correspond to grating lobes for the infinite array.

Looking at the crystals through waveguide provides a specific perspective, and not necessarily the most general, or widest perspective from an application point of view. The properties of crystals are dependent on the direction from which they are illuminated. For example, if an optically uniaxial crystal is only studied for propagation along the optic axis, double refraction (linear birefringence) will not be observed, and in crystals of a certain point group symmetry (e.g. $\bar{4}$ and $\bar{4}2m$) optical activity cannot occur along the optic axis. However, in order to study absorption mechanisms in the composite materials, the waveguide provides a well-defined and controlled environment for accurate measurement of reflection and transmission coefficients. It was decided to work in waveguide to study the absorption properties, and not, e.g. to use the 11–17 GHz quasi-Gaussian beam free space measurement system [31] because of out of beam scattering and diffraction around resonance. In the waveguide the scattering coefficients for unit cells of the synthetic material are determined accurately, and energy balance is used to determine the absorption by the synthetic material.

The uniaxial crystals of resonant steel hooks in air showed widely varied absorption response for the chiral, racemic and non-chiral systems, dependent on the distance between the elements in a unit cell, the distance between adjacent unit cells, and the repetition of the unit cells. It is observed that resonant hooks of steel wire can be arranged to dissipate an incident electromagnetic wave significantly.

The conventional approach towards studying microwave chiral materials is through an effective medium constitutive parameter description. An experimental study by Cloete *et al.* [11] was performed on chiral and racemic absorbing, composite materials consisting of small, conducting helices, randomly oriented. They calculate the effective medium constitutive parameters from measured scattering parameters and use the normal incidence reflection coefficient of each material in the Dällenbach configuration as a simple measure of their relative merits as microwave absorbers. Conclusions from their study are that "tiny copper helices can somewhat enhance the performance of dielectric absorbers about the frequency where the helices are one half-wavelength resonant," and that "a chiral composite and its racemic counterpart have essentially identical properties as absorbers of specular reflection." Like Bohren *et al.* [10] they conjecture "that the chirality of the helix does not play an essential role in absorbers." They remark that the advantage of the helix geometry is that it makes a conveniently compact resonator.

The approach in this study towards addressing the claims about chirality in microwave absorbers and towards finding an answer to Bohren's question is original in various aspects: in the choice of the three segment hook as the chiral element, instead of the helix, for the

closely related geometry of its enantiomorph and the non-chiral hooks; in the study of a unit cell of resonant (in the microwave regime) chiral and non-chiral hooks; and in the full-wave numerical analysis of the resonant wire hooks, embedded in a host, instead of an effective medium constitutive parameter description.

In the experiments with the uniaxial unit cells, embedded in a dielectric microwave absorber, the following observations were made.

Geometry is important, and in various ways. The inclusion of wire structures in a microwave absorber can improve the absorption interaction of an electromagnetic wave with the host, provided that the inclusions are good conductors and of resonant length. This is observed whether the inclusions are chiral, or non-chiral. In the comparison of the performance of the four uniaxial crystals in the square waveguide, there are differences in the amount of absorption and bandwidth, indicating that geometry and geometrical arrangement in the absorbing host is significant. The important observation is that the unit cell of non-chiral cranks couples the incident field to the loss mechanisms of the host as effectively as the unit cell of chiral hooks and the racemic unit cell of enantiomorphous hooks. The experiment with four unit cells in the square waveguide indicated that the interaction between the unit cells is important and dependent on spacing and geometrical repetition.

Chirality is a geometrical requirement for optical activity. However, no evidence is found in these experiments to suggest that chirality is a geometrical requirement for absorption by synthetic microwave materials.

Appendix A

Experiments in rectangular waveguide

A.1 The microwave absorber

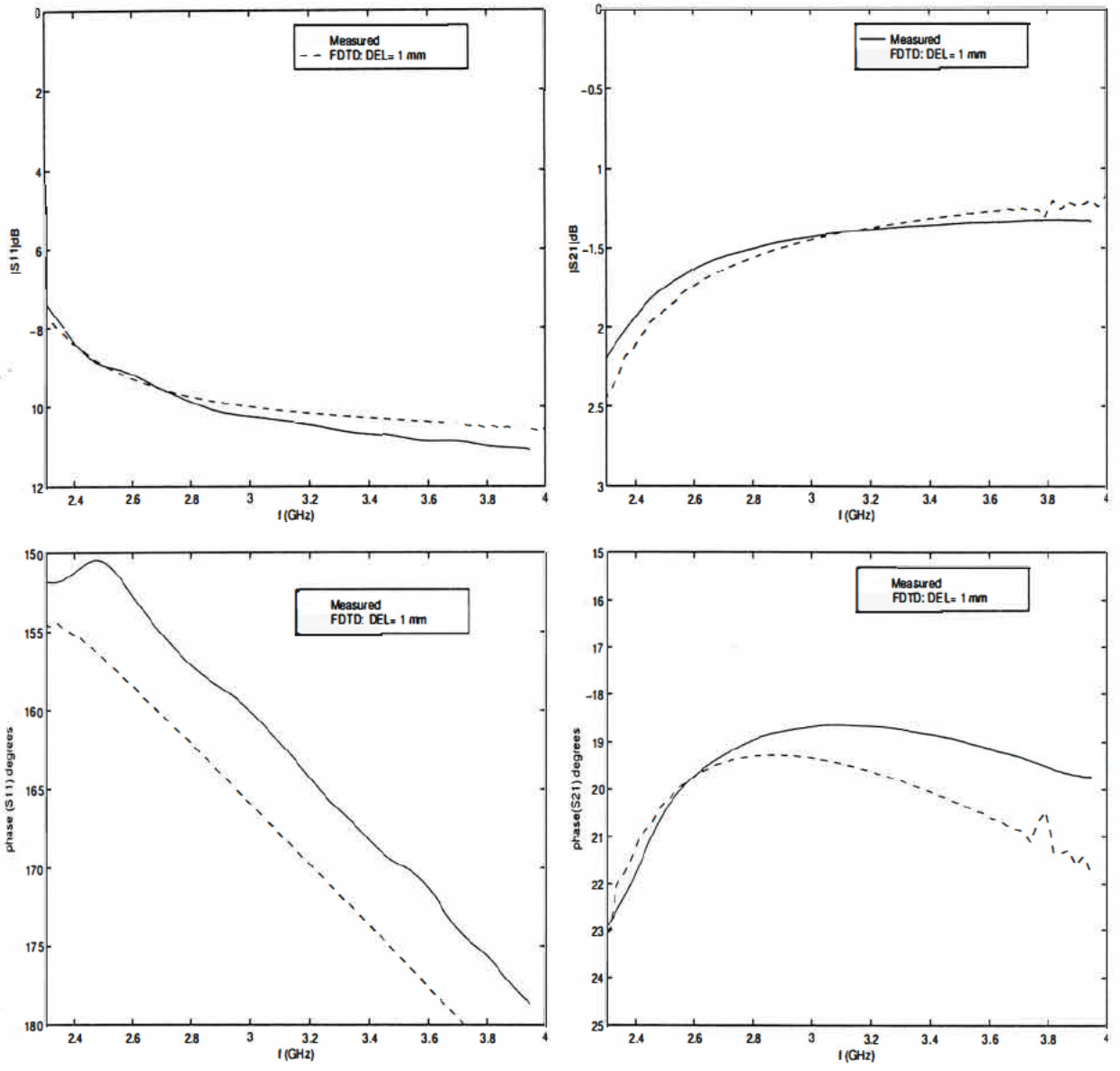

Figure A.1: Measured scattering parameters of the absorber (thickness $d \approx 13.85$ mm) compared to the FDTD experiment with $\epsilon_r = 1.67$ and $\sigma = 0.04$ S/m and an effective thickness of $d = 14$ mm ($\Delta = 1$ mm).

A.2 Point group 422 chiral crystal

Point group 422 copper unit cell embedded in a microwave absorber

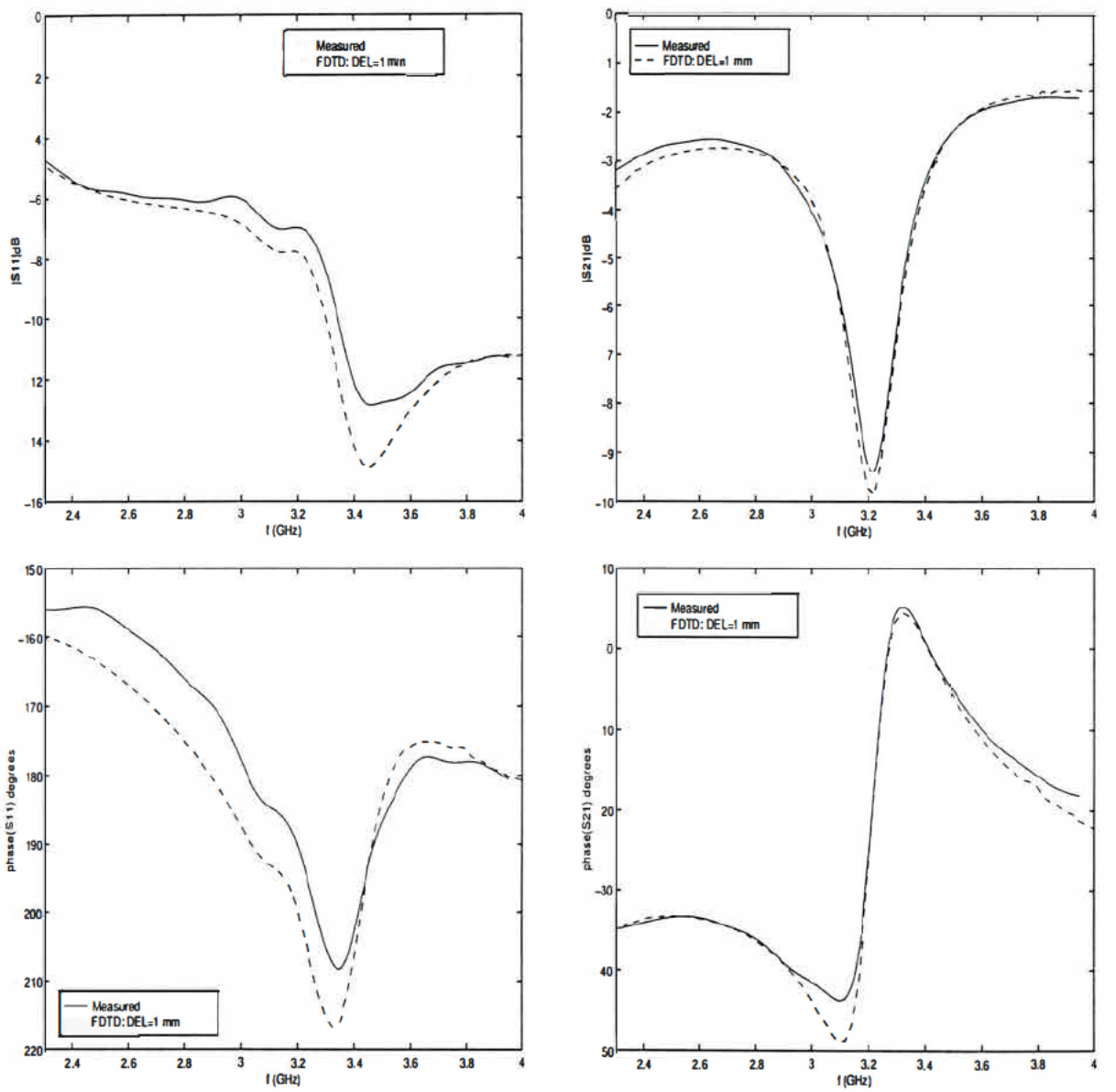

Figure A.2: Point group 422 chiral unit cell in absorber, copper wire. Measured scattering parameters compared to the FDTD experiment, with $\sigma_{\text{wire}} = 5.7 \times 10^7$ S/m, and $\epsilon_r = 1.67$ and $\sigma = 0.04$ S/m for the absorbing host.

Point group 422 steel unit cell embedded in a microwave absorber

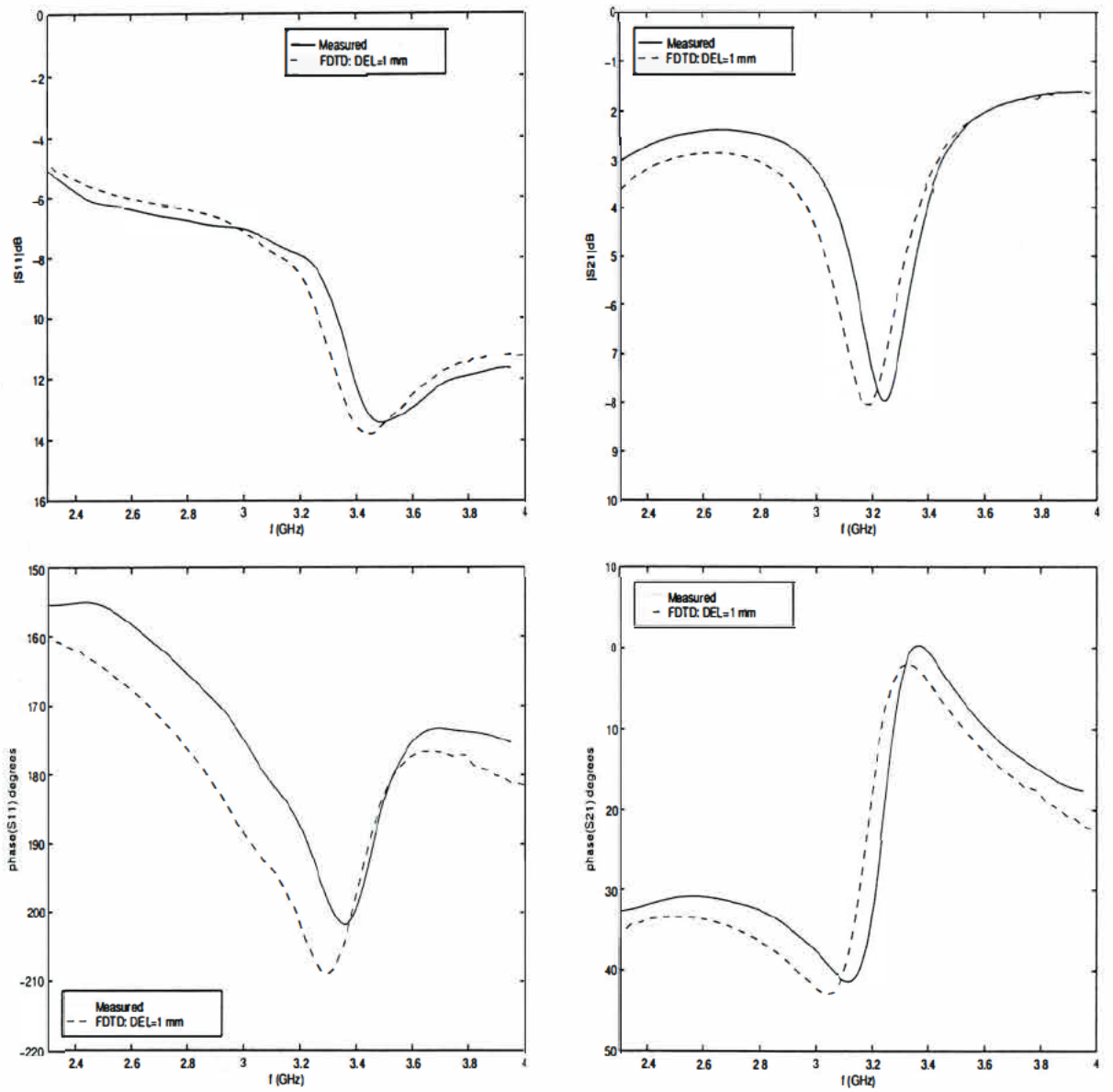

Figure A.3: Point group 422 chiral unit cell in absorber, steel wire. Measured scattering parameters compared to the FDTD experiment, with $\sigma_{\mathbf{wire}} = 2 \times 10^5$ S/m, and $\epsilon_r = 1.67$ and $\sigma = 0.04$ S/m for the absorbing host.

A.3 Point group $4/m$ non-chiral crystal

Point group $4/m$ copper unit cell embedded in a microwave absorber

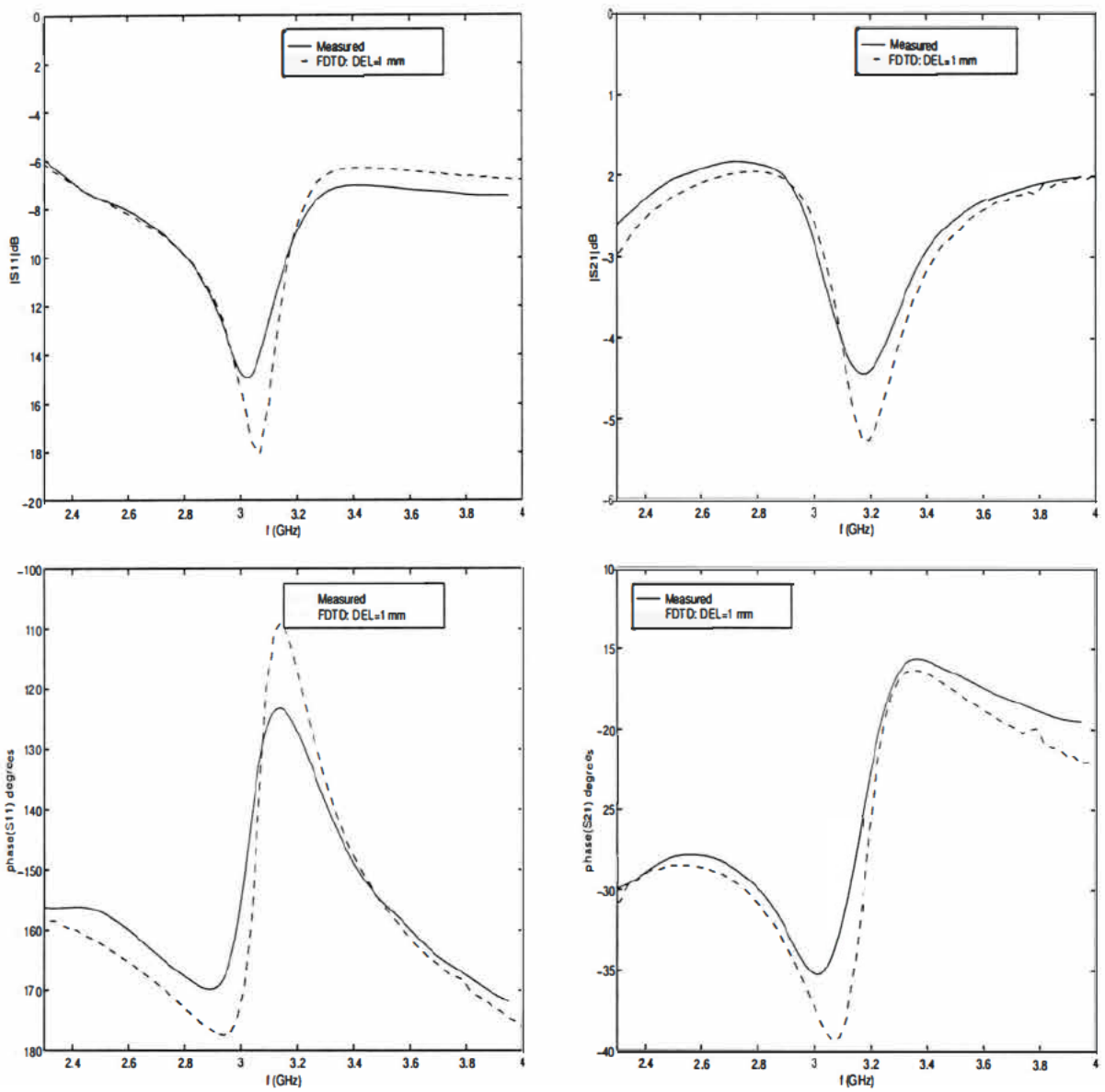

Figure A.4: Point group $4/m$ non-chiral unit cell in absorber, copper wire. Measured scattering parameters compared to the FDTD experiment, with $\sigma_{\text{wire}} = 5.7 \times 10^7$ S/m, and $\epsilon_r = 1.67$ and $\sigma = 0.04$ S/m for the absorbing host.

Point group $4/m$ steel unit cell embedded in a microwave absorber

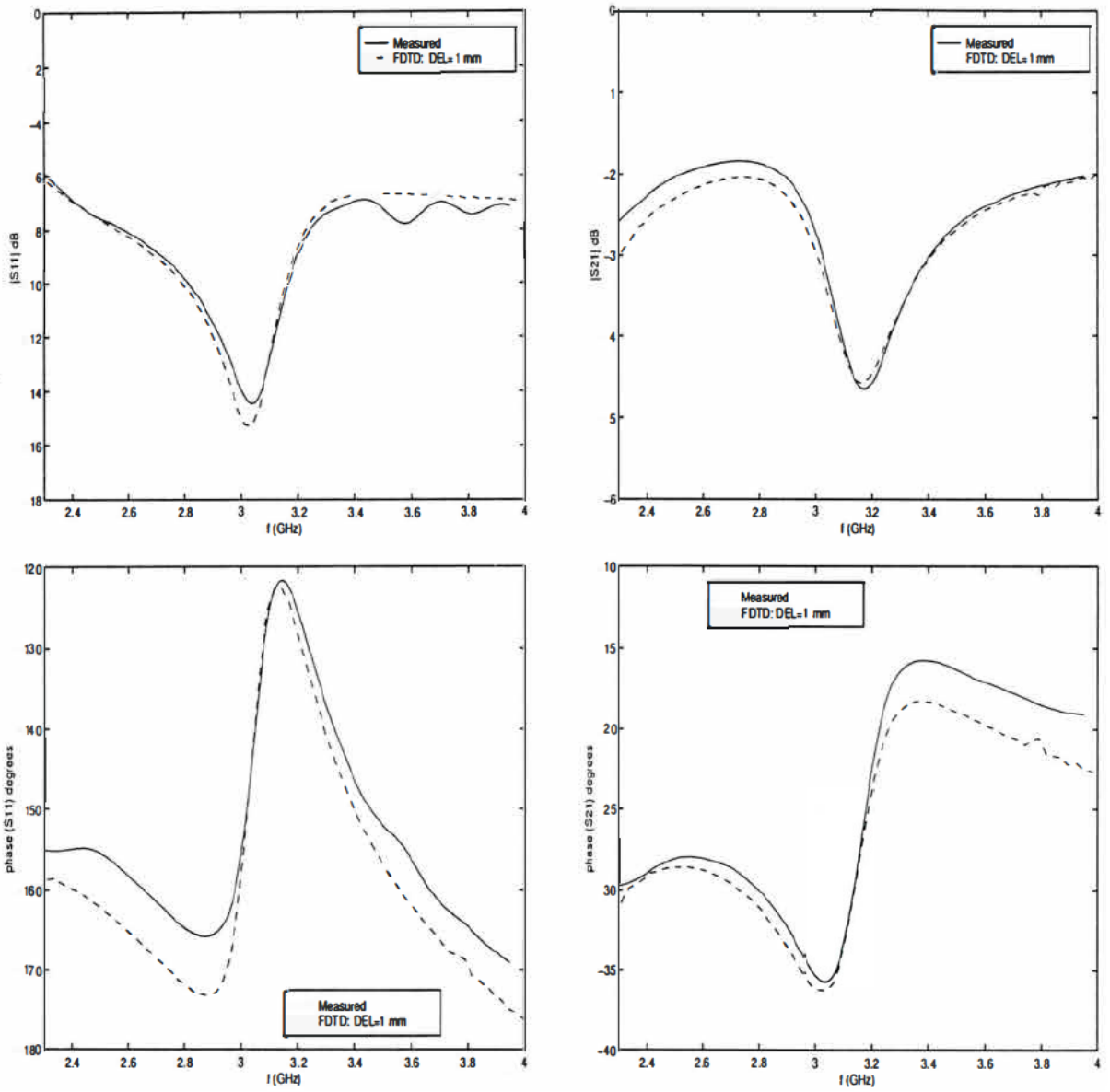

Figure A.5: Point group $4/m$ non-chiral unit cell in absorber, steel wire. Measured scattering parameters compared to the FDTD experiment, with $\sigma_{\text{wire}} = 2 \times 10^5$ S/m, and $\epsilon_r = 1.67$ and $\sigma = 0.04$ S/m for the absorbing host.

Appendix B

Point group 2 racemic crystal

Measured and predicted results for the racemic unit cell of point group 2 symmetry, consisting of four thin wire hooks of alternating handedness, in rectangular waveguide, are presented in this appendix. The results are not discussed in detail, but are presented in confirmation of the substantiation of the code. The detail of the geometry, measurements and numerical experiments were discussed in Chapter 4.

Racemic unit cell of point group 2 symmetry.

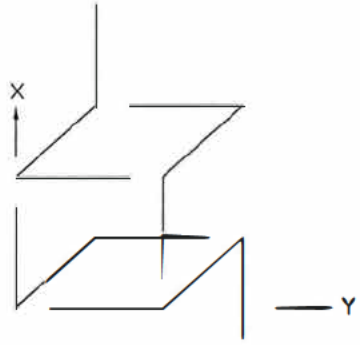

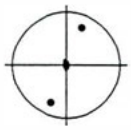

(1st setting)

2

Point group 2 has one 2-fold axis.
The unit cell consists of four chiral hooks, two of each enantiomorph.
Point group 2 falls in the monoclinic crystal system and is optically biaxial.

Copper unit cell in polystyrene foam

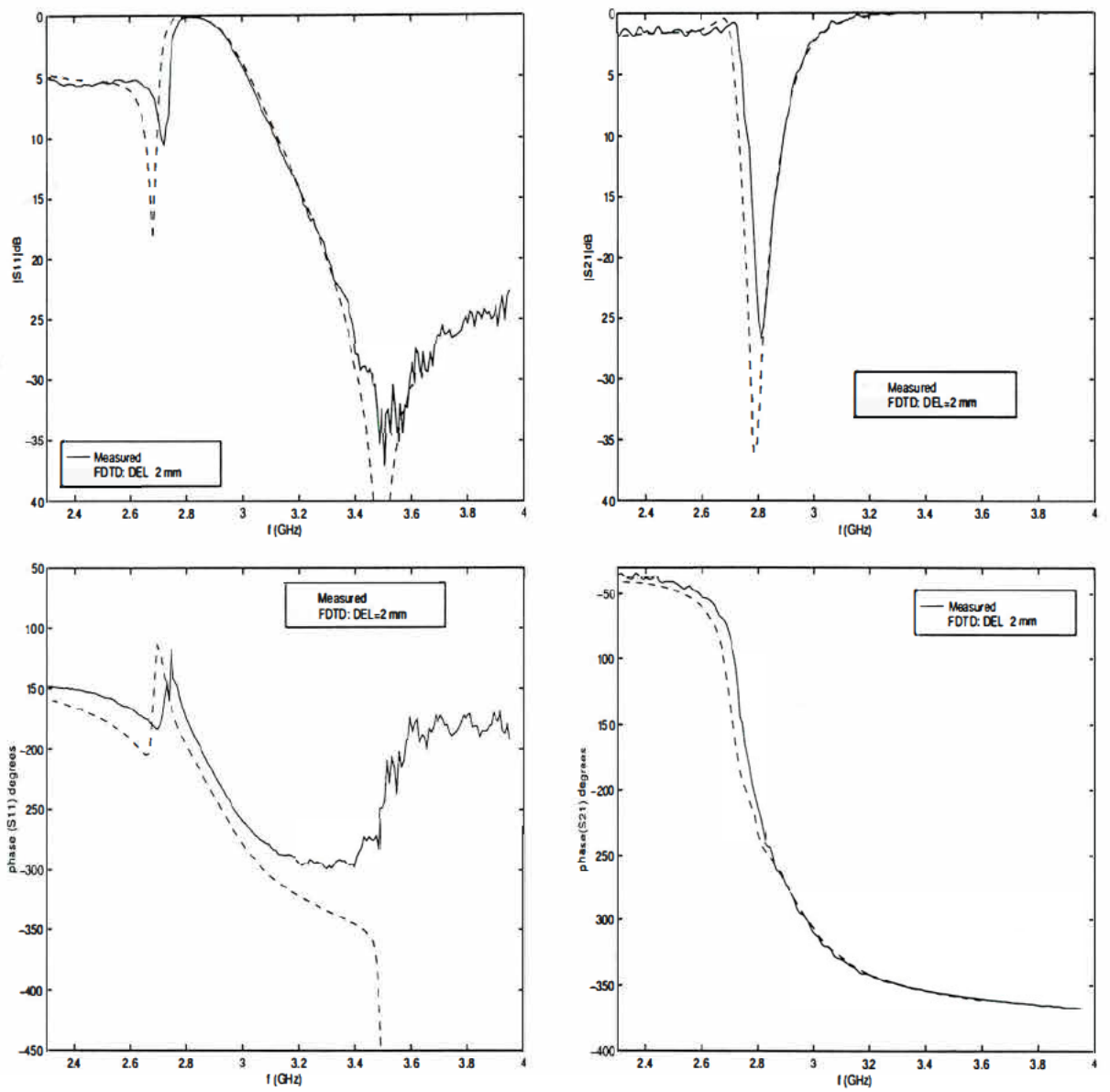

Figure B.1: Point group 2 unit cell in polystyrene foam, copper wire. Measured scattering parameters compared to the FDTD experiment, with $\sigma_{\text{wire}} = 5.7 \times 10^7$ S/m, and $\Delta = 2$ mm.

Steel unit cell in polystyrene foam

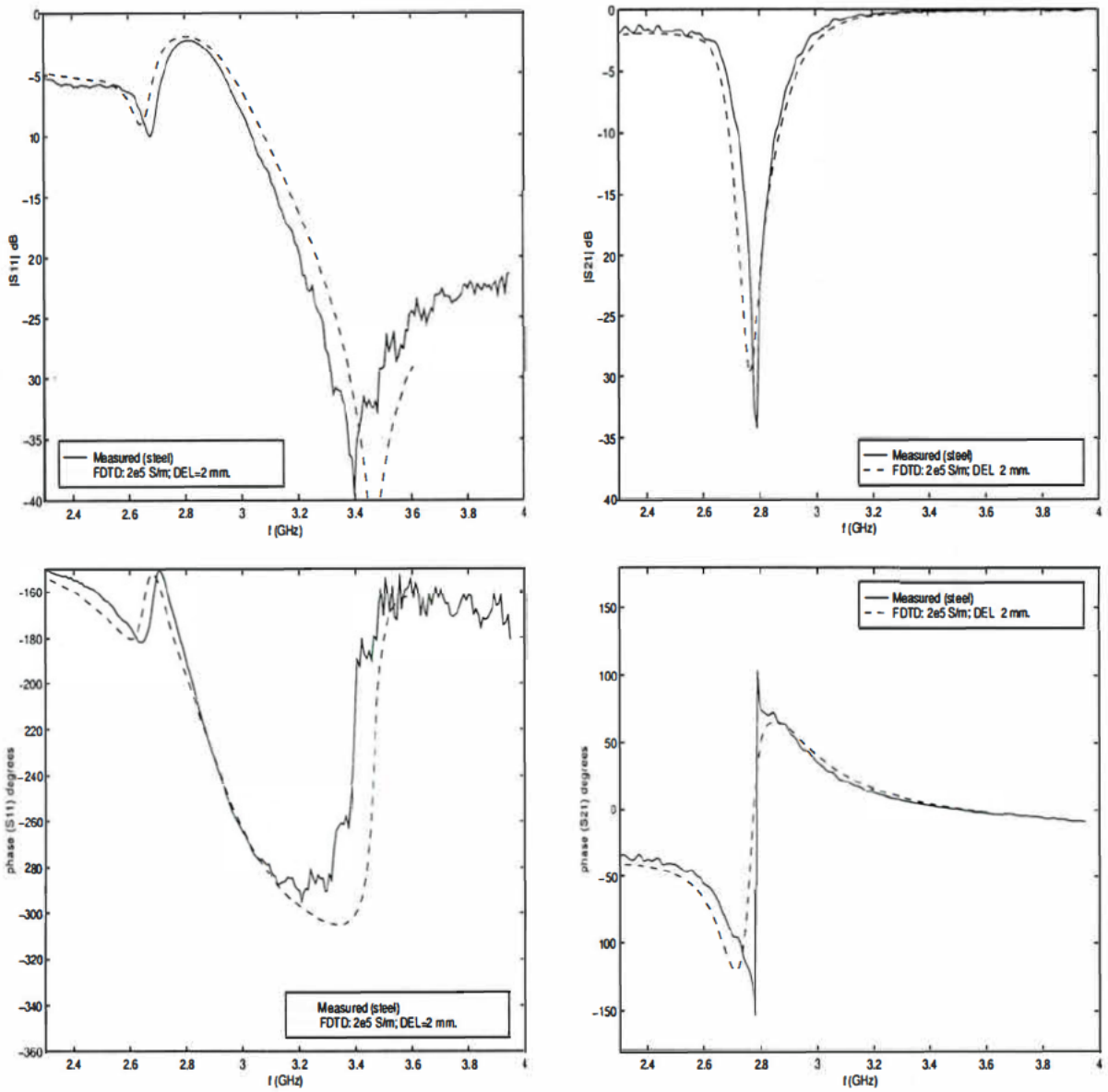

Figure B.2: Point group 2 unit cell in polystyrene foam, steel wire. Measured scattering parameters compared to the FDTD experiment, with $\sigma_{\text{wire}} = 2 \times 10^5$ S/m and $\Delta = 2$ mm.

Copper unit cell embedded in a microwave absorber

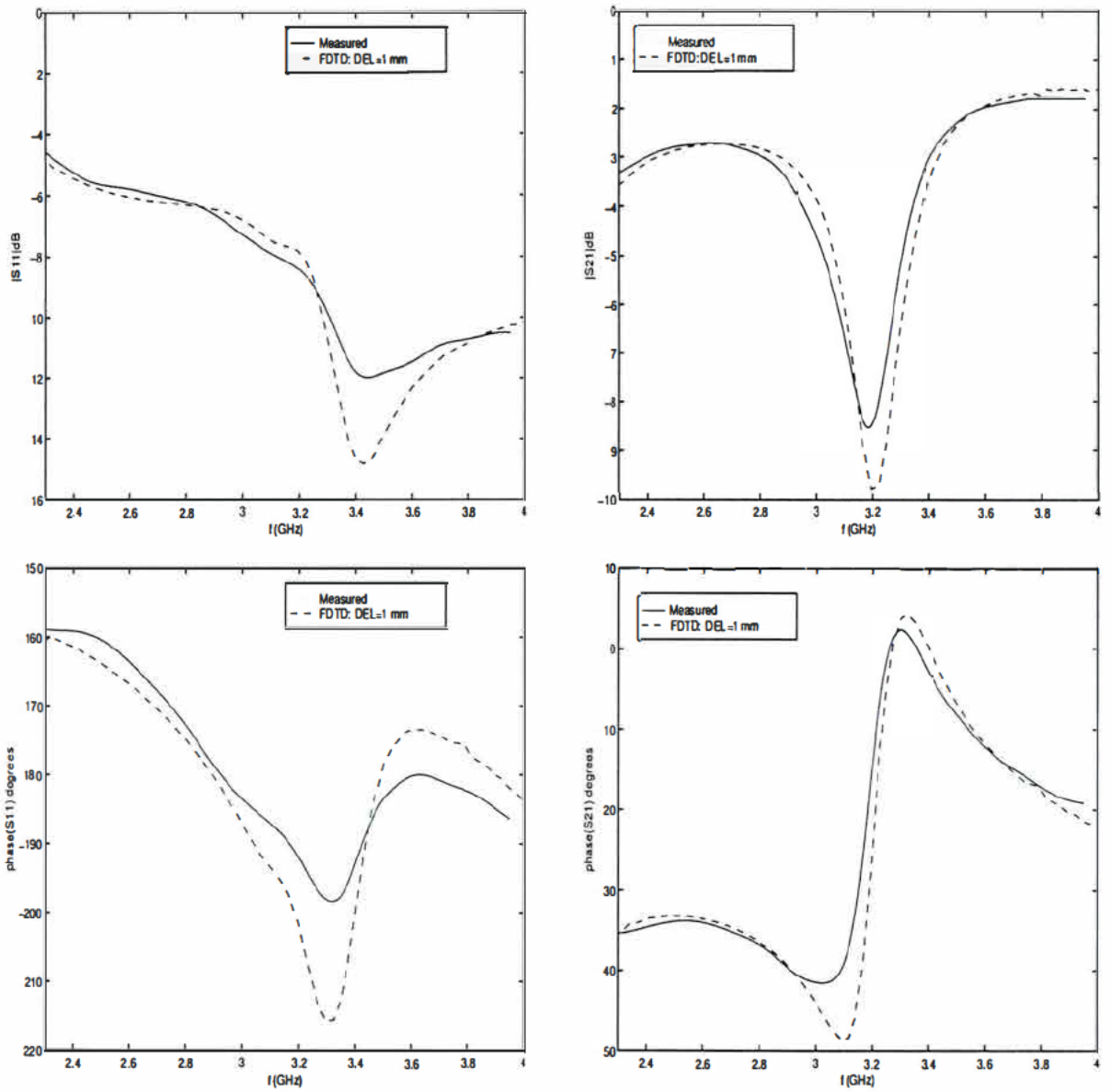

Figure B.3: Point group 2 unit cell in absorber, copper wire. Measured scattering parameters compared to the FDTD experiment, with $\sigma_{\text{wire}} = 5.7 \times 10^7$ S/m, and $\epsilon_r = 1.67$ and $\sigma = 0.04$ S/m for the absorbing host, and $\Delta = 1$ mm.

Steel unit cell embedded in a microwave absorber

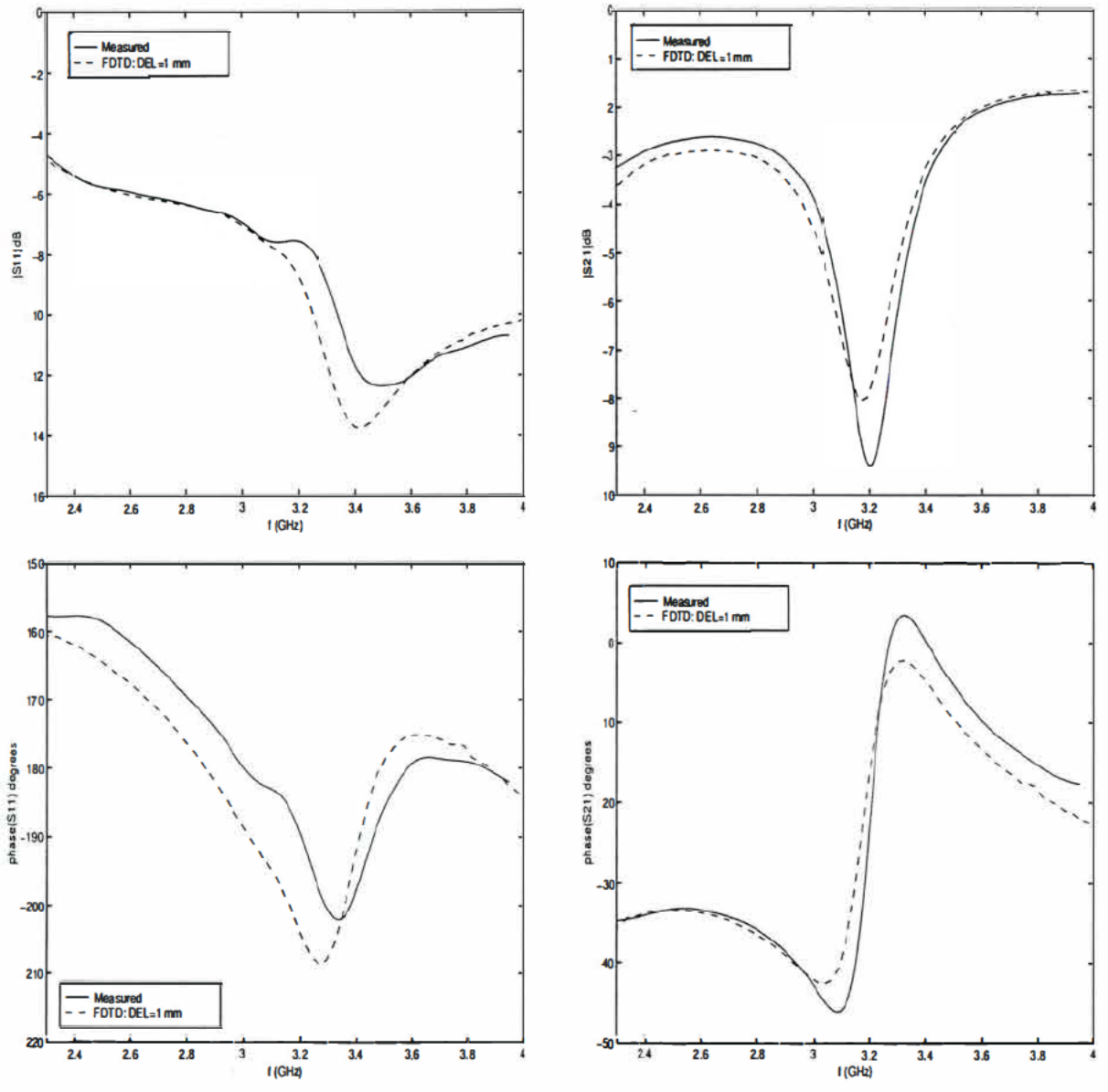

Figure B.4: Point group 2 unit cell in absorber, steel wire. Measured scattering parameters compared to the FDTD experiment, with $\sigma_{\text{wire}} = 2 \times 10^5$ S/m, and $\epsilon_r = 1.67$ and $\sigma = 0.04$ S/m for the absorbing host.

Appendix C

Experiments in a square waveguide

C.1 A single unit cell in a square waveguide

Copper unit cell embedded in a microwave absorber

Reflection and transmission coefficient in a 72 mm square waveguide for a unit cell of four copper hooks embedded in a microwave absorber. Total hook length $L = 48$ mm; distance between centre legs, 24 mm; $\sigma_{\text{wire}} = 5.7 \times 10^7$ S/m; microwave absorbing host, $\epsilon_r = 1.67$ and $\sigma = 0.04$ S/m, thickness 18 mm.

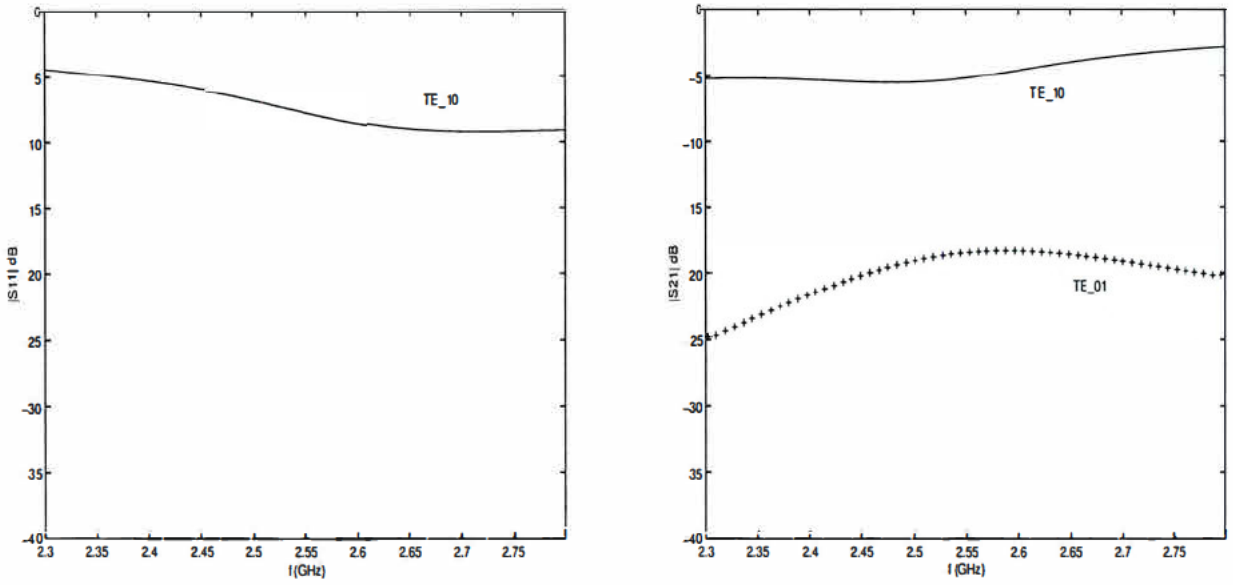

Figure C.1: Point group 422 chiral unit cell.

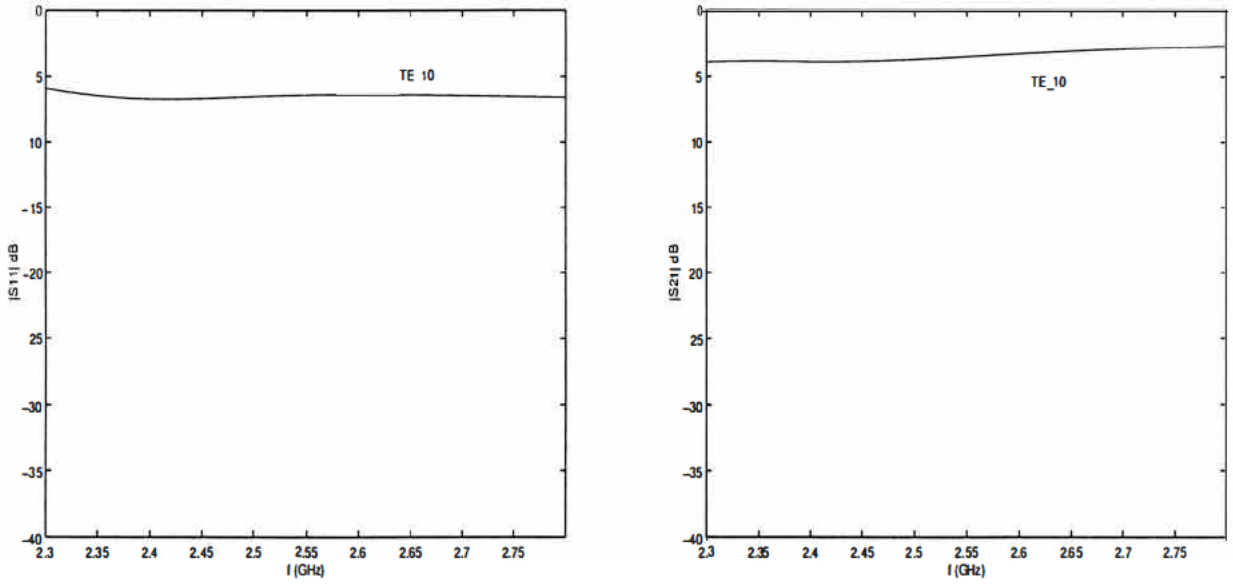

Figure C.2: Point group $4/m$ non-chiral unit cell of staples.

Copper unit cell embedded in a microwave absorber

Reflection and transmission coefficient in a 72 mm square waveguide for a unit cell of four copper hooks embedded in a microwave absorber. Total hook length $L = 48$ mm; distance between centre legs, 24 mm; $\sigma_{\text{wire}} = 5.7 \times 10^7$ S/m; microwave absorbing host, $\epsilon_r = 1.67$ and $\sigma = 0.04$ S/m, thickness 18 mm.

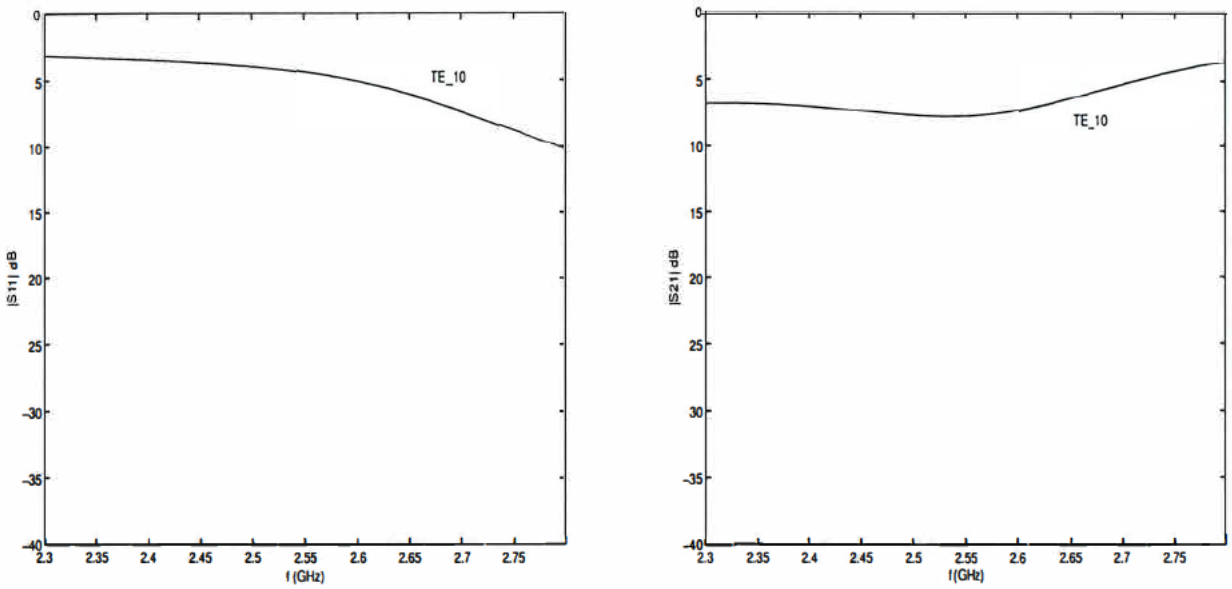

Figure C.3: Point group $\bar{4}$ non-chiral unit cell of cranks.

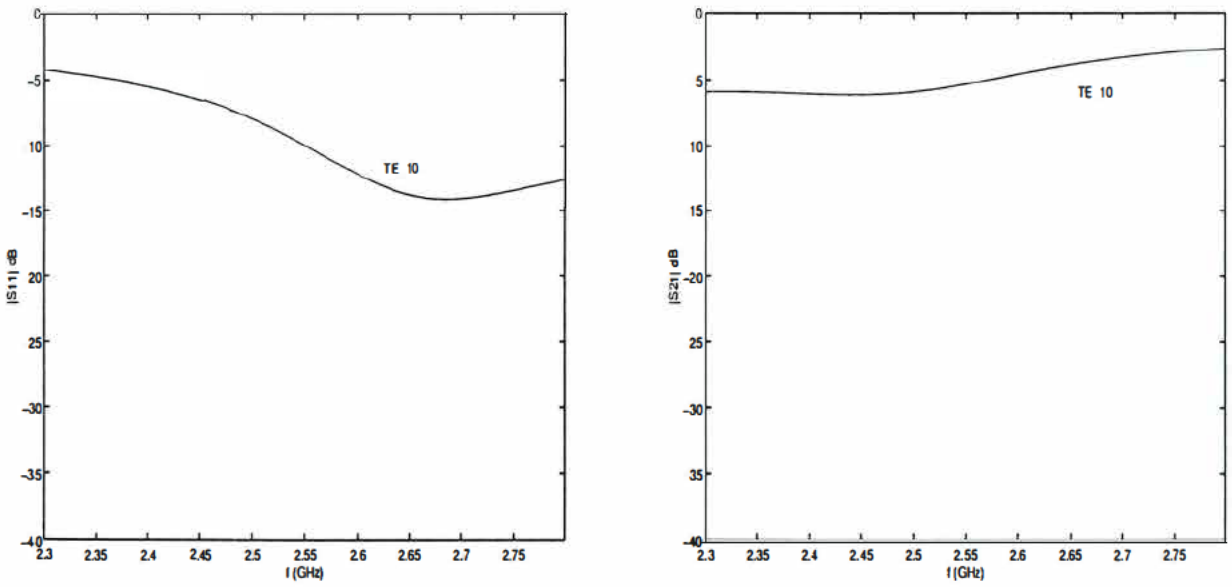

Figure C.4: Point group $\bar{4}$ racemic unit cell of enantiomorphous hooks.

Steel unit cell in air

Reflection and transmission coefficient in a 72 mm square waveguide for a unit cell of four hooks of steel wire in air. Total hook length $L = 60$ mm; distance between centre legs, 24 mm; $\sigma_{\text{wire}} = 2 \times 10^5$ S/m.

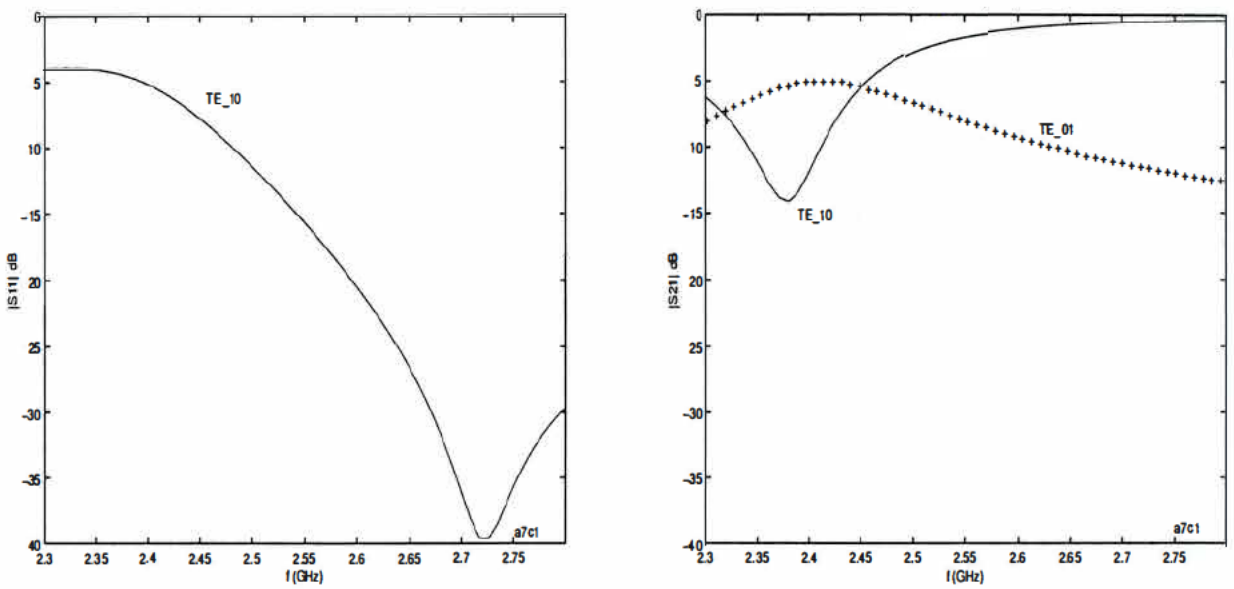

Figure C.5: Point group 422 chiral unit cell of steel hooks in air.

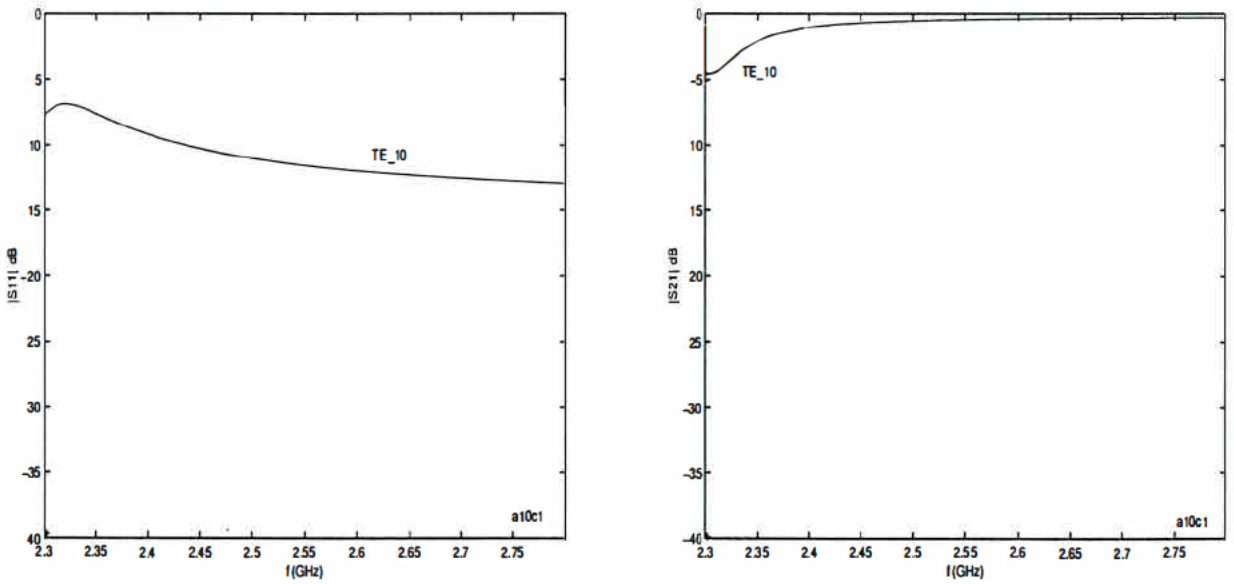

Figure C.6: Point group $4/m$ non-chiral unit cell of steel staples in air.

Steel unit cell in air

Reflection and transmission coefficient in a 72 mm square waveguide for a unit cell of four hooks of steel wire in air. Total hook length $L = 60$ mm; distance between centre legs, 24 mm; $\sigma_{\text{wire}} = 2 \times 10^5$ S/m.

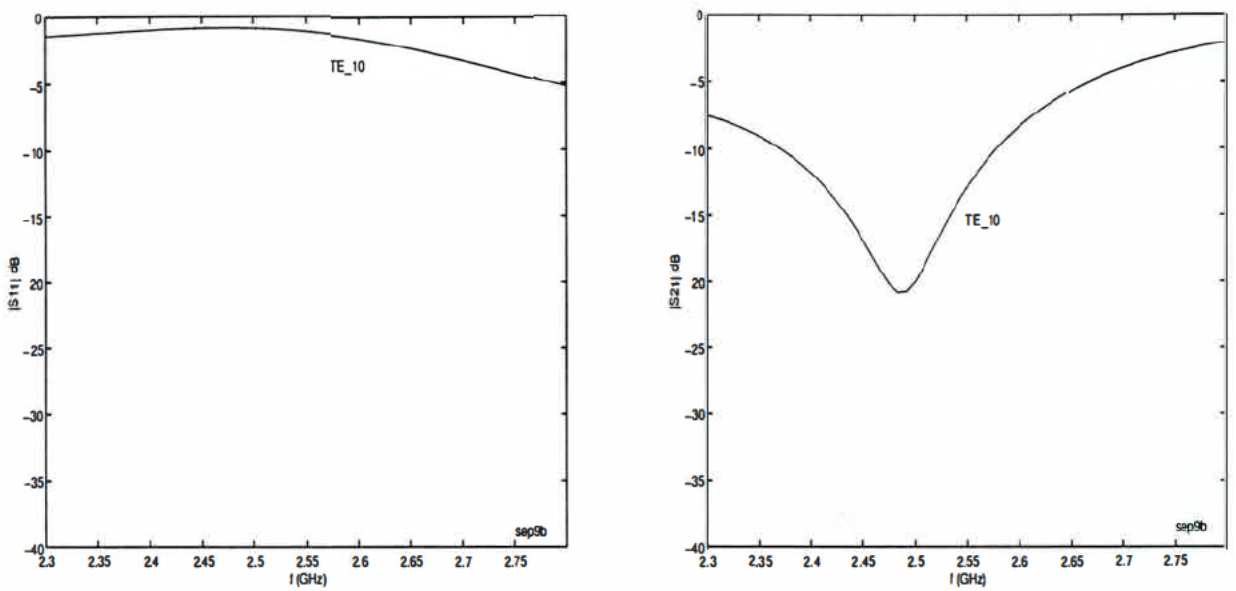

Figure C.7: Point group $\bar{4}$ non-chiral unit cell of steel cranks in air.

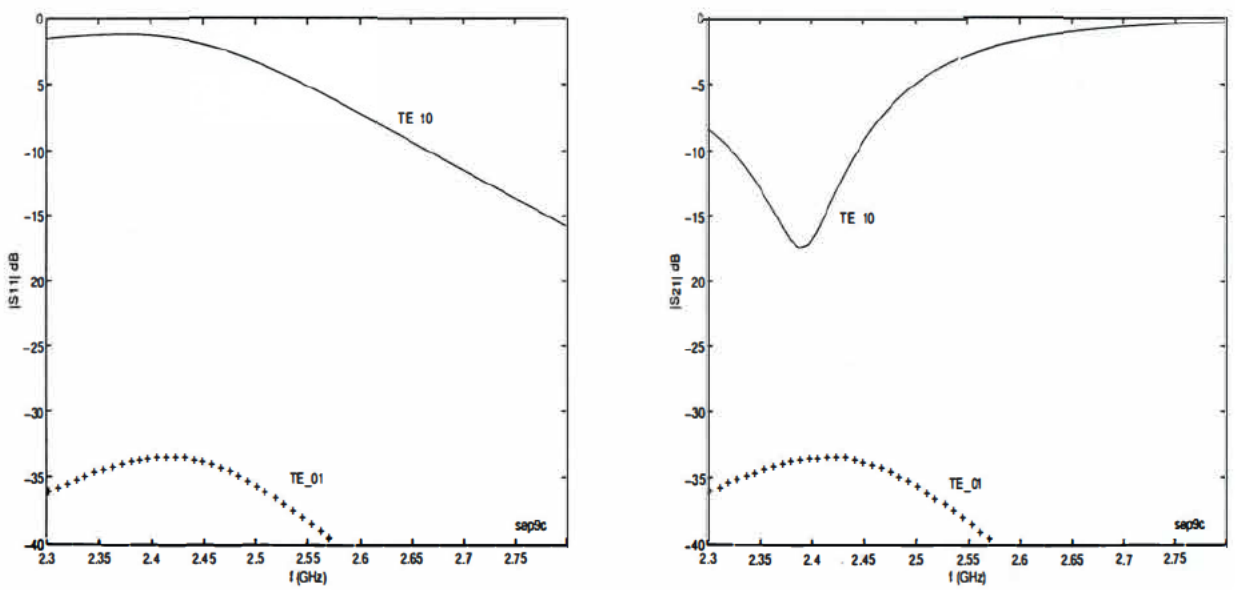

Figure C.8: Point group $\bar{4}$ racemic unit cell of enantiomorphous steel hooks in air.

C.2 Four unit cells in a square waveguide

Copper unit cells embedded in the microwave absorber

Reflection and transmission coefficient in a 72 mm square waveguide for a system of four unit cells of copper hooks embedded in a microwave absorber. Total hook length $L = 48$ mm; distance between centre legs, 24 mm; $\sigma_{\text{wire}} = 5.7 \times 10^7$ S/m; microwave absorbing host, $\epsilon_r = 1.67$ and $\sigma = 0.04$ S/m, thickness 18 mm.

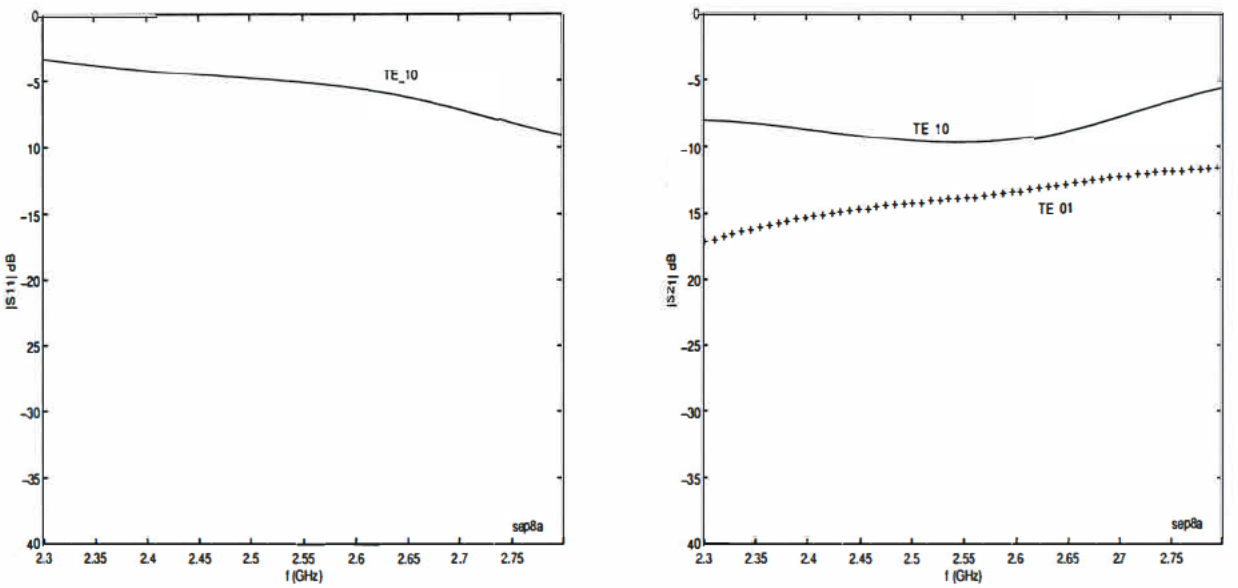

Figure C.9: Four 422 chiral unit cells of the same handedness.

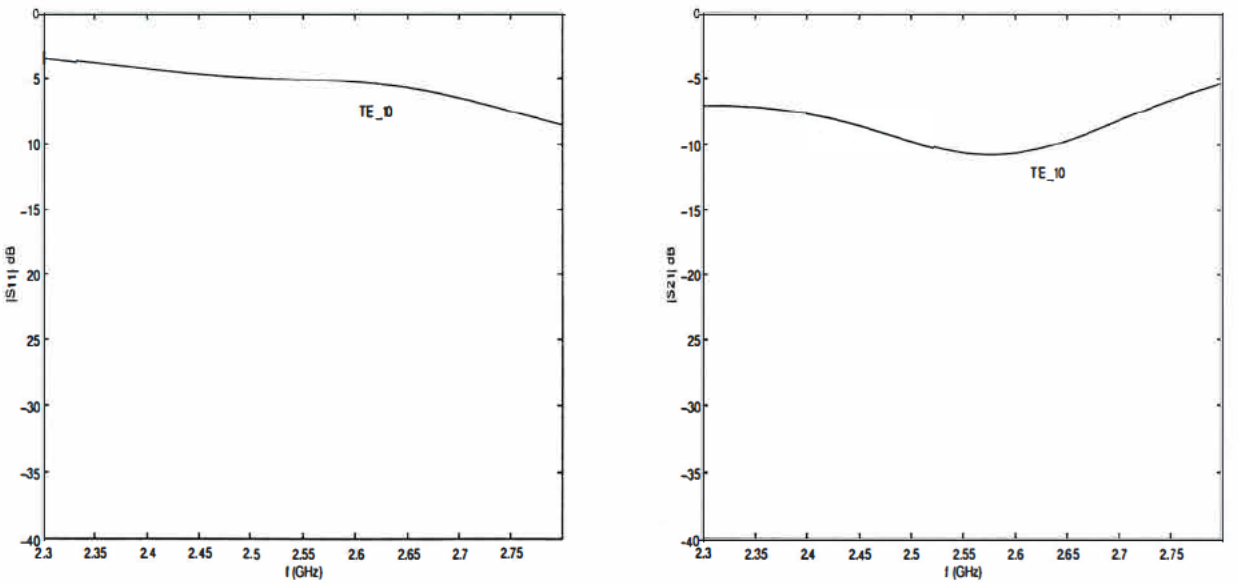

Figure C.10: Four 422 chiral unit cells, related by two orthogonal mirror planes.

Copper unit cells embedded in the microwave absorber

Reflection and transmission coefficient in a 72 mm square waveguide for a system of four unit cells of copper hooks embedded in a microwave absorber. Total hook length $L = 48$ mm; distance between centre legs, 24 mm; $\sigma_{\text{wire}} = 5.7 \text{ x } 10^7$ S/m; microwave absorbing host, $\epsilon_r = 1.67$ and $\sigma = 0.04$ S/m, thickness 18 mm.

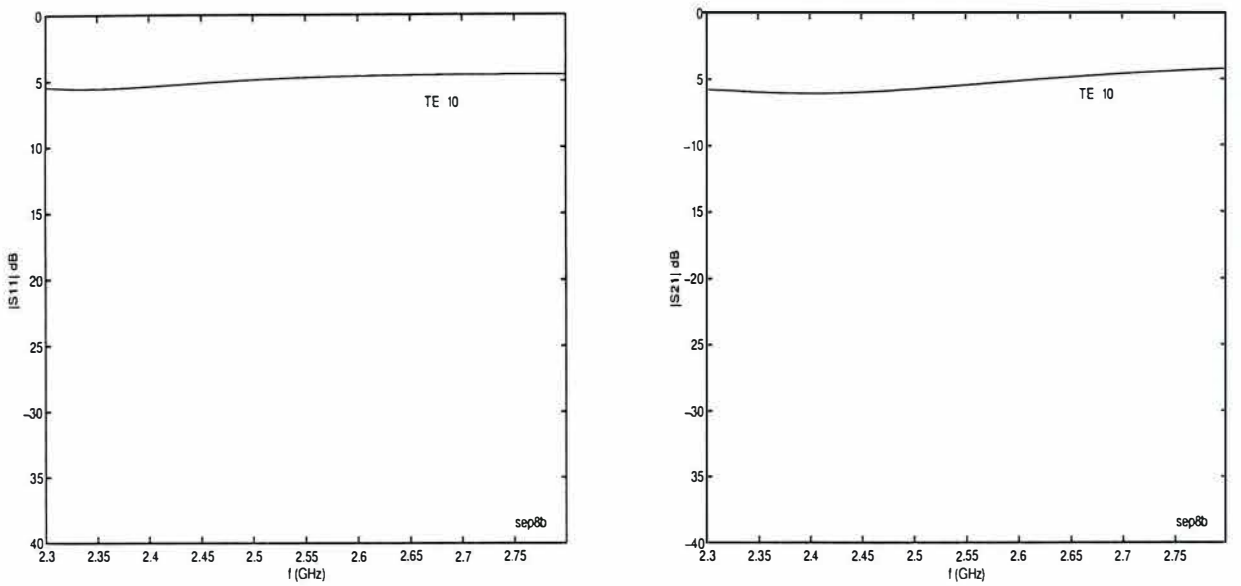

Figure C.11: Four $4/m$ non-chiral unit cells of staples.

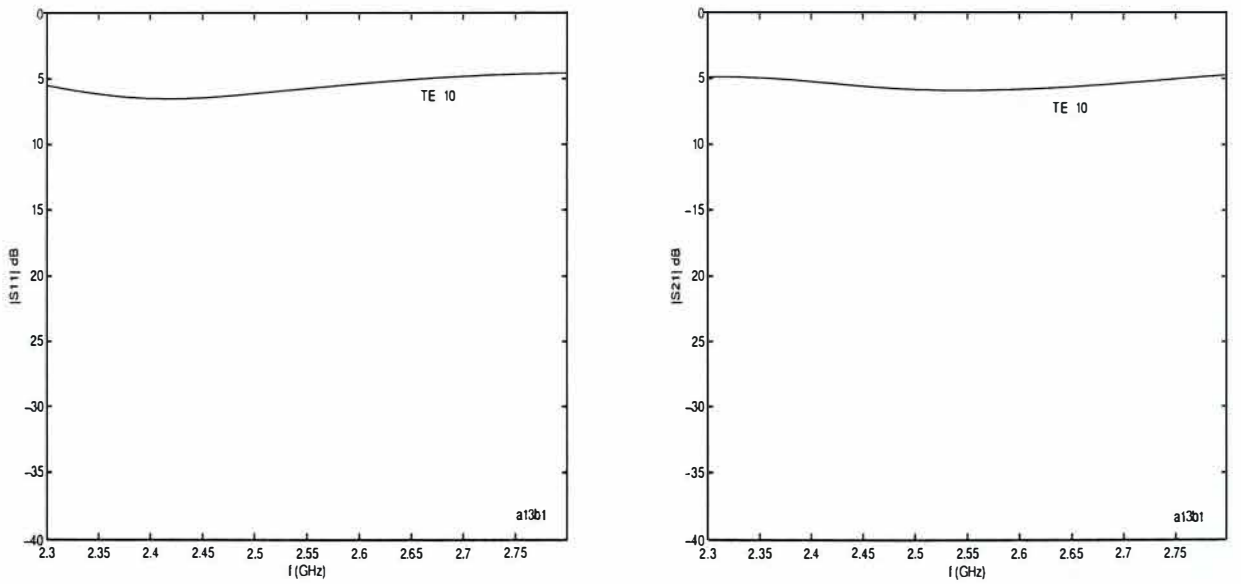

Figure C.12: Four $4/m$ non-chiral unit cells of staples, related by two orthogonal mirror planes.

Steel unit cells in air

Reflection and transmission coefficient in a 72 mm square waveguide for a system of four unit cells of steel hooks in air. Total hook length $L = 60$ mm; the centre legs are separated by 24 mm; $\sigma_{\text{wire}} = 2 \times 10^5$ S/m.

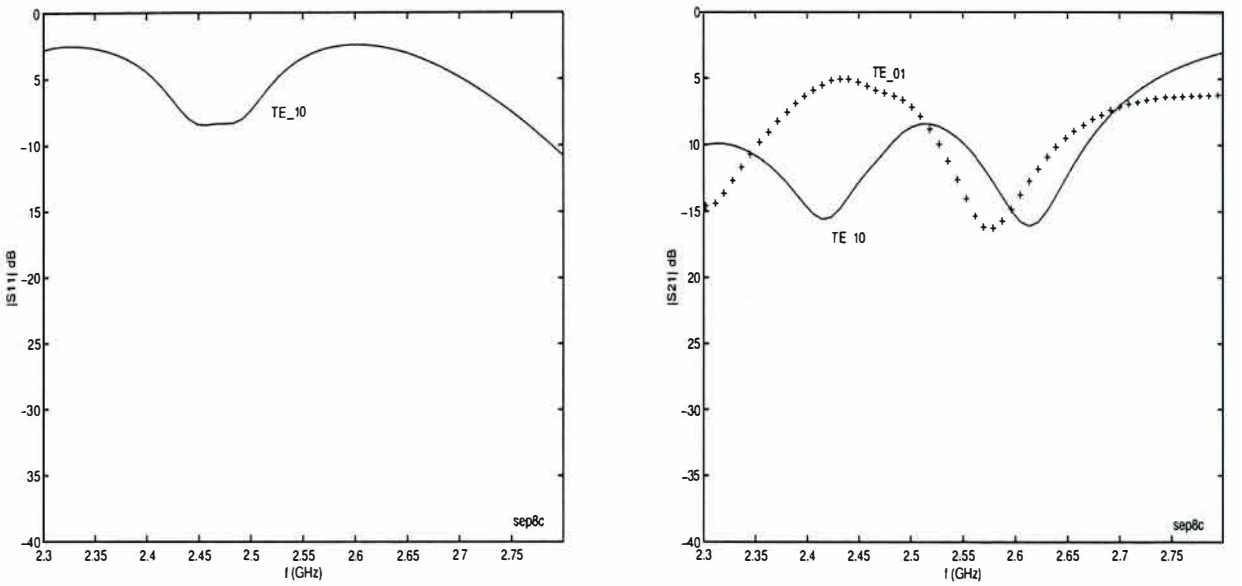

Figure C.13: Four 422 chiral unit cells of the same handedness.

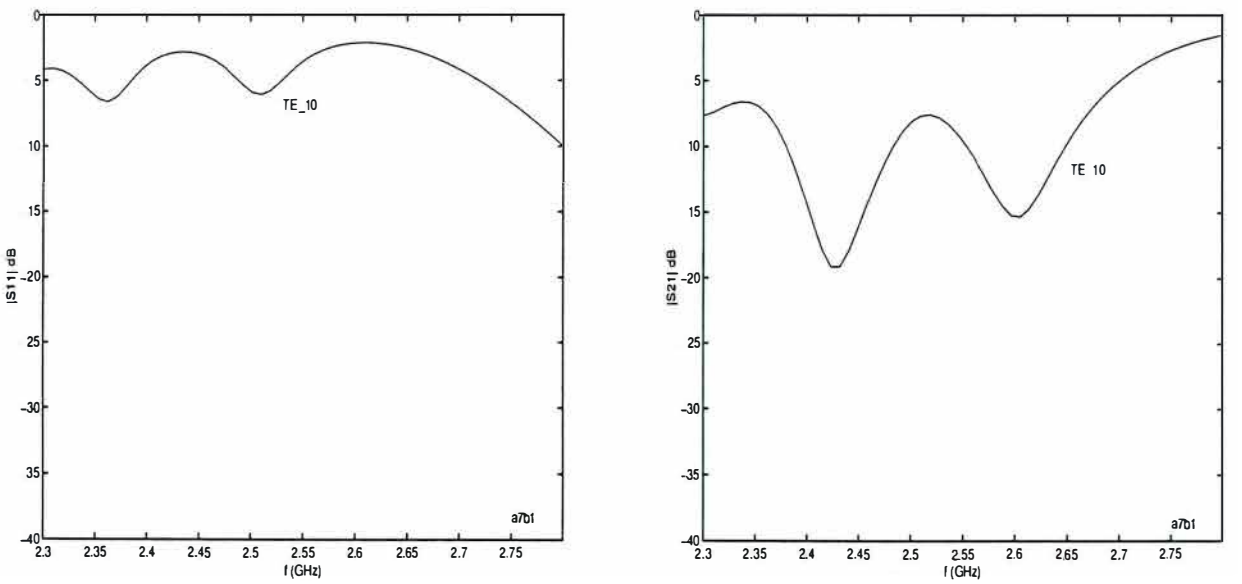

Figure C.14: Four 422 chiral unit cells, related by two orthogonal mirror planes.

Steel unit cells in air

Reflection and transmission coefficient in a 72 mm square waveguide for a system of four unit cells of steel hooks in air. Total hook length $L = 60$ mm; the centre legs are separated by 24 mm; $\sigma_{\text{wire}} = 2 \times 10^5$ S/m.

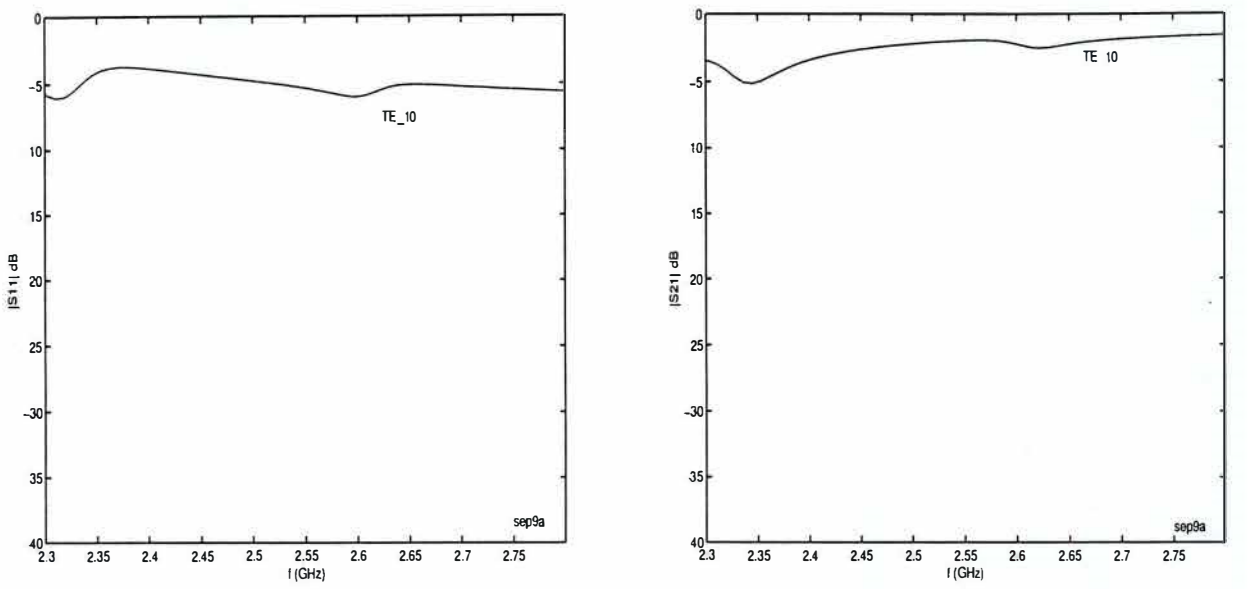

Figure C.15: Four $4/m$ non-chiral unit cells of staples.

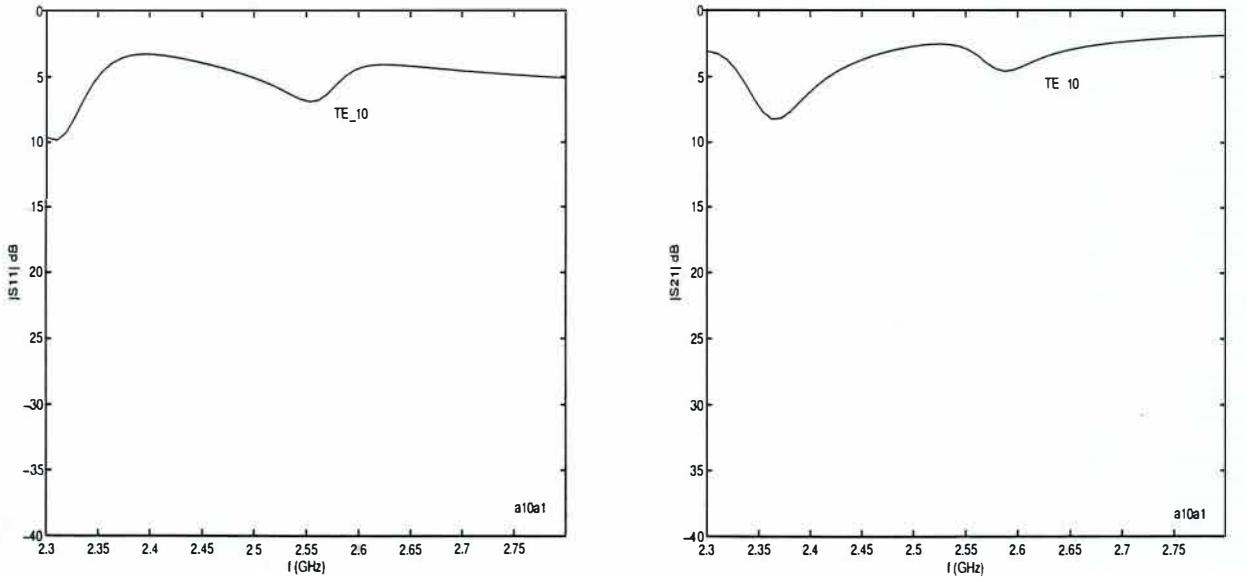

Figure C.16: Four $4/m$ non-chiral unit cells of staples, related by two orthogonal mirror planes.

Bibliography

[1] K. F. Lindman, "Über eine durch ein isotropes System von spiralförmigen Resonatoren erzeugte Rotationspolarization der elektromagnetischen Wellen," *Annalen der Physik*, vol. 63, no. 4, pp. 621 644, 1920. Reprinted in [4], pp. 202 213.

[2] I. Tinoco, Jr. and M. P. Freeman, "The optical activity of oriented copper helices. I. Experimental," *J Physical Chemistry*, vol. 61, pp. 1196 1200, Sept. 1957.

[3] L. D. Barron, *Molecular Light Scattering and Optical Activity.* London: Cambridge University Press, 1982.

[4] A. Lakhtakia, ed., *Selected Papers on Natural Optical Activity.* Bellingham, Washington: SPIE The International Society for Optical Engineering, 1990.

[5] R. E. Raab and J. H. Cloete, "An eigenvalue theory of circular birefringence and dichroism in a non-magnetic chiral medium," *J Electromagnetic Waves and Applications*, vol. 8, no. 8, pp. 1073 1089, 1994.

[6] V. K. Varadan, V. V. Varadan, and A. Lakhtakia, "On the possibility of designing antireflection coatings with chiral composites," *J Wave-Material Interaction*, vol. 2, no. 1, pp. 71 81, 1987.

[7] D. L. Jaggard and N. Engheta, "CHIROSORB™ as an invisible medium," *Electronics Letters*, vol. 25, no. 3, pp. 173 174, 1989.

[8] D. L. Jaggard, N. Engheta, and J. C. Liu, "Chiroshield: a Salisbury/Dallenbach shield alternative," *Electronics Letters*, vol. 26, no. 17, pp. 1332 1334, 1990. Correction: ibid. vol. 27, no. 6, p. 547, 1991.

[9] United States patents 4 948 922, 5 063 391, 5 099 242 and 5 165 059. International patent application PCT/US92/00050. UK patent application GB 2 257 302 A. European patent applications 0 520 677 A1, 0 526 269 A1. (These patents and patent applications on potential uses of synthetic chiral materials were filed between September 1988 and June 1992. Copies were kindly supplied by Dr. Udo Unrau, TU Braunschweig, on 27 April 1994.).

[10] C. F. Bohren, R. Luebbers, H. S. Langdon, and F. P. Hunsberger, "Microwave-absorbing chiral composites: Is chirality essential or accidental?," *Applied Optics*, vol. 31, pp. 6403–6407, 20 Oct. 1992.

[11] J. H. Cloete, S. A. Kuehl, and M. Bingle, "The absorption of electromagnetic waves at microwave frequencies by synthetic chiral and racemic materials," *Int. J Applied Electromagnetics Mechanics*, vol. 9, pp. 103 114, 1998.

[12] I. P. Theron and J. H. Cloete, "The electric quadrupole contribution to the circular birefringence of nonmagnetic anisotropic chiral media: A circular waveguide experiment," *IEEE Trans. Microwave Theory and Techniques*, vol. 44, no. 8, pp. 1451 1459, 1996.

[13] I. P. Theron, *The Circular Birefringence of Artificial Chiral Crystals at Microwave Frequencies.* PhD thesis, Stellenbosch University, Stellenbosch, 1995.

[14] L. J. Spencer *et al.*, "Crystallography," *Encyclopaedia Britannica*, vol. 6, pp. 851–866, 1968.

[15] E. A. Wood, *Crystals and Light: An Introduction to Optical Crystallography.* New York: Dover Publications, 2nd ed., 1977.

[16] R. R. Birss, *Symmetry and Magnetism.* Amsterdam: North-Holland, 2nd ed., 1966.

[17] R. P. Feynman, R. B. Leighton, and M. Sands, *The Feynman Lectures on Physics.* Reading, Massachusetts: Addison-Wesley, 1964.

[18] I. Bernal, W. C. Hamilton, and J. S. Ricci, *Symmetry. A Stereographic Guide for Chemists.* San Francisco: W. H. Freeman, 1972.

[19] C. Kittel, *Introduction to Solid State Physics.* New York: John Wiley and Sons, 7th ed., 1996.

[20] M. J. Gunning and R. E. Raab, "Systematic eigenvalue approach to crystal optics: an analytic alternative to the geometric ellipsoid model," *J Optical Society of America A*, vol. 15, no. 8, pp. 2199 2207, 1998.

[21] K. S. Kunz and R. J. Luebbers, *The Finite Difference Time Domain Method for Electromagnetics.* Boca Raton: CRC Press, 1993.

[22] A. Taflove, *Computational Electrodynamics: The Finite-Difference Time-Domain Method.* Boston, MA: Artech House, 1995.

[23] E. B. Graham, J. Pierrus, and R. E. Raab, "Multipole moments and Maxwell's equations," *J Physics B*, vol. 25, pp. 4673 4684, 1992.

[24] A. R. von Hippel, ed., *Dielectric Materials and Applications.* Boston: Artech House, 1995. Originally published by MIT Press, Cambridge, 1954.

[25] J. D. Jackson, *Classical Electrodynamics.* New York: John Wiley and Sons, 2nd ed., 1975.

[26] M. Bingle, "The finite difference time domain modelling of liquids with dispersive dielectric properties," Master's thesis, Stellenbosch University, Stellenbosch, 1995.

[27] S. Ramo, J. R. Whinnery, and T. van Duzer, *Fields and Waves in Communication Electronics.* New York: John Wiley and Sons, 3rd ed., 1994.

[28] H. A. Haus and J. R. Melcher, *Electromagnetic Fields and Energy.* Englewood Cliffs, New Jersey: Prentice-Hall, 1989.

[29] J.-P. Berenger, "A perfectly matched layer for the absorption of electromagnetics waves," *J. Comput. Phys.*, vol. 114, no. 1, pp. 185 200, 1994.

[30] D. S. Katz, E. T. Thiele, and A. Taflove, "Validation and extension to three dimensions of the Berenger PML absorbing boundary condition for FD-TD meshes," *IEEE Microwave and Guided Wave Letters*, vol. 4, no. 8, pp. 268 270, 1994.

[31] A. G. Smith, *An Experimental Study of Artificial Isotropic Chiral Media at Microwave Frequencies*. PhD thesis, Stellenbosch University, Stellenbosch, 1994.

[32] J. H. Cloete and A. G. Smith, "The constitutive parameters of a lossy chiral slab by inversion of plane wave scattering coefficients," *Microwave and Optical Technology Letters*, vol. 5, no. 7, pp. 303 306, 1992. Correction, ibid. vol. 7, no. 1, p. 42, 1994.

[33] J. Baker-Jarvis, R. G. Geyer, and P. D. Domich, "A nonlinear least-squares solution with causality constraints applied to transmission line permittivity and permeability determination," *IEEE Trans. Instrumentation and Measurement*, vol. 41, no. 5, pp. 646 652, 1992.

[34] M. Bingle, I. P. Theron, and J. H. Cloete, "A frequency domain dispersion and absorption model for numerically extracting the constitutive parameters of an isotropic chiral slab from measured reflection and transmission coefficients," in *Proceedings 13th Annual Review of Progress in Applied Computational Electromagnetics*, pp. 803 810, Monterey, California, March 1997.

[35] R. E. Diaz, "Application of the analytic theory of materials to the modelling of composites in electromagnetic engineering," in *Proceedings 13th Annual Review of Progress in Applied Computational Electromagnetics*, pp. 766 773, Monterey, California, March 1997.

[36] I. J. Craddock and C. J. Railton, "A new technique for the stable incorporation of static field solutions in the FDTD method for the analysis of thin wires and narrow strips," *IEEE Trans. Microwave Theory and Techniques*, vol. 46, no. 8, pp. 1091 1096, 1998.

[37] J. J. Boonzaaier and C. W. I. Pistorius, "Finite-difference time-domain field approximations for thin wires with a lossy coating," *IEE Proc. H, Microw. Antennas Propag.*, vol. 141, no. 2, pp. 107–113, 1994.

[38] J. H. Beggs, R. J. Luebbers, K. S. Yee, and K. S. Kunz, "Finite-difference time-domain implementation of surface impedance boundary conditions," *IEEE Trans. Antennas and Propagation*, vol. 40, no. 1, pp. 49 56, 1992. Corrections, ibid. vol. 41, p. 118, 1993.

[39] E. Kreyszig, *Advanced Engineering Mathematics*. New York: John Wiley and Sons, 6th ed., 1988.

[40] N. Marcuvitz, *Waveguide Handbook*. London: Peregrinus, 1986.

[41] Hewlett-Packard Company, Santa Rosa, CA, *HP8510 Operating and Programming Manual*, April 1988. Manual part no. 08510-90074.

[42] G. R. Jones, M. A. Laughton, and M. G. Say, eds., *Electrical Engineer's Reference Book*. Oxford: Butterworth-Heineman, 15th ed., 1993.

[43] T. Lyman, ed., *Metals Handbook, Volume 1: Properties and Selection of Metals*. Metals Park, Ohio: American Society for Metals, 8th ed., 1961.

[44] A. E. Sanderson, "Effect of surface roughness on propagation of the TEM mode," in *Advances in Microwaves* (L. Young, ed.), vol. 7, pp. 1 57, New York: Academic Press, 1971.

[45] P. W. Hannan and M. A. Balfour, "Simulation of a phased-array antenna in waveguide," *IEEE Trans. Antennas and Propagation*, vol. 13, pp. 342 353, 1965.

[46] A. I. Zverev, *Handbook of Filter Synthesis*. New York: John Wiley and Sons, 1967.